Organizational Results Research Report

July 2005

RI 99.026

OR 06.001

Shear Test of High Performance Steel Hybrid Girders

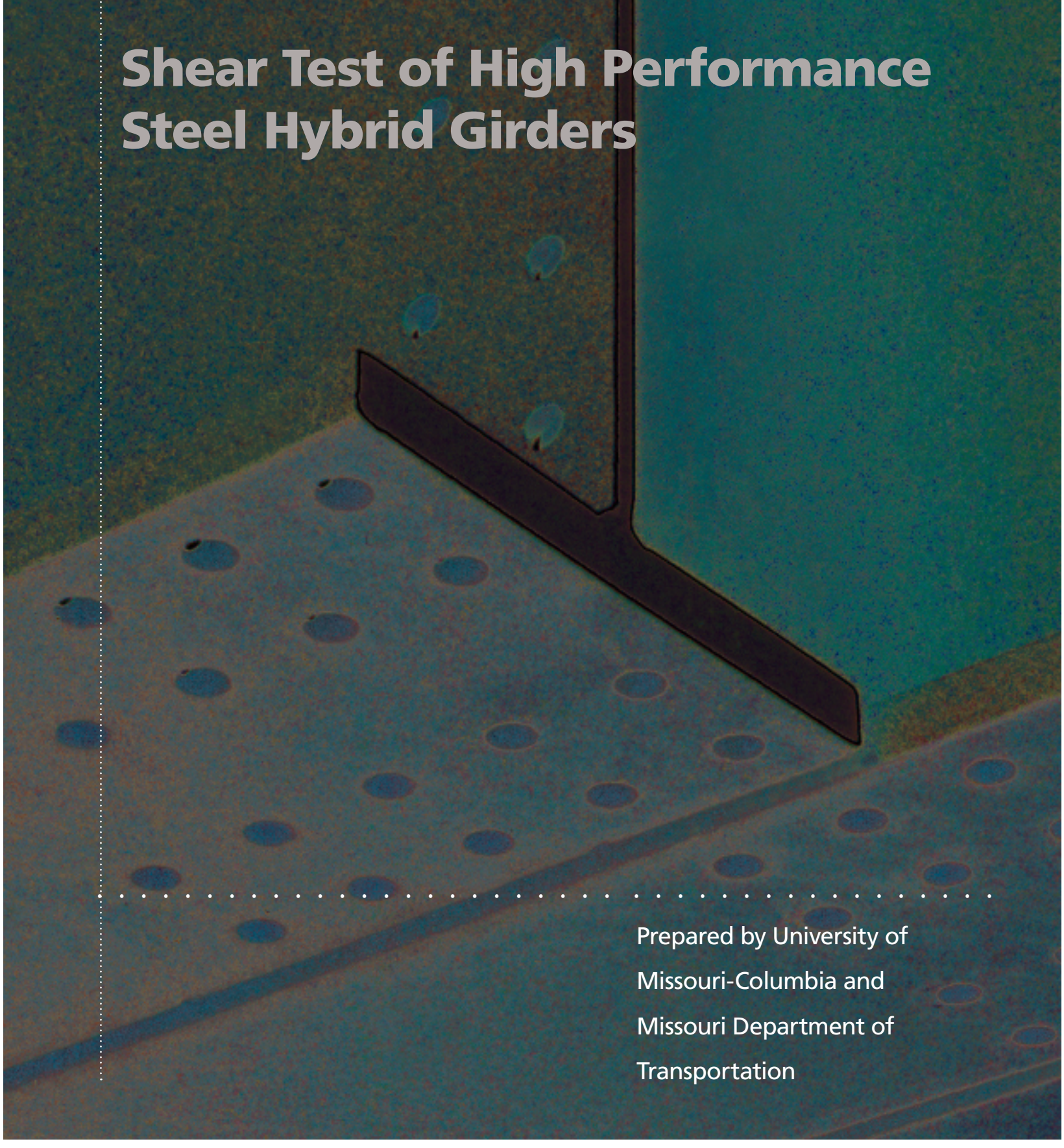

Prepared by University of Missouri-Columbia and Missouri Department of Transportation

Draft Final Report

RI99-026

SHEAR TESTS OF HIGH PERFORMANCE STEEL HYBRID GIRDERS

Prepared for the
Missouri Department of Transportation
Research Development & Technology

By:
Michael G. Barker, PE
University of Wyoming
formerly of the
University of Missouri-Columbia

Submitted
June 2005

The opinions, findings and conclusions expressed in this report are those of the principal investigator and the Missouri Department of Transportation. They are not necessarily those of the U.S. Department of Transportation or the Federal Highway Administration. This report does not constitute a standard, specification or regulation.

ACKNOWLEDGEMENTS

The author wishes to recognize the graduate students that worked on this project: auSTIN Hurst, John Schreiner, Courtney Rush, Ben Davis, Adam Zentz, and Tori Goessling. Special thanks are due to C.H. Cassil who dedicated himself to this project and made sure the testing was done with professionalism and care.

This work was part of a collaborative effort involving the American Iron and Steel Institute, the Federal Highway Administration, the Missouri Department of Transportation, and Georgia Tech University.

EXECUTIVE SUMMARY

High Performance Steel, in particular HPS70W, has been used in hundreds of bridges across the United States. A large percentage of these bridges have used the HPS in the form of hybrid girder designs. Bridge studies have shown that the most beneficial use of HPS70W (70 ksi) is in the flanges of hybrid girders with 50 ksi webs. One limit with hybrid girder design, which decreases the beneficial aspects, is that tension field action (TFA) is not allowed when determining the shear capacity. This is a severe shear capacity penalty for using hybrid girders. Limiting hybrid shear capacities to the shear buckling capacity results in more transverse stiffeners required (closer spacing) for a hybrid girder than that for a homogeneous girder. This not only increases material costs, but significantly increases fabrication costs.

The objective of this research is to validate the tension field action behavior in hybrid plate girders. The goal is to allow TFA in hybrid girders resulting in more economical design of steel bridges.

The work conducted for this research covers several topics in tension field action and moment-shear interaction of plate girders. The first effort concentrated on the original shear capacity theoretical derivations and the differences in using hybrid girders. In addition, two series of tests were designed and tested to determine the hybrid girder shear capacity and study the tension field behavior of homogeneous and hybrid girders. Series I test specimens were homogeneous and hybrid girders tested under high shear and low moment conditions. Series II test specimens were designed and tested to study the effect of moment-shear interaction. Finally, an array of practical bridge designs was developed to study the benefit of allowing TFA in hybrid girders.

This report includes a thorough presentation of tension field action and moment-shear interaction in plate girders, and in particular hybrid plate girders. It presents a comprehensive presentation on the test girders with a detailed analysis and examination of the test behaviors.

There are a few important results that may improve the design of hybrid steel girder bridges. Hybrid steel girders exhibit tension field action according to current AASHTO shear capacity provisions. Using the original moment-shear interaction derivations, this research has produced a theoretical lower-bound moment-shear interaction equation for hybrid girders that is equivalent to the current AASHTO moment-shear interaction requirement for homogeneous girders. However, the results of the experimental tests and analytical studies have also shown that there is no moment-shear interaction for these plate girders. The girders all demonstrated that the capacities exceeded expectations and that a moment-shear interaction reduction is not necessary.

TABLE OF CONTENTS

LIST OF FIGURES

LIST OF TABLES

Chapter 1 - Introduction

1.1 Problem Statement

With the advent of HPS70W steel (High Performance Steel with yield strength of 70 ksi), hundreds of bridges have been built using HPS. The AASHTO LRFD Specifications (1998) have been updated to allow HPS70W steel in bridges. Studies have shown that the current design specifications are adequate for HPS70W and the issues of ductility and buckling are sufficiently considered (Barth et al. 2000). Therefore, bridges have been built, and many more will be built, with HPS70W material. A majority of these bridges will use hybrid girders.

Hybrid steel girders were a popular choice for bridge girders in years past. Using 50 ksi material for the flanges with a lower cost 36 ksi web material yielded more economical results while still maintaining flexural capacities near a homogeneous 50 ksi girder. Since that time, the cost gap between the two strength materials dwindled and the economic benefit of hybrid girders vanished. However, with High Performance Steel, hybrid design has become a common practice again. Bridge studies (Barker and Schrage 2000) have shown that the most beneficial use of HPS70W (70 ksi) is in the flanges of hybrid girders with 50 ksi webs.

One limit with hybrid girder design, which decreases the beneficial aspects, is that tension field action (TFA) is not allowed when determining the shear capacity. The reasoning is that, in hybrid girders, the web yields near maximum moment, which may affect the tension strut assumed for TFA. This is a severe shear capacity penalty when using hybrid girders. Limiting hybrid shear capacities to the shear buckling capacity

results in more transverse stiffeners required (closer spacing) for a hybrid girder than that for a homogeneous girder. This not only increases material costs, but significantly increases fabrication costs.

Tension field action is a type of shear behavior observable in transversely stiffened girders. The slender web of a plate girder may buckle under applied load, after which it can no longer resist shear in the traditional beam manner. Additional applied shear beyond the shear buckling capacity of the web can be resisted through tension field action, which includes formation of a tension strut diagonally across the buckled web panel. This tension strut anchors to the transverse stiffeners and flanges that border the shear panel, and the magnitude of vertical shear resistance is taken to be the vertical component of the tension strut. The tension field action contribution to shear capacity depends on the stiffener spacing, but can typically be equal in magnitude to the shear buckling capacity. The total shear capacity of a stiffened girder is the sum of the shear buckling capacity and the tension field action capacity. Thus, the use of tension field action can significantly increase the shear design capacity of the girder.

A major concern with hybrid girders is that the lower strength web material may yield before the nominal moment capacity of the girder is attained. The web yielding problem leads to concerns about the ability of tension field action stresses to achieve sufficient anchorage through the yielded web material. There has been little research performed on this topic, so tension field action shear capacity is not allowed in the design of hybrid plate girders according to AASHTO's (1998) Load and Resistance Factor Design (LRFD) design code, and the design shear capacity of hybrid girders is limited to the shear buckling capacity. Limiting the shear capacity of hybrid girders often results in

the use of thicker web panels and additional transverse stiffeners to increase the design shear capacity of the hybrid girder. The ultimate result is a less economical hybrid design.

1.2 Research Objective

The objective of this research is to validate the tension field action behavior in hybrid plate girders. The goal is to allow TFA in hybrid girders resulting in more economical design of steel bridges. Using thicker webs or extra transverse stiffeners would no longer be necessary to obtain the required shear capacity, which would save material and labor costs, as well as reduce weight and decrease the number a fatigue details on the girder. The use of hybrid design can result in shallower girder depths, which will require less material and labor costs for bridge approaches. The ultimate result of allowing tension field action shear capacity to be used for hybrid design is the ability to achieve less expensive, more efficient projects without sacrificing quality or safety.

Tension field action certainly does occur in transversely stiffened hybrid plate girders, especially in situations where the flexural stresses are relatively low. If flexural stresses are low, then there is no web yielding in the hybrid girder, and the tension field should be no different than conventional homogeneous girders. However, as flexural stresses increase and web yielding is possible, there may be some reduction in tension field action capacity. The interaction between bending moment and shear capacity is also investigated in this research.

1.3 Research Content

The work conducted for this research covers several endeavors. These topics will be presented in this report as described in Section 1.4. The first effort concentrated on the original shear capacity theoretical derivations (Basler 1961a) and the impact of using hybrid girders. Proposed lower bound shear capacity procedures were developed that represent the equivalent AASHTO equations for hybrid girders (Barker et al 2002, Hurst 2000). Hurst (2000) reformulates the original derivations to account for hybrid design and develops new proposed moment-shear interaction equations.

Two series of tests were designed (Hurst 2000) and tested to determine the hybrid girder shear capacity and study the tension field behavior of homogeneous and hybrid girders. Series I test specimens were homogeneous and hybrid girders tested under high shear and low moment conditions. Results from Series I testing are published in two separate theses (Schreiner 2001, Rush 2001). Schreiner's thesis documents the testing procedure and verifies that the hybrid girder's shear capacities were accurately predicted by AASHTO's current tension field action design equations. Rush's thesis interprets the experimental data and compares it to tension field action theory, concluding that tension field action stresses are present in hybrid girders and reasonably predicted by theory.

Series II test specimens were designed and tested to study the effect of moment-shear interaction. Results from Series II testing are published in two separate theses (Zentz 2002, Davis 2002). Davis' thesis documents the testing procedure and compares the hybrid girder's shear capacities to AASHTO's current and Hurst's proposed tension field action moment-shear interaction equations. Zentz's thesis interprets the experimental

data and compares it to tension field action theory, concluding that hybrid girders are capable of developing tension field action stresses predicted by theory.

Finally, Goessling (2002) studied an array of practical bridge designs to study the impact of allowing TFA in hybrid girders. The study included two- and three-span bridges with varying span lengths, number of girders (girder spacing) and web slenderness ratios. The results are presented in terms of number of transverse stiffeners required with and without tension field action.

1.4 Results

This research, in conjunction with research at Georgia Tech (Aydemir 2000) found that tension field action shear capacity is fully applicable to hybrid girders. The AASHTO shear capacity equations are accurate for hybrid girders and that there is not a moment-shear interaction for any plate girder, whether homogeneous or hybrid. Allowing tension field action in hybrid plate girders and removing the moment-shear interaction for all plate girder designs would be a major advancement for steel bridge design.

1.5 Report Organization

This report will begin with background information concerning hybrid plate girders, tension field action theory, and moment-shear interaction in Chapter 2. A summary of the original derivation of the currently accepted tension field action theory will be followed by presentation of AASHTO's (1998) Load and Resistance Factor Design shear design capacity equations. Chapter 2 also presents Hurst's (2000) derivation of a lower bound moment-shear interaction equation, in AASHTO format, that

considers hybrid action in plate girders. Although the final results show there should not be any moment-shear interaction, the proposed hybrid moment-shear interaction is presented to demonstrate the moment-shear interaction theory and to give a conservative lower bound for moment-shear interaction in hybrid designs.

Chapter 3 presents the Series I & II test specimens, the test set-up, testing procedures and theoretical experimental results for the test girders. Emphasis is placed on the Series II tests since they constitute the most important part of this work. The Series I tests, high shear and low moment, were expected to show applicable tension field action and the results are a basis for the Series II tests. The Series II tests, the moment-shear interaction tests, provide the important conclusions and results for this study.

Chapter 4 presents the experimental test analyses. Again, the Series II tests are emphasized due to their importance. The experimental shear capacities from the Series I tests have been shown to be comparable to those calculated by the current AASHTO tension field action design equations (Schreiner 2001). To validate the tension field action behavior, the experimental capacities and stress responses were compared to tension field action theory (Rush 2001). The Series II tests are examined in detail in Chapter 4. The experimental shear capacities were found to be adequately predicted by current AASHTO tension field action design equations (Davis 2002). The experimental stress behavior and tension action behavior is also shown to correspond with theory (Zentz 2002). Chapter 4 includes an impact section that describes the savings that can be realized using tension field action in hybrid plate girders and removing the moment-shear interaction for all plate girders (Goessling 2002).

Chapter 5 presents the results and conclusions of the research efforts.

Chapter 2 - Tension Field Action

2.1 Introduction

The purpose of this chapter is to provide background information on the shear strength of hybrid plate girders subject to concurrent shear and bending. Plate girders and hybrid steel design are introduced, followed by current shear design equations. A brief derivation of the shear design equations is given, and limitations of the current shear design equations concerning hybrid plate girders are discussed. Moment-shear interaction is explained and the current interaction equations presented, along with a summary of the original derivation. The original derivation is modified to accommodate hybrid girders. Finally, a proposed lower-bound moment-shear interaction diagram for hybrid girders will be presented.

2.2 Hybrid Plate Girders

Plate girders are I-shaped steel girders built-up from flanges and webs cut from steel plates and welded together. They are commonly used when the available hot-rolled W-shapes are inadequate for a given span and loading. Currently, plate girders are commonly used for bridges, but can also be used for special-purpose buildings where long spans or high loadings are present. When properly designed and implemented, plate girders are very efficient and cost-effective flexural members.

For any I-shaped section, the flanges provide the majority of the moment capacity while the web provides shear resistance. Moment capacity of plate girders can be increased by increasing the girder depth, increasing the amount of steel used in each

girder, or by improving the properties of the steel. However, using additional steel increases the self-weight of the girder as well as the total steel costs. Indirect costs, such as costs due to larger bridge approaches, can also arise by increasing the depth of the girder.

Improving steel properties is a way to increase moment capacity without additional girder weight or depth. High Performance Steel (HPS) has higher yield strengths than conventional steels, thus conventional flexural members can be replaced by smaller HPS members. However, there is currently a cost premium associated with HPS, so homogeneous HPS sections are often uneconomical. Barker and Schrage (2000) have shown that using a combination of conventional steel web and HPS flanges (hybrid design) can be more economical than homogeneous sections of either 50 or 70 ksi steel. The higher yield strength HPS flanges increase moment capacity while using the less expensive conventional steel web saves material costs.

Plate girders are designed with slender webs in order to minimize material costs while maintaining the distance between flanges. Web instability is a concern whenever slender webs are used, so transverse stiffeners are welded to the web to increase capacity. The transverse stiffeners, if properly spaced, create larger web buckling capacity and allow for the development of tension field action shear capacity.

2.3 Shear Capacity

The shear capacity of a transversely stiffened plate girder is composed of two parts: the shear buckling capacity and the post-buckling shear capacity. Theoretically, a transversely stiffened plate girder initially resists shear in a beam type manner up to a

shear load level called the shear buckling capacity. Once the applied shear reaches the shear buckling capacity, it is assumed that the web buckles and additional applied shear is resisted through a post-buckling phenomenon known as tension field action (TFA) until the nominal shear capacity of the plate girder is reached. The following discussions explain the theory behind each mode of shear resistance, the capacities associated with each mode, and give the current AASHTO design equations for shear capacity of transversely stiffened plate girders.

2.3.1 Shear Buckling Capacity

As a transversely stiffened plate girder is loaded with vertical shear loading, an element at the neutral axis theoretically experiences a state of pure beam shear stress, as shown in Figure 2-1(a) below. The principal stresses for this element lie on a plane that is inclined 45° from the horizontal. These principal stresses are a normal tensile stress on one diagonal and a normal compressive stress on the other diagonal. As the load is increased, these principal stresses increase. When the shear load reaches the shear buckling capacity, the slender web buckles between transverse stiffeners due to the diagonal compressive stress. This is the upper limit of the shear buckling capacity of transversely stiffened plate girders.

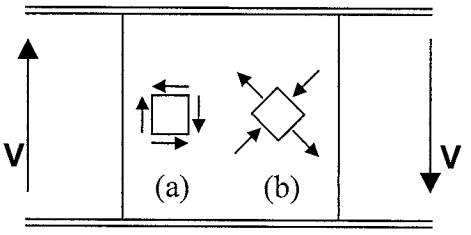

Figure 2-1. Neutral Axis Stresses

The shear buckling capacity used in AASHTO's LRFD (1998) design code is given as:

$$V_{cr} = C \cdot V_p$$ **Equation 2-1**

Where:

V_{cr} = shear buckling capacity

C = ratio of shear buckling stress to shear yield strength

For elastic buckling:

$$C = \frac{1.52}{\left(D/t_w\right)^2}\left(\frac{E \cdot k}{F_{yw}}\right)$$ **Equation 2-2**

Where:

E = modulus of elasticity of the material

F_{yw} = yield stress of web material

D = web depth

t_w = web thickness

$$k = 5 + \frac{5}{\left(d_0/D\right)^2}$$ **Equation 2-3**

Where:

d_0 = transverse stiffener spacing

V_p = plastic shear capacity = $0.6A_wF_{yw}$ **Equation 2-4**

Where:

A_w = cross sectional area of web

2.3.2 Post-Buckling Shear Capacity

When the shear load on a transversely stiffened plate girder exceeds the shear buckling capacity, the web buckles under diagonal compressive forces. The buckled web, theoretically, cannot support any additional diagonal compressive forces, so a new load resisting mechanism resists additional shear loading. This phenomenon is called tension field action. Diagonal tensile forces form a tension band across the web, which anchors to the flanges and transverse stiffeners in opposite corners of the web panel, as shown in Figure 2-2. The vertical component of this tension band is responsible for the post-buckling vertical shear capacity of transversely stiffened plate girders. The tension field action mechanism can be easily visualized by comparing it with that of a Pratt truss (see Figure 2-3).

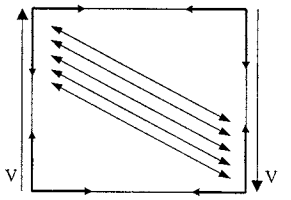

Figure 2-2. Diagonal Tensile Stresses Anchor to Corners of Shear Panel

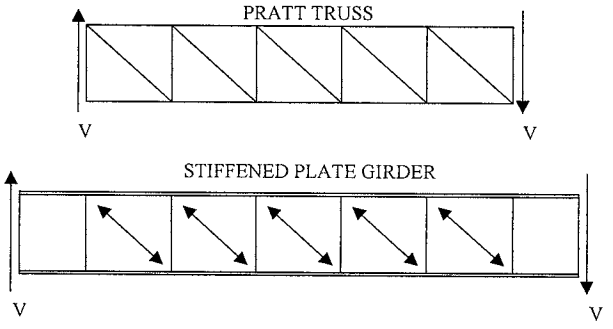

Figure 2-3. Pratt Truss / Tension Field Action Comparison

The post-buckling shear capacity, V_{tfa}, used in AASHTO's 1998 design code is given as:

$$V_{tfa} = V_p \cdot \frac{0.87 \cdot (1 - C)}{\sqrt{1 + \left(d_0 / D\right)^2}}$$ **Equation 2-5**

The full shear capacity of a transversely stiffened plate girder is given by the sum of the elastic shear capacity and the post-buckling shear capacity:

$$V_n = V_{cr} + V_{tfa}$$ **Equation 2-6**

Where:

V_n = nominal shear capacity of transversely stiffened plate girder

2.3.3 Basler's Shear Capacity Derivation

The current AASHTO design code equations relating to the shear capacity of transversely stiffened plate girders are based on research by Basler (1961a). A brief summary of Basler's derivation follows.

Basler initially assumes the ultimate shear force of a transversely stiffened plate girder can be described as the product of the plastic shear force and a nondimensional function depending on the following parameters: stiffener spacing, web depth, web thickness, yield stress, and modulus of elasticity. In mathematical form:

$$V_u = V_p \cdot f\left(d_0, D, t_w, F_y, E\right)$$ **Equation 2-7**

Where:

V_u = ultimate shear force

V_p = plastic shear capacity

f = nondimensional function

d_0 = transverse stiffener spacing

D = web depth

t_w = web thickness

F_y = yield stress of the material

E = modulus of elasticity of the material

The plastic shear force is described as "the shear force for which unrestricted yielding occurs" and is similar in concept to the plastic moment used in plastic analysis (Basler 1961a). The plastic shear force is calculated as the product of the shear yield stress and the cross-sectional area of the web.

The Hencky – von Mises yield criterion is used to determine the shear yield stress, τ_y. For the case of yielding under pure shear, $\sigma_1 = -\sigma_2 = \tau_y$, where σ_1 and σ_2 are the major and minor principal stresses, respectively. In this case, the yield criterion gives $\tau_y = F_y/\sqrt{3}$ as shown in Figure 2-4.

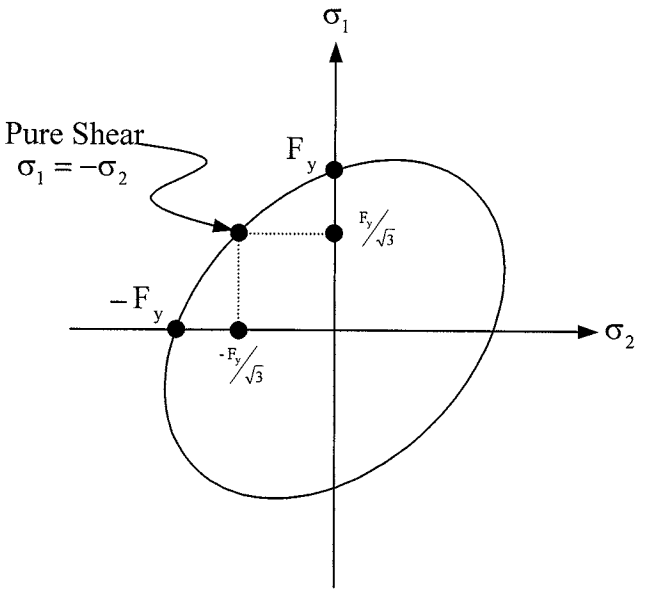

Figure 2-4. Von Mises Yield Criterion

The plastic shear force becomes:

$$V_p = \tau_y D\, t_w = \frac{1}{\sqrt{3}} F_y D\, t_w = 0.58 F_y D\, t_w$$ **Equation 2-8**

Basler assumes that during tension field action behavior, a uniform tension field of magnitude σ_t acts on the web's cross-section, inclined at some angle ϕ from the horizontal as is shown in Figure 2-5.

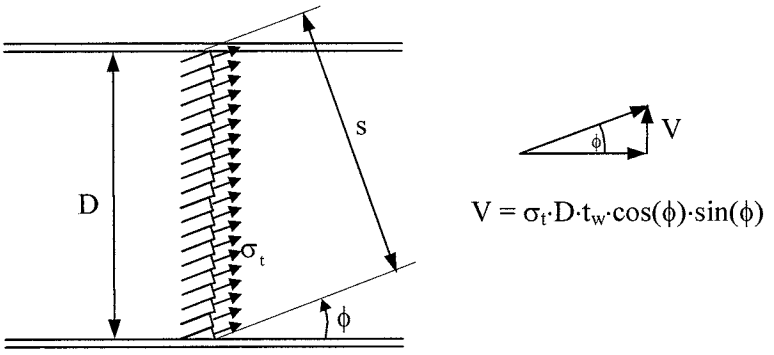

Figure 2-5. Basler's Assumed Tension Field

The vertical component of this tension field is found to be:

$$V = \sigma_t D\, t_w \cos(\phi)\sin(\phi)$$ **Equation 2-9**

Where:

V = vertical shear force due to inclined tension field

σ_t = magnitude of tension field stresses

ϕ = inclination of tension field from horizontal

The maximum shear force occurs when $\phi = 45°$, which yields:

$$V_{max} = \frac{1}{2} \cdot \sigma_t \cdot D \cdot t_w$$ **Equation 2-10**

In order for any tension field to be effective in resisting vertical shear, proper anchorage must be provided. For the assumed uniform tension field across the entire surface

of the web, anchorage would have to be provided by the flanges in both the horizontal and vertical directions. However, the flanges lack the flexural rigidity to provide anchorage in the vertical direction, so a partial tension field must be assumed. Like the previous uniform tension field, the partial tension field has stresses of magnitude σ_t oriented at an angle ϕ from the horizontal. The partial tension field is assumed to have a bandwidth, s, such that only the transverse stiffeners provide vertical anchorage.

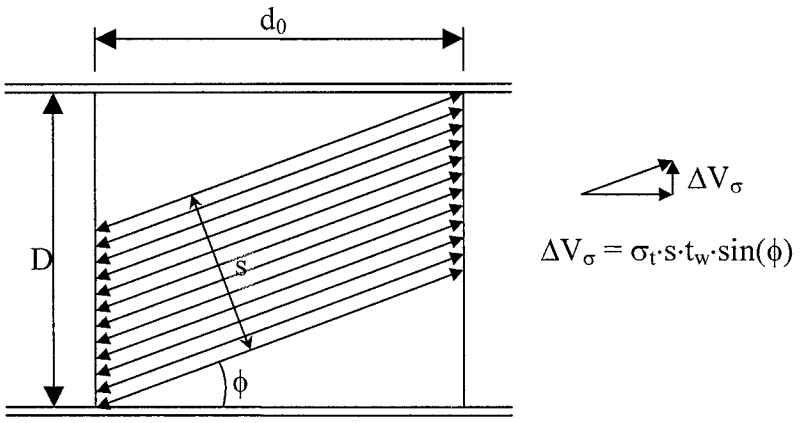

Figure 2-6. Basler's Assumed Partial Tension Field

The tension field bandwidth, measured perpendicular to the inclination of the stresses, can be expressed as:

$$s(\phi) = D \cdot \cos(\phi) - d_0 \cdot \sin(\phi)$$ **Equation 2-11**

Where:

s = bandwidth of partial tension field, a function of ϕ

The vertical shear force resulting from the partial tension field is expressed as:

$$\Delta V_\sigma = \sigma_t \cdot s \cdot t_w \sin(\phi)$$ **Equation 2-12**

Where:

ΔV_σ = vertical resultant shear force from partial tension field

Or, by substituting Equation 2-11 into Equation 2-12:

$$\Delta V_\sigma = \sigma_t t_w \left[\frac{D}{2} \sin(2\phi) - \frac{d_0}{2} (1 - \cos(2\phi)) \right] \qquad \textbf{Equation 2-13}$$

As the applied shear stresses continue to increase, the bandwidth associated with the partial tension field must increase. This means that the inclination of the tension field must decrease. At some point there is an optimum contribution of ΔV_σ to the shear force V_σ. Basler assumes that failure of the plate girder occurs when the ΔV_σ reaches a maximum value. In order to find the inclination of the tension field at the ultimate shear load, Equation 2-13 is differentiated with respect to ϕ and set equal to zero, as follows:

$$\frac{d}{d\phi}(\Delta V_\sigma) = 0 \qquad \textbf{Equation 2-14}$$

Which yields:

$$\sigma_t t_w (D \cdot \cos(2\phi) - d_0 \cdot \sin(2\phi)) = 0 \qquad \textbf{Equation 2-15}$$

Neither the tension field stress nor the web thickness is zero, so

$$D \cdot \cos(2\phi) - d_0 \cdot \sin(2\phi) = 0 \qquad \textbf{Equation 2-16}$$

Simplifying Equation 2-16 yields:

$$\tan(2\phi) = \frac{D}{d_0}$$

Equation 2-17

Equation 2-17 shows that the angle 2ϕ is equivalent to the angle between the panel diagonal and the horizontal, as shown in Figure 2-7. Using that relationship, the following quantities are readily obtained:

$$\sin(2\phi) = \frac{1}{\sqrt{1+\left(d_0/D\right)^2}}$$

Equation 2-18

$$\cos(2\phi) = \frac{d_0/D}{\sqrt{1+\left(d_0/D\right)^2}}$$

Equation 2-19

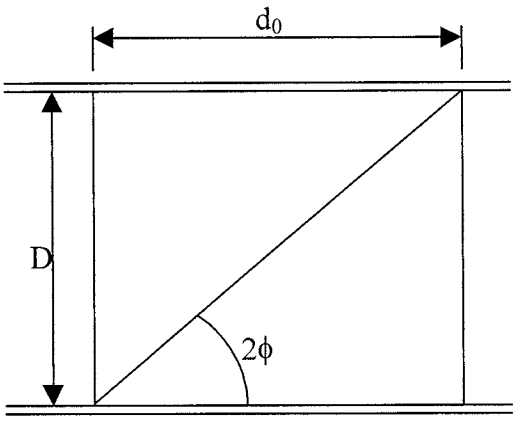

Figure 2-7. Shear Panel Diagonal

Next, Basler assumes a succession of web panels subject to a constant shear force, as shown in Figure 2-8. A free body diagram (Figure 2-9) is taken by making cuts at A, B, and C. Along cut A, the web is subjected to an unknown resultant, which is decomposed into a normal force, F_w, and a shear force component. The shear component is $V_\sigma/2$ due to symmetry. Flange force F_f also acts at section A. Similar force components act at cut B, except the flange force changes by an amount ΔF_f. At section C, the tension field stresses, σ_t, act at an inclination of ϕ, which is defined in Equation 2-17. Vertical stiffener force F_s also acts at cut C. Solving the system statically will yield an expression for V_σ, the ultimate shear force due to the partial tension field.

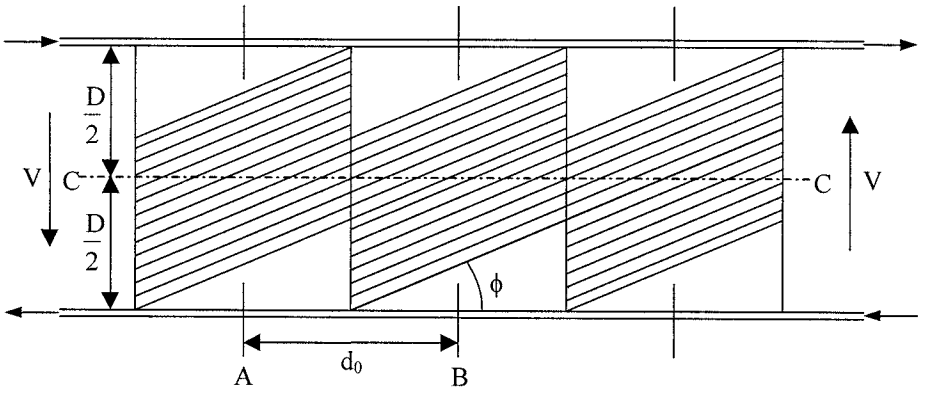

Figure 2-8. Succession of Web Panels

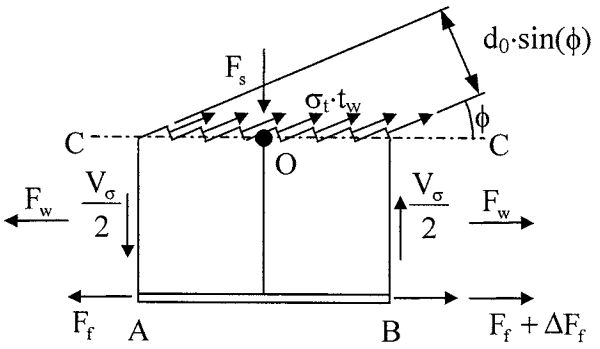

Figure 2-9. Assumed Free Body Diagram

Considering horizontal equilibrium of the free body:

$$\Delta F_f = -\sigma_t t_w d_0 \sin(\phi)\cos(\phi) = -\sigma_t t_w d_0 \frac{\sin(2\phi)}{2}$$ **Equation 2-20**

Summing moments around point O:

$$\Delta F_f = -\frac{V_\sigma \cdot d_0}{D}$$ **Equation 2-21**

Equating Equation 2-20 and Equation 2-21, and substituting Equation 2-18 for sin(2ϕ) yields:

$$V_\sigma = \sigma_t \cdot t_w \cdot D \cdot \frac{1}{2 \cdot \sqrt{1 + \left(d_0 / D\right)^2}}$$ **Equation 2-22**

Equation 2-22 gives the vertical component of the tension field that occurs after web buckling. Shear is resisted in a beam-type manner prior to web buckling, and the vertical component of the tension field resists additional shear forces beyond the web-buckling load. So, the ultimate shear capacity of the plate girder is due to both beam action (V_τ) and tension field action (V_σ), and the ultimate shear load can be expressed as:

$$V_u = V_\tau\big|_{max} + V_\sigma\big|_{max}$$ **Equation 2-23**

Basler then makes two assumptions in order to compute these components of shear capacity. The first assumption is that the superposition of the beam and tension field components is ultimately limited by the state of stress that fulfills the von Mises yield criteria. The second assumption is that, prior to web buckling, applied shear is resisted

purely in a beam-type manner, but after that, V_τ remains constant and any postbuckling contribution to shear capacity must be due to tension field action. Therefore, the maximum beam-type shear resistance must correspond to the shear stress that will cause web buckling:

$$V_\tau = V_{cr} = \tau_{cr} \cdot D \cdot t_w = V_p \cdot \frac{\tau_{cr}}{\tau_y}$$ **Equation 2-24**

The shear buckling stress, taken from plate buckling theory, is given as:

$$\tau_{cr} = k \cdot \frac{\pi^2 \cdot E}{12 \cdot (1 - \nu^2)} \cdot \left(\frac{t_w}{D}\right)^2$$ **Equation 2-25**

Where:

ν = Poisson's ratio

k = shear buckling coefficient

Where:

$$k = 5.34 + \frac{4.00}{\left(d_0/D\right)^2} \quad \text{for } d_0/D \geq 1$$ **Equation 2-26**

$$k = 4.00 + \frac{5.34}{\left(d_0/D\right)^2} \quad \text{for } d_0/D < 1$$ **Equation 2-27**

Using the first assumption, the maximum tension field stress, σ_t, can be computed. This is the stress that can be added to the state of stress at web buckling that will fulfill the yield criteria. For an element at the neutral axis, the state of stress at web buckling is pure shear and $\tau_{xy} = \tau_{cr}$, as shown in Figure 2-10(a).

Special attention must be given to coordinate systems for this discussion. Subscripts x and y will be used to denote the fixed coordinate systems referring to the beam's horizontal and vertical axes, respectively. The u–v coordinate system is obtained by rotating the x and y axes counter-clockwise by an angle ϕ. Therefore, the u-axis corresponds with the line of action of the tension field stresses. At the critical buckling load, $\tau_{xy} = \tau_{cr}$, which can be expressed in u–v coordinates as:

$$\sigma_u = \tau_{cr} \cdot \sin(2\phi)$$ **Equation 2-28**

$$\sigma_v = -\tau_{cr} \cdot \sin(2\phi)$$ **Equation 2-29**

$$\tau_{uv} = \tau_{cr} \cdot \cos(2\phi)$$ **Equation 2-30**

These stresses are shown on the u-v axes in Figure 2-10(b).

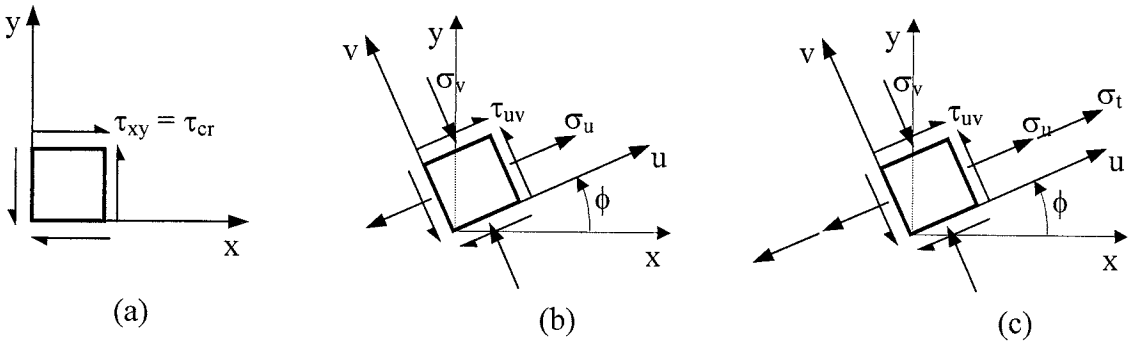

Figure 2-10. Neutral Axis States of Stress

After web buckling, the beam-type contribution to shear resistance is assumed to remain constant. At ultimate shear load, the maximum tension field stress, σ_t, acts on the element in addition to the stresses present at web buckling (see Figure 2-10(c)). Expressed in u–v coordinates, these stresses are simply:

$$\sigma_u = \tau_{cr} \cdot \sin(2\phi) + \sigma_t$$ **Equation 2-31**

$$\sigma_v = -\tau_{cr} \cdot \sin(2\phi)$$ **Equation 2-32**

$$\tau_{uv} = \tau_{cr} \cdot \cos(2\phi)$$ **Equation 2-33**

From these equations, it can be seen that the compressive stresses along the v-axis as well as the shear stresses in the u-v plane remain constant after web buckling. This phenomenon is observed when plotting these states of stress on Mohr's circle (Figure 2-11) as point v theoretically remains constant following web buckling.

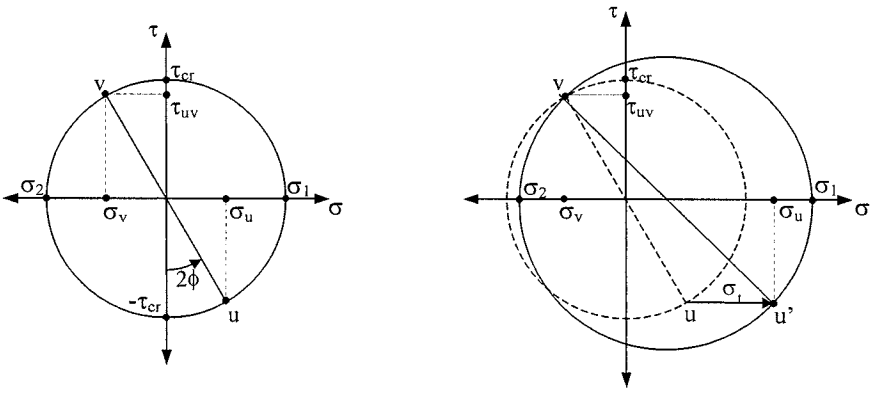

(a) Web Buckling Condition (b) Yield Condition

Figure 2-11. Mohr's Circle for Neutral Axis Element

Substituting the ultimate state of stress described in the above equations into von Mises' yield criteria:

$$\sigma_u^2 + \sigma_v^2 - \sigma_u \cdot \sigma_v + 3\tau_{uv}^2 - F_y^2 = 0$$ **Equation 2-34**

The following solution is obtained:

$$\frac{\sigma_t}{F_y} = \sqrt{1 + \left(\frac{\tau_{cr}}{F_y}\right)^2 \cdot \left[\left(\frac{3}{2} \cdot \sin(2\phi)\right)^2 - 3\right]} - \frac{3}{2} \cdot \frac{\tau_{cr}}{F_y} \cdot \sin(2\phi)$$ **Equation 2-35**

The ultimate shear load is computed using Equation 2-22, Equation 2-23, and Equation 2-24.

$$V_u = V_p \cdot \left[\frac{\tau_{cr}}{\tau_y} + \frac{\sqrt{3}}{2} \cdot \frac{\sigma_t}{F_y} \cdot \frac{1}{\sqrt{1 + \left(d_0/D\right)^2}}\right]$$ **Equation 2-36**

Where σ_t/F_y is given by Equation 2-35.

In order to simplify the computation, Basler approximates the von Mises yield condition with a linear function. For any state of stress between pure shear and pure tension, only a small portion of the yield criteria ellipse is needed (see Figure 2-12). This portion is then approximated with a straight line with the following equation:

$$\sigma_1 = F_y + \left(\sqrt{3} - 1\right) \cdot \sigma_2$$ **Equation 2-37**

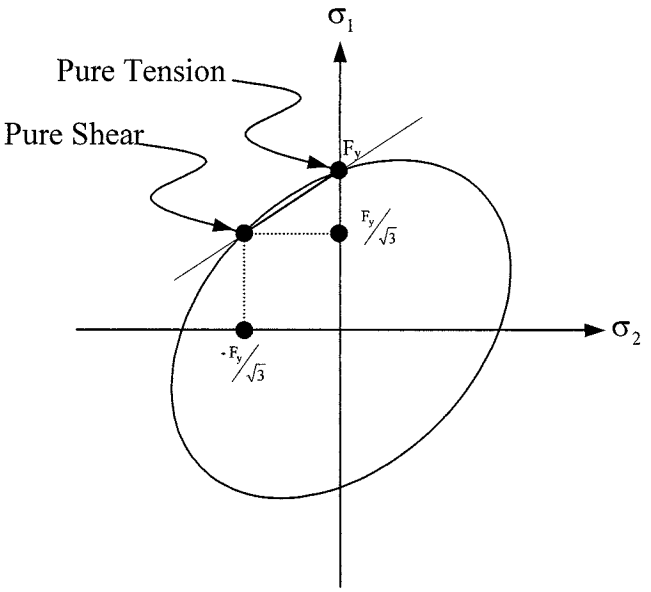

Figure 2-12. Yield Criteria Simplification

For the limiting case of $\phi = 45°$, σ_u from Equation 2-31 and σ_v from Equation 2-32 become principal stresses: $\sigma_1 = \tau_{cr} + \sigma_t$ and $\sigma_2 = -\tau_{cr}$. Substituting these values into the approximated von Mises yield criteria from Equation 2-37, we obtain:

$$\frac{\sigma_t}{F_y} = 1 - \frac{\tau_{cr}}{\tau_y}$$ **Equation 2-38**

Basler states that using Equation 2-38 instead of Equation 2-35 even when ϕ is not equal to 45° will be conservative since the approximate method underestimates the tension field stress, and the underestimation increases as ϕ decreases. A lower value of ϕ corresponds to a panel with a larger aspect ratio, d_0/D. In order for panels with large aspect

ratios to develop tension fields, larger shear displacements are required than those required by shear panels with smaller aspect ratios. Therefore, this approximation is not only a way to simplify computations, but also to provide an allowance for compatibility conditions for longer shear panels (Basler 1961a).

The ultimate shear force can be calculated from Equation 2-36 and Equation 2-38 as:

$$V_u = V_p \cdot \left[\frac{\tau_{cr}}{\tau_y} + \frac{\sqrt{3}}{2} \cdot \frac{1 - \frac{\tau_{cr}}{\tau_y}}{\sqrt{1 + \left(d_0 / D \right)^2}} \right] \qquad \textbf{Equation 2-39}$$

2.3.4 AASHTO's Tension Field Action Provisions

Basler's tension field theory has been adopted by AASHTO (1998) LRFD for design. For comparison, the design equation as published in AASHTO Article 6.10.6 for determining the total shear capacity of a transversely stiffened plate girder is:

$$V_n = V_p \cdot \left[C + \frac{0.87 \cdot (1 - C)}{\sqrt{1 + \left(d_0 / D \right)^2}} \right] \qquad \textbf{Equation 2-40}$$

with $C = \tau_{cr}/\tau_y$

AASHTO places three limitations on the tension field action provisions to ensure that they are properly applied. First, tension field action shear capacity is not allowed in the design of end panels of plate girders. The tension field anchors to the flanges and stiffeners in opposite corners of the shear panel, and since end panels do not have an adjacent shear panel one on side to anchor to, it is believed that the tension field cannot properly anchor to

the flange. Thus, without proper anchorage, the tension field cannot fully develop in end panels of plate girders.

The second limitation is that tension field action shear capacity cannot be used for design if: $\frac{d_0}{D} > \left(\frac{260}{D/t_w}\right)^2$

This is to ensure that the dimensions of the plate girder are reasonable and will permit the development of a tension field. This restriction keeps the shear panel from being too long, which would reduce the angle of inclination of the tension field, making the vertical component of the tension field negligible.

Finally, the third restriction imposed by AASHTO is that tension field action shear capacity may not be used for the design of hybrid plate girders. Hybrid plate girders inherently experience web yielding due to flexural stresses at high moment. When a hybrid girder is subjected to flexure, portions of the web are likely to yield prior to yielding of the flanges, since the flange material has higher yield strength than the web material (see Figure 2-13). This presents a potential anchorage problem for the tension field stresses. The primary concern is whether the tension field can properly anchor to the flanges and stiffeners through the portion of yielded web material near the flanges. Since a high shear load must be present in order to produce tension field stresses, and a high moment loading must be present to yield the web, this concern is applicable to areas with high-shear, high-moment loading. On a bridge, this is typically for continuous girders over interior piers.

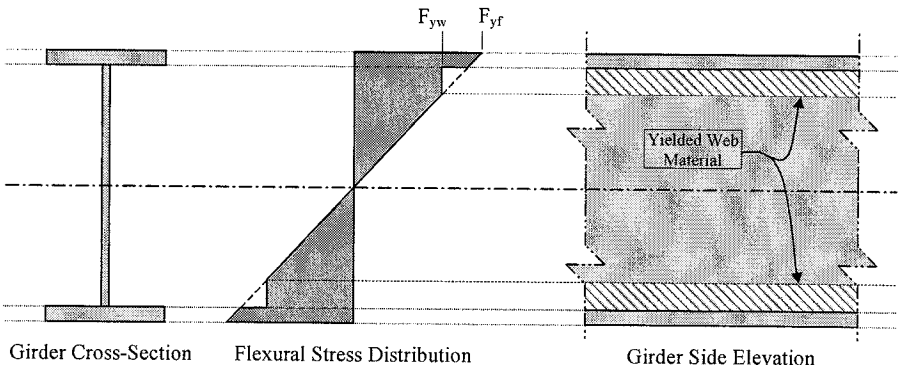

Figure 2-13. Web Yielding in Hybrid Girders

For those instances, where the use of tension field action is disallowed, the girder is restricted to the shear buckling capacity. The shear buckling capacity can typically be on the order of about half of the full shear capacity utilizing tension field action. While the first two of the three restrictions are straightforward, it seems counter-intuitive that a hybrid girder that uses higher strength flanges would have about half the shear capacity of a homogeneous girder of the same dimensions. To continue this investigation, the next section explores the current moment-shear interaction theory as well as a proposed moment-shear interaction curve for hybrid plate girders.

2.4 Moment-Shear Interaction

It is possible that the maximum bending moment and maximum shear occur at the same location in a girder. In order to ensure that a given cross section is not expected to

resist its full moment capacity and full shear capacity concurrently, moment-shear interaction reductions are included in current design practice (AASHTO 1998).

The accepted moment-shear interaction theory in AASHTO's 1998 design code is also based on research performed by Basler (1961b). A brief summary of Basler's derivation and results will be presented here, followed by the actual interaction curve as published by AASHTO. Also, a recently proposed (Barker et al 2002) lower-bound interaction diagram for hybrid girders will be presented.

2.4.1 Basler's Interaction Diagram

Basler begins his moment-shear interaction derivation by defining several reference moments, assuming a symmetrically proportioned girder (see Figure 2-14).

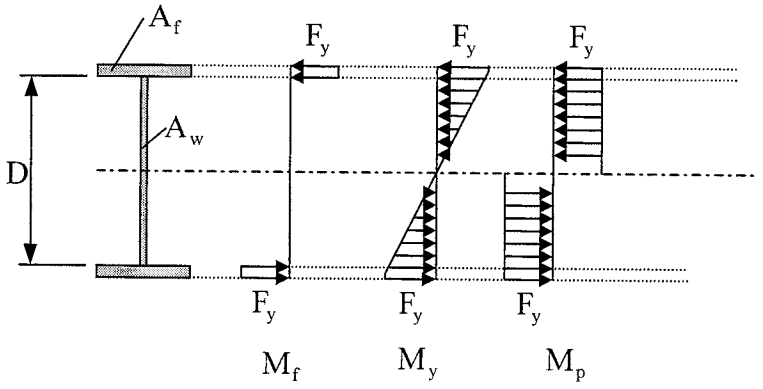

Figure 2-14. Basler's Reference Moments

The flange moment, M_f, is the moment carried by the flanges alone when fully yielded.

$$M_f = F_y \cdot D \cdot A_f \qquad \textbf{Equation 2-41}$$

Where:

M_f = flange moment

A_f = cross sectional area of one flange

The yield moment, M_y, is characterized by yielding at the centroid of the compression flange, and has a linear flexural stress distribution.

$$M_y = F_y \cdot D \cdot \left(A_f + \frac{A_w}{6} \right) = A_f \cdot F_y \cdot D \cdot \left(1 + \frac{A_w}{6A_f} \right)$$ **Equation 2-42**

The plastic moment, M_p, is the moment resistance provided by a fully yielded cross section.

$$M_p = F_y \cdot D \cdot \left(A_f + \frac{A_w}{4} \right)$$ **Equation 2-43**

In the following discussion, the applied moment, M, will be referred to in terms of the yield moment, M_y, by means of the proportion M/M_y. This is necessary to give meaning to the magnitude of the applied moment by comparing it with the girder's moment carrying capacity, as well as to simplify the discussion by using nondimensional quantities. The applied shear, V, will be expressed in terms of the ultimate shear force, V_n, in the proportion V/V_n for the same reasons. These ratios will be referred to as the relative (or normalized) moment and shear.

Basler's ultimate shear force is based on a web fully yielded in shear, and can be expressed as:

$$V_n = D \cdot t_w \cdot \tau_y = A_w \cdot \tau_y$$ **Equation 2-44**

Basler then creates a chart, plotting M/M_y vs. V/V_n. If the applied bending moment is small, the girder can reach it's full shear capacity, or $V/V_n = 1$. If the applied shear is maintained at this level and bending moment is increased, the flanges can resist all of the bending moment up until the flange moment, M_f. This is shown in Figure 2-15 as the vertical line at $V/V_n = 1$, for $0 \leq M/M_y \leq M_f/M_y$. One should note that this derivation assumes the flanges are properly braced in the lateral direction such that they are capable of reaching the yield stress.

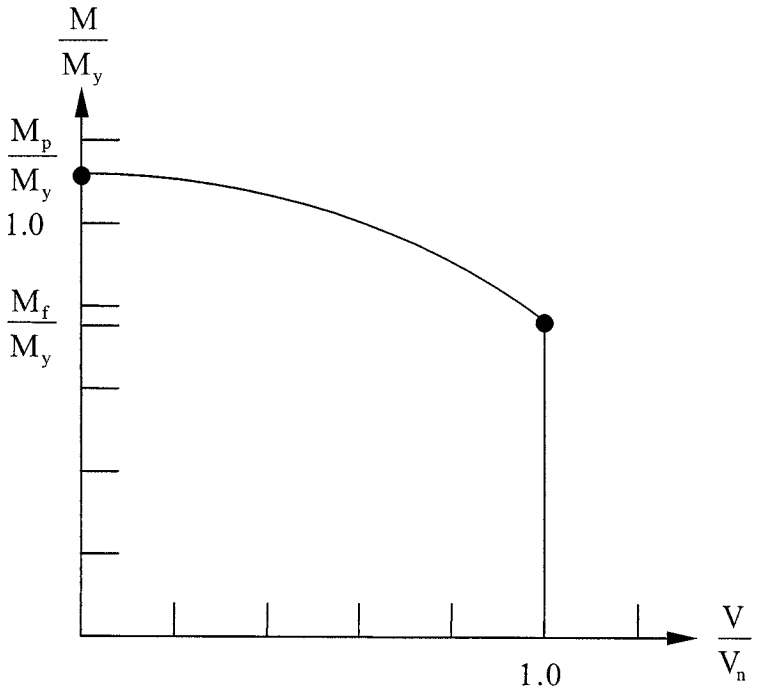

Figure 2-15. Basler's Moment-Shear Interaction Curve

Now, assume that the applied shear on the beam is small. In this case, the maximum moment the girder could experience is the plastic moment, M_p. Basler notes that the only portion of the interaction curve where bending moment affects shear capacity is between the

flange moment, M_f, and the plastic moment, M_p, so any interaction curve should pass through those points. Also, since a small shear force would have little effect on the moment carrying capacity of the girder, the interaction curve should be perpendicular to the M/M_y axis as V/V_n tends toward zero. Basler suggests the following interaction curve equation:

$$\left(\frac{V}{V_n}\right)^2 + \frac{M - M_f}{M_p - M_f} = 1 \qquad \textbf{Equation 2-45}$$

This equation assumes a stress distribution in which a central portion of the web is yielded in shear and resists no moment. The flanges and outer portions of the web are yielded due to flexural stresses and do not resist shear. This distribution is shown below in Figure 2-16.

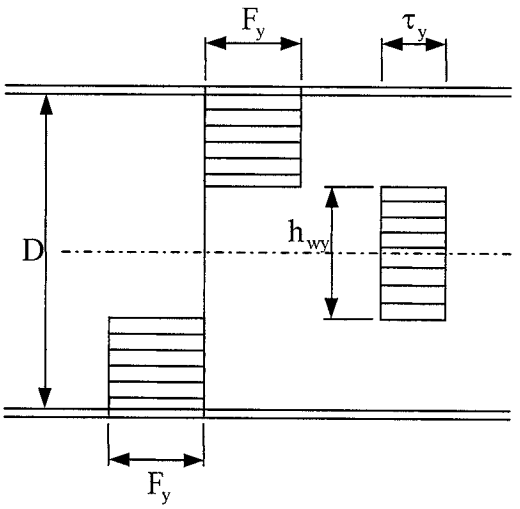

Figure 2-16. Basler's Assumed Stress Distribution for Interaction

The height of the central "effective" portion of the web resisting shear is h_{wy}, and it provides the following shear strength:

$$V_n' = h_{wy} \cdot t_w \cdot \tau_y$$ **Equation 2-46**

Where:

V_n' = shear capacity of central portion of web

h_{wy} = height of central portion of web yielded in shear

Dividing Equation 2-46 by Equation 2-44 and rearranging yields:

$$h_{wy} = \left(\frac{V_n'}{V_n}\right) \cdot D$$ **Equation 2-47**

The remainder of the web and the flanges are resisting bending moment and carrying no shear. The moment capacity provided by these portions of the cross section is:

$$M_n' = A_f \cdot F_y \cdot D + t_w \cdot F_y \cdot \left(\frac{D^2 - h_{wy}^2}{4}\right)$$ **Equation 2-48**

Substituting Equation 2-47 into Equation 2-48 and rearranging yields:

$$M_n' = A_f \cdot F_y \cdot D \cdot \left[1 + \frac{A_w}{4A_f} \cdot \left(1 - \left(\frac{V_n'}{V_n}\right)^2\right)\right]$$ **Equation 2-49**

Substitution of Equation 2-42 into Equation 2-49 gives:

$$M_n' = M_y \cdot \frac{1 + \frac{A_w}{4A_f} \cdot \left(1 - \left(\frac{V_n'}{V_n}\right)^2\right)}{1 + \frac{A_w}{6A_f}} \qquad \textbf{Equation 2-50}$$

It becomes obvious with Equation 2-50 that Basler's interaction curve is based on the ratio of A_w/A_f. Basler goes on to plot the interaction curve for various values of A_w/A_f, noting that most reasonably proportioned girders are in the range of $A_w/A_f \leq 2$. Using a value of 2 for A_w/A_f, the following equation is obtained:

$$\frac{M_n'}{M_y} = 1.125 - 0.375 \cdot \left(\frac{V_n'}{V_n}\right)^2 \qquad \textbf{Equation 2-51}$$

Equation 2-51 is then solved for 3 points to define the final curve (see Figure 2-17). First, setting the shear to zero, the value of relative moment is calculated as 1.125. Next, setting the relative shear to 1.0 yields a relative moment of 0.75. Finally, setting the relative moment equal to one, the relative shear is calculated to be $1/\sqrt{3} \approx 0.6$. Often, the geometry of a plate girder does not allow the plastic moment to be attained. In this case, part of the interaction curve will be cut off at the yield moment where $M/M_y = 1.0$.

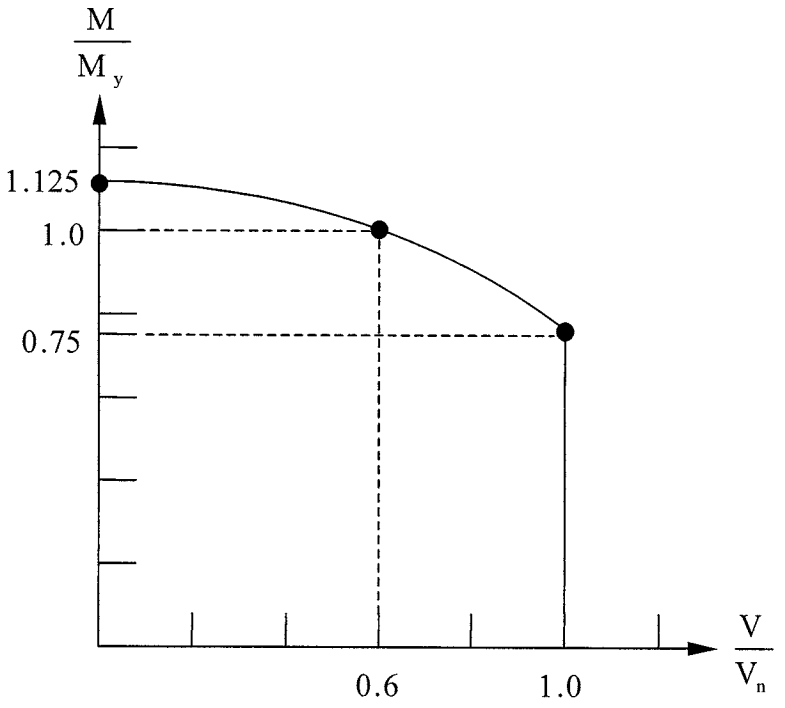

Figure 2-17. Basler's Moment-Shear Interaction Curve with Critical Values

2.4.2 AASHTO's Interaction Diagram

AASHTO has adopted a modified form of Basler's moment-shear interaction diagram for use in steel plate girder design. While Basler uses the yield moment, M_y, as the reference moment, AASHTO's relative moment is taken in reference to the nominal moment capacity of the girder, M_n. The nominal moment capacity of a plate girder is less than or equal to the yield moment, hence this is a conservative modification.

Another modification is the reference shear force. Basler's ultimate shear force is a "plastic" shear force; the cross sectional area of the web multiplied by the shear yield stress. AASHTO's interaction curve uses the nominal shear capacity of the girder including tension

field action as the reference shear. The nominal shear capacity of a plate girder is less than or equal to the plastic shear force of the slender web panel, so this modification is also conservative.

Since AASHTO uses the nominal moment capacity as the reference moment, the relative moment is limited to a value of 1.0. This ensures that the moment capacity is not exceeded, even at low shear loading. This modification also makes the interaction curve easier to use, by replacing a large part of the curve with a straight line.

Finally, AASHTO notes that the remaining portion of the curve is nearly linear, and it would be conservative and convenient to replace it with a straight line. So, the curve is replaced with a straight line between the points where the curve formerly intersected the limiting values of relative shear and moment (see Figure 2-18).

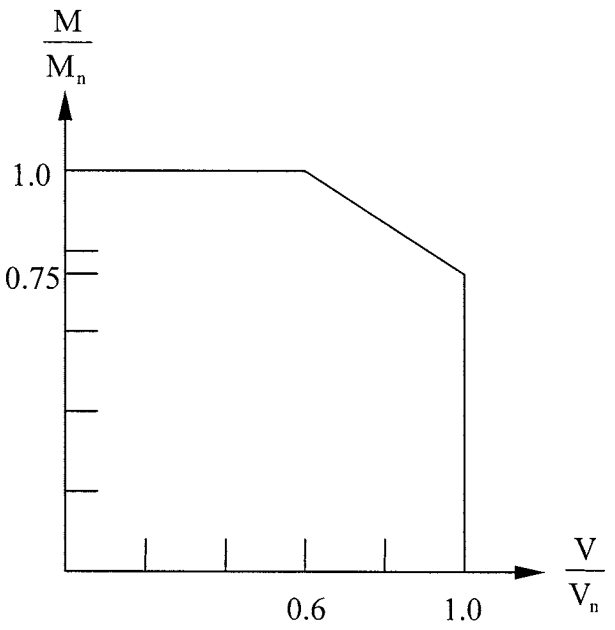

Figure 2-18. AASHTO's Moment-Shear Interaction Diagram

For application in design and analysis, the interaction diagram is reduced to one simple equation, sometimes referred to as the "R equation". When $M_u \geq 0.75\phi_f M_y$, the nominal shear capacity is reduced by the factor R, which is calculated as:

$$R = 0.6 + 0.4 \cdot \left(\frac{M_r - M_u}{M_r - 0.75 \cdot \phi_f \cdot M_y} \right)$$ **Equation 2-52**

Where:

ϕ_f = resistance factor for flexure = 1.0

M_r = factored flexural resistance = $\phi_f M_n$

M_u = factored applied moment

M_y = bending moment that initiates yielding of outermost fibers of flange

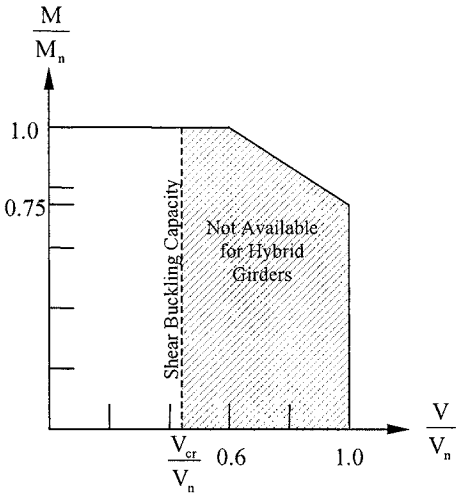

Note: V_n represents shear capacity if TFA applicable

Note: Shear buckling capacity varies with girder dimensions

Figure 2-19. Hybrid Girder Moment-Shear Interaction Restriction

As discussed in Section 2.3.4, AASHTO does not allow tension field action shear capacity to be used in the design of hybrid plate girders. This results in a large part of the moment-shear interaction diagram being unavailable to hybrid girders (see Figure 2-19). While there may be justifiable concern for areas subjected to high shear and high moment loading, the penalty as concerning the interaction diagram is very conservative. Consider a hybrid plate girder that is subject to a high shear loading but small bending moment. This is the situation for a simply supported bridge girder near an abutment. In this case, there is no concern for web yielding, so tension field anchorage would not be a problem. The girder should be able to attain its full shear capacity, including tension field action. The Series I tests (Schreiner 2001 and Rush 2001) demonstrate TFA is applicable to hybrid girders subject to low moment. The Series II tests and analyses (Zentz 2002 and Davis 2002) show that tension field action is also applicable to hybrid girders subject to high moment. Hurst (2000) developed a lower-bound conservative moment-shear interaction equation for hybrid girders as is shown in the next section.

2.4.3 Proposed Hybrid Moment-Shear Interaction Diagram

With the intent to make hybrid designs more economical by utilizing tension field action, and therefore reducing the required number of transverse stiffeners, a new moment-shear interaction diagram has been derived to accommodate hybrid girders. The interaction curve was developed using Basler's original interaction equations and modifying them to account for yield strength differences between the web and flanges (Hurst 2000). A brief summary of Hurst's derivation follows.

First, a ratio of the yield strengths of the flanges and web is defined:

$$\beta = \frac{F_{yf}}{F_{yw}} \geq 1$$ **Equation 2-53**

Where:

F_{yf} = flange yield strength

F_{yw} = web yield strength

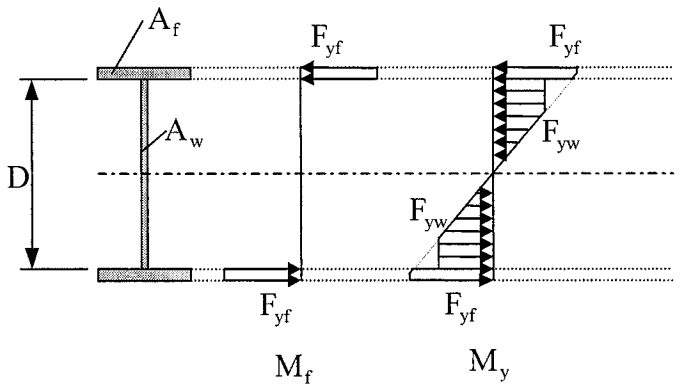

Figure 2-20. Reference Moments for Modified Basler Theory

Like Basler's derivation, some reference moments (Figure 2-20) are now defined. The maximum bending moment that can be carried by the flanges alone is called the flange moment, and denoted M_f. Approximating the distance between flange centroids as the web depth, D, the flange moment can be expressed as:

$$M_f = A_f \cdot F_{yf} \cdot D = A_f \cdot \beta \cdot F_{yw} \cdot D$$ **Equation 2-54**

The yield moment, denoted M_y, is defined as the moment that initiates yielding of the centroid of the compression flange. Since we are dealing with a hybrid girder with $F_{yw} \leq F_{yf}$, the web will yield before the flange yield moment is reached. In order to account for the nonlinear stress effects of web yielding, AASHTO's hybrid reduction factor, R_h, is applied here.

$$M_y = R_h \cdot S_x \cdot F_{yf} = R_h \cdot S_x \cdot \beta \cdot F_{yw} \qquad \textbf{Equation 2-55}$$

Where:

S_x = section modulus $\approx A_f \cdot D + \frac{A_w \cdot D}{6}$

Substituting the approximated section modulus into Equation 2-55:

$$M_y = A_f \cdot D \cdot \beta \cdot F_{yw} \cdot R_h \cdot \left(1 + \frac{A_w}{6A_f}\right) \qquad \textbf{Equation 2-56}$$

Once again, a stress distribution is assumed such that a central portion of the web is yielded due to shear stress and cannot resist any flexure. The remainder of the cross section is yielded due to flexural stresses and provides no resistance to shear (see Figure 2-21).

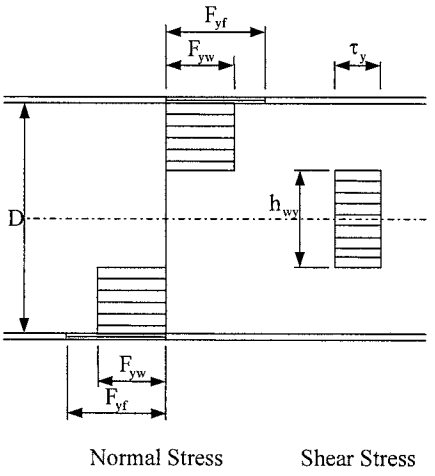

Figure 2-21. Assumed Stress Distribution for Modified Basler Theory

Through calculations identical to those leading up to Equation 2-47, the height of the central portion of the web is again found to be:

$$h_{wy} = \left(\frac{V_n'}{V_n}\right) \cdot D$$ **Equation 2-57**

The nominal moment capacity of the girder, which includes no contribution from the central portion of the web, is calculated to be:

$$M_n' = A_f \cdot \beta \cdot F_{yw} \cdot D + t_w \cdot \left(\frac{D^2}{4}\right) \cdot F_{yw} - t_w \cdot \left(\frac{h_{wy}^{\ 2}}{4}\right) \cdot F_{yw}$$ **Equation 2-58**

Substituting Equation 2-57 into Equation 2-58 and rearranging yields:

$$M_n' = F_{yw} \cdot A_f \cdot D \cdot \left[\beta + \frac{A_w}{4A_f} \cdot \left(1 - \left(\frac{V_n'}{V_n} \right)^2 \right) \right]$$ **Equation 2-59**

Substituting Equation 2-56into Equation 2-59 gives:

$$M_n' = M_y \cdot \frac{\beta + \left(\frac{A_w}{4A_f} \right) \cdot \left(1 - \left(\frac{V_n'}{V_n} \right)^2 \right)}{\beta \cdot R_h \cdot \left(1 + \frac{A_w}{6A_f} \right)}$$ **Equation 2-60**

Again, assuming a practical upper limit of $A_w/A_f = 2$, Equation 2-60 becomes:

$$M_n' = M_y \cdot \frac{\beta + \frac{1}{2} \cdot \left(1 - \left(\frac{V_n'}{V_n} \right)^2 \right)}{\frac{4}{3} \cdot \beta \cdot R_h}$$ **Equation 2-61**

Equation 2-61 then simplifies as:

$$\frac{M_n'}{M_y} = \frac{3}{4R_h} \cdot \left[1 + \frac{1}{2\beta} \cdot \left(1 - \frac{V_n'}{V_n} \right)^2 \right]$$ **Equation 2-62**

Equation 2-62 is the final equation for the proposed "Modified Basler Interaction Curve" proposed by Hurst. This is the hybrid equivalent of Basler's interaction equation, given as Equation 2-51. The curve for 50-70 ksi hybrids is plotted below in Figure 2-22, along with the original Basler interaction curve for comparison.

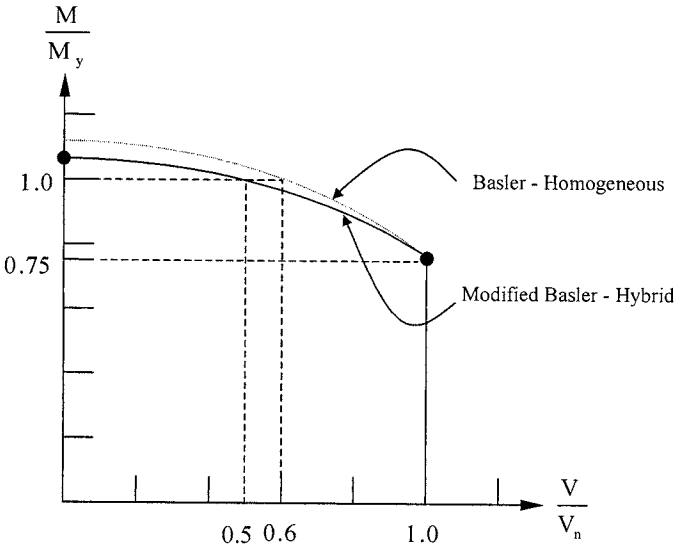

Figure 2-22. Modified Basler Interaction Curve for 50-70 Hybrid Girders

Hurst (2000) then examined the interaction equation for varying steel combinations and linearized the interaction diagram for convenience (see Figure 2-23). The maximum moment is again limited to the nominal moment capacity. Similar to the current interaction diagram, the hybrid interaction diagram limits the applied moment to 75% of the nominal moment capacity when the applied shear is equal to the nominal shear capacity.

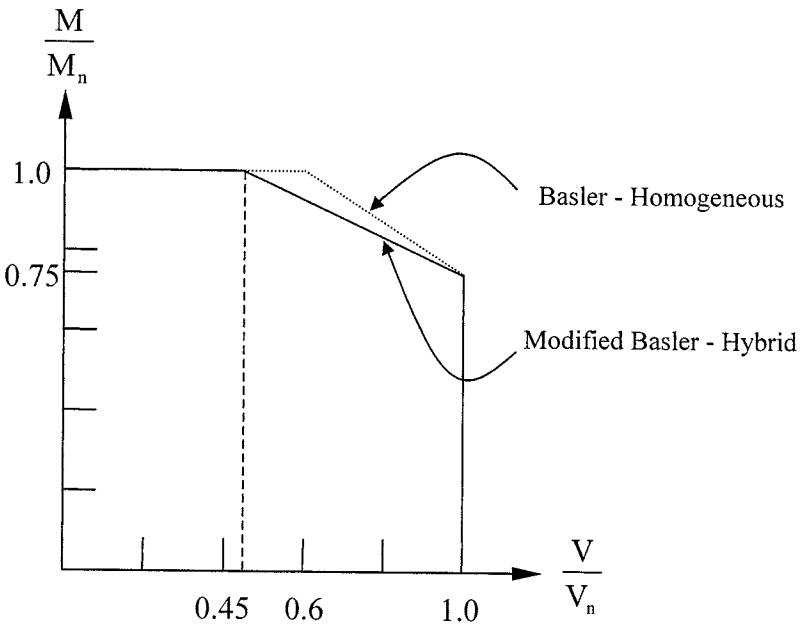

Figure 2-23. Modified Basler Interaction Diagram for General Hybrid Girders

The difference between the proposed hybrid interaction diagram and the currently accepted homogeneous interaction diagram is apparent when the applied moment is taken to be equal to the nominal moment capacity. At this load level there is a concern for web yielding, and the normalized shear cannot attain the same level as that of a homogenous girder ($V/V_n = 0.6$). Through a study of reasonable steel combinations, a value of $V/V_n = 0.45$ was selected as conservative and adequate as a limit when $M/M_n = 1.0$. For use in design and analysis, the reduction equation in AASHTO for hybrid girders could be expressed as:

$$R = 0.45 + 0.55 \cdot \left(\frac{M_r - M_u}{M_r - 0.75 \cdot \phi_f \cdot M_y} \right)$$ **Equation 2-63**

When $M_u \geq 0.75\phi_f M_y$, the nominal shear capacity of the hybrid girder is reduced by the factor R, as calculated above, to account for moment-shear interaction.

2.5 Summary

The necessary background information concerning the strength of plate girders subject to concurrent shear and bending has been presented, along with the limitations imposed by AASHTO concerning hybrid girders. These limitations are believed to be over-conservative, so a new moment-shear interaction curve for hybrid girders was presented. In the following chapters, experimental testing to validate the proposed interaction curve is documented. The test setup and procedure will be explained in the next chapter.

Chapter 3 - Test Specimens and Theoretical Behavior

3.1 Introduction

Hurst (2000) outlined the experimental tension field action test setup, which is designed to demonstrate tension field action in and the moment shear interaction behavior of hybrid girders. In order to verify TFA and validate AASHTO's or Hurst's proposed hybrid moment-shear interaction curve, several tests are required with varying levels of applied shear and bending moment. The designed tests plot on Hurst's interaction diagram as shown in Figure 3-1. Tests 1 – 3 (two identical test 3 were planned, labeled 3a and 3b) are designated as Series I tests, described in Section 3.2. The remainder of the tests are referred to as Series II and are described in Section 3.3.

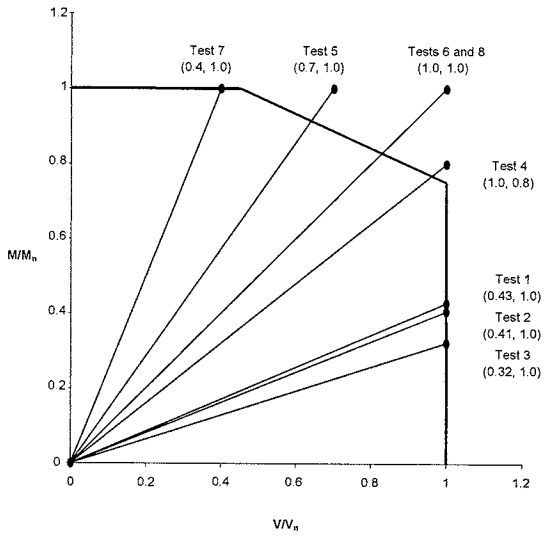

Figure 3-1. Target Moment & Shear Ratios for Test Girders

The test girders are designed as ½-scale plate girders that represent reasonable plate girder proportions. All of the test girders are of the same cross-sectional dimensions, shown in Figure 3-2. Each girder has a shear test panel with an aspect ratio of 1.5, which is designed to be the weakest shear panel in the girder to ensure failure at that location. The aspect ratio of 1.5 was chosen so that the tension field action contribution to shear capacity is approximately equal to the shear buckling capacity of the girder. The individual girders for the Series I and Series II tests will be discussed in their respective sections of this chapter.

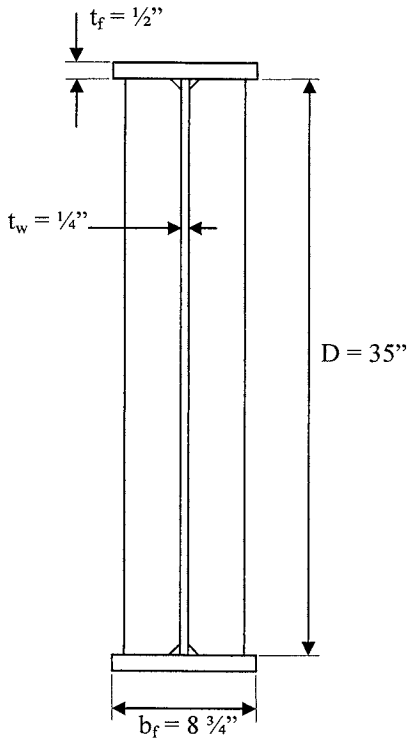

Figure 3-2. Test Girder Cross Section

3.2 Series I Test Specimens

The objective of the Series I tests was to demonstrate that tension field action shear capacity is applicable to hybrid girders subject to low moment-high shear loading. In order to validate the experiment, the same setup and instrumentation was used to test both homogeneous and hybrid girders. Four girders were included in Series I testing: two identical 50-70 hybrid girders, one homogeneous 50 ksi girder, and one homogeneous 70 ksi girder. All four girders had identical dimensions and instrumentation.

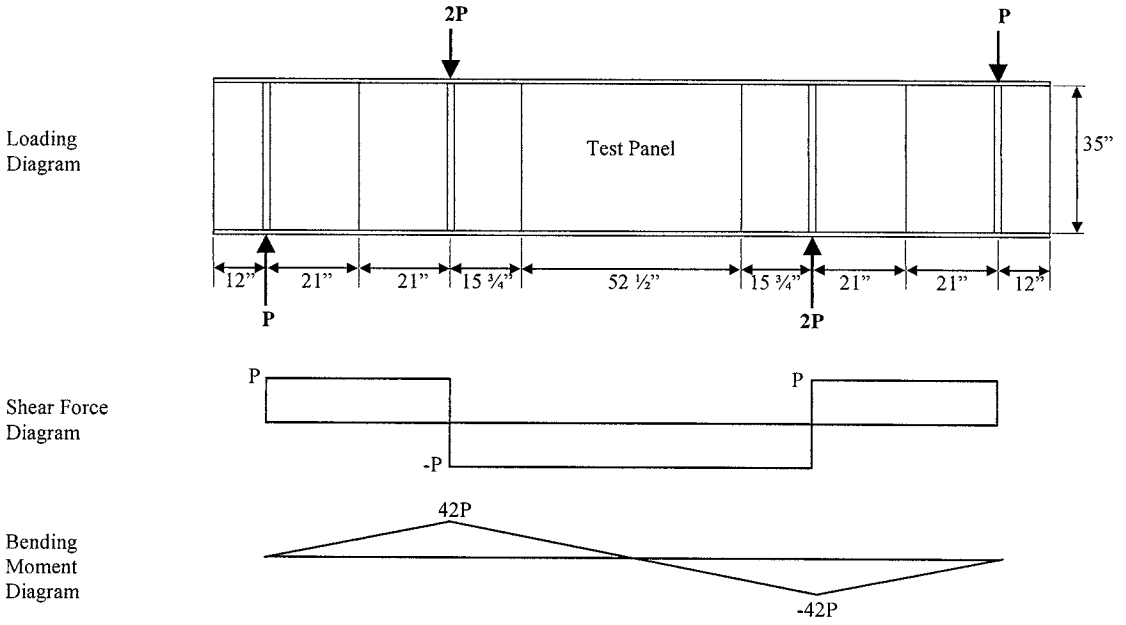

Figure 3-3. Series I Testing Configuration

The Series I test setup was designed to produce a state of low moment-high shear in the centrally located test panel. To achieve this loading, a reversed four-point bending loading diagram was selected (see Figure 3-3). Two pairs of hydraulic actuators were used to apply loads to the ends of the test girders. One pair of these actuators was hung from a steel load frame, while the other pair of actuators was mounted on the structural strong-floor of the testing facility. A cylindrical steel roller bearing mounted on a concrete pedestal provided the upward reaction shown on the loading diagram. Another steel roller bearing mounted on a "hold-down" beam provided the downward reaction. The hold-down beam was hung between two steel load frames, as shown in Figure 3-4.

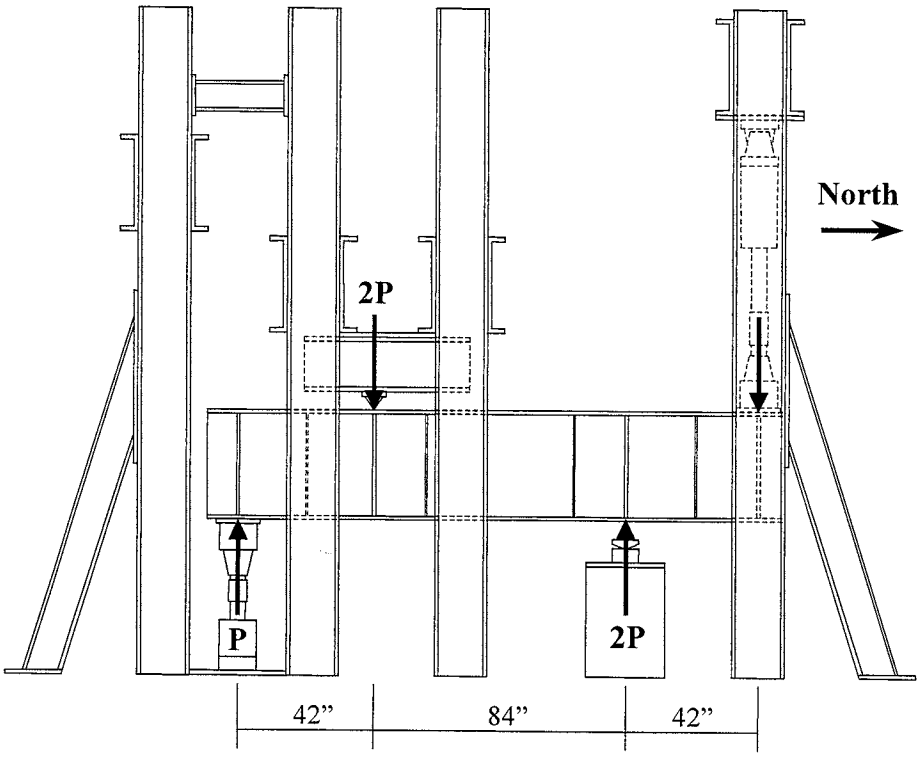

Figure 3-4. Series I Testing Structure

Instrumentation of the test girder included bondable linear and rosette strain gauges to record strains experienced by the girder. String potentiometers, or string pots, were used to record lateral web deflections in the test panel throughout the test. The actuators used to apply load to the test girders are equipped with load cells to record applied load, as well as LVDT's to record deflection of each actuator. As the instrumentation of the Series I girders is identical to that of the Series II girders, a description of the test apparatus and instrumentation will be presented in the Series II Sections 3.3.2 and 3.3.3.

Series I testing was performed in the spring of 2001 at the University of Missouri's Remote Testing Facility (RTF). Results from Series I testing are published in two separate theses (Schreiner 2001, Rush 2001). Schreiner's thesis documents the testing procedure and verifies that the hybrid girder's shear capacities were accurately predicted by AASHTO's current tension field action design equations. Rush's thesis interprets the experimental data and compares it to Basler's (1961a) tension field action theory, concluding that tension field action stresses are present in hybrid girders and reasonably predicted by Basler's theory. Note that these results only apply to low moment-high shear loading. The more general case of combined shear and bending is investigated herein with the Series II tests.

This chapter and Chapter 4 will concentrate on the Series II (tension field action with moment-shear interaction) in the detailed presentation and anlyses. The Series II tests demonstrate the behavior that justify the results and conclusions. Only the overall results of the Series I tests will be presented. The Series I test results and detailed analyses are contained in Schreiner (2001) and Rush (2001).

3.3 Series II Test Specimens

The objective of the Series II tests is to investigate tension field action behavior in hybrid plate girders subject to combined shear and bending. Six test girders were constructed and tested at the University of Missouri's Remote Testing Facility. The tests are designated Tests 4 – 8 on Figure 3-1, with two identical girders for Test 6, referred to as Tests 6a and 6b. The following discussion will address the test girders, test design, and instrumentation.

Series II testing was performed in the spring of 2002 at the University of Missouri's Remote Testing Facility (RTF). Results from Series II testing are published in two separate theses (Zentz 2002 and Davis 2002). Davis' thesis documents the testing procedure and verifies that the hybrid girder's shear capacities were conservatively predicted by AASHTO's current and Hurst's modified tension field action design equations. Zentz's thesis interprets the experimental data and compares it to Basler's (1961a and 1961b) tension field action theory, concluding that tension field action and moment-shear interaction stresses in hybrid girders are reasonably predicted by Basler's theory. Note that these results apply to moment-high shear interaction loading.

3.3.1 Test Girders

All Series II test girders are designed with the test panel adjacent to a central bearing stiffener, as shown in Figure 3-5. Excluding the test panel, each girder uses a short transverse stiffener spacing to ensure that the test panel is the weakest shear panel in the girder.

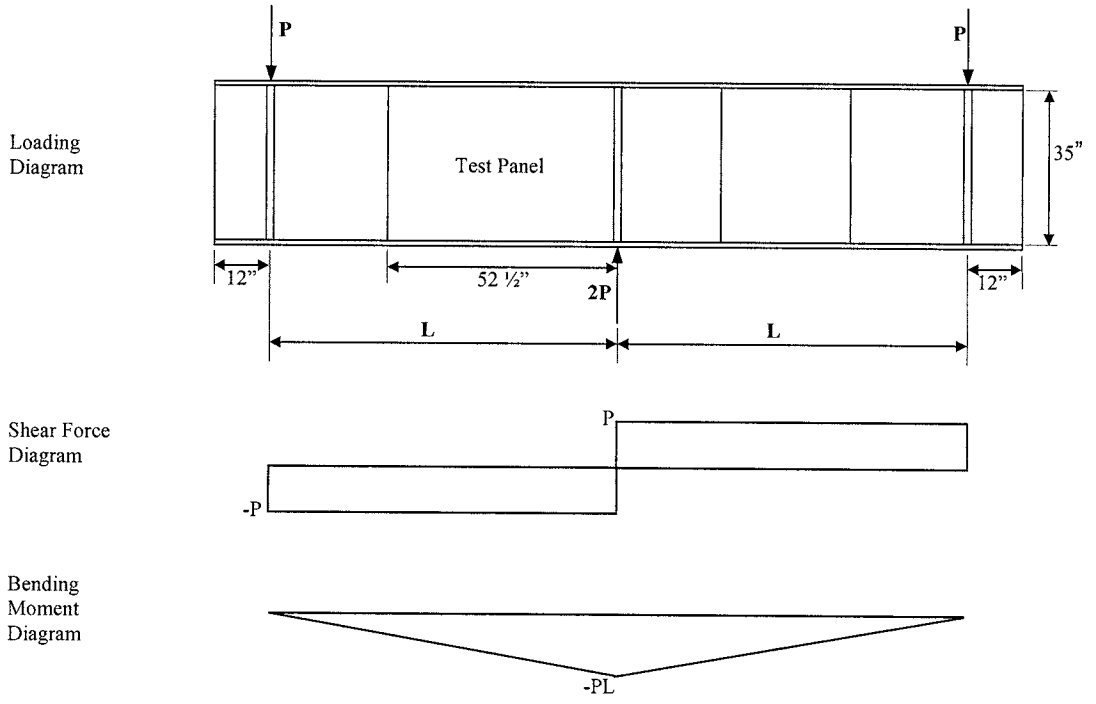

Figure 3-5. Series II Testing Configuration

In order to achieve varying levels of bending moment at the test panels of the six girders, the moment arm from the actuator to the test panel was varied. Unlike the girders used in the Series I tests, Series II girders are not all the same length. Appropriate lengths were chosen to achieve the levels of normalized shear and moment prescribed by Hurst (2000). These lengths and other girder specifications are given in Table 3-1.

Table 3-1. Series II Girder Specifications

Girder #	Girder Type	Target M/M_n	Target V/V_n	L (in)
4	Hybrid 50-70	0.8	1.0	65
5	Hybrid 50-70	1.0	0.7	116
6	Hybrid 50-70	1.0	1.0	81
7	Hybrid 50-70	1.0	0.4	200
8	Homo. 50 ksi	1.0	1.0	62

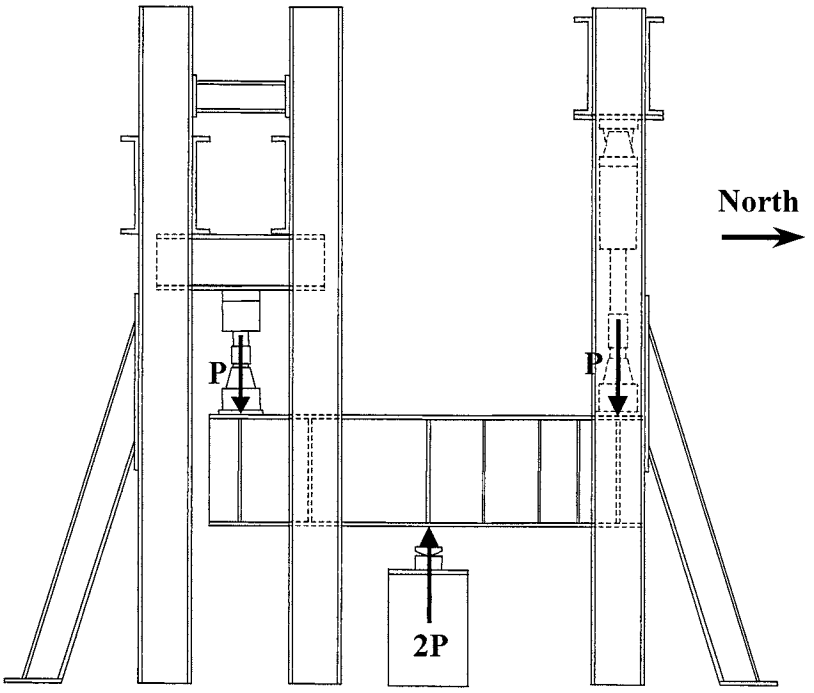

Figure 3-6. Series II Short Girder Setup

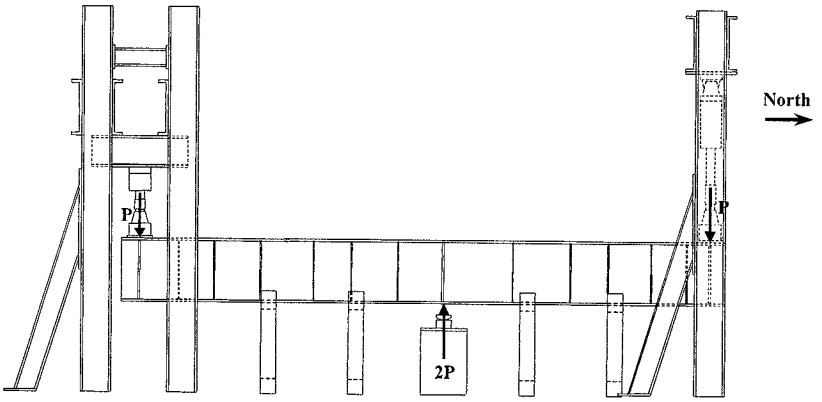

Figure 3-7. Series II Long Girder Setup with Intermediate Lateral Bracing

3.3.2 Test Design

The general test setup for Series II testing includes two pairs of hydraulic actuators hung from steel load frames, a cylindrical steel roller bearing mounted on a concrete pedestal, and lateral bracing. General test setups for short and long girders are shown in Figure 3-6 and Figure 3-7, respectively.

Each of the load frames consist of two W14x132 columns, connected near the top by two specially designed cross beams. Three load frames are used for the Series II tests, along with up to two pairs of diagonal braces for stability. These load frames are fastened into the RTF's structural strong-floor. The strong-floor is an isolated, four-foot thick, steel-reinforced concrete slab with threaded steel tie-down holes on a four-foot grid pattern. Each tie-down hole has a rated uplift capacity of 120 kips.

The general setup remains the same for all of the Series II tests, but since the lengths of the test girders vary, the setup must to be lengthened or shortened accordingly.

This is accomplished in two steps: moving entire load frames, and moving only actuators. The north pair of actuators are mounted on a single steel load frame with diagonal braces. This load frame, along with the actuators, can be lifted with an overhead crane and moved in increments of 4 feet (the tie-down spacing of the strong-floor). Moving the south actuators makes finer length adjustments to the test setup. Each of these actuators is mounted to a heavy steel beam that spans two load frames, as shown in Figure 3-6 and Figure 3-7.

Four hydraulic actuators are used to apply loads to the test girders. Each actuator has a rated capacity of 110 kips under static loading. The actuators are equipped with load cells and LVDT's to record load and displacement data for each actuator. Since the load required to fail the test girders is approximately 200 kips, the actuators are grouped into pairs by fastening a stiffened steel "spreader beam" across the swivel heads of the actuators. Load from the pair of actuators is then transferred to the test girder through the spreader beam as shown in Figure 3-8. The actuators provide the downward forces shown on the loading diagram (see Figure 3-5).

The upward reaction force shown on the loading diagram is provided by a steel roller bearing mounted on a reinforced concrete pedestal. The pedestal may be moved to accommodate any length of test girder. Besides serving as a mount for the bearing, the pedestal also provides lateral bracing at the bearing location. Two sliding steel sections, one on each side of the girder, clamp the girder into place by resting against the bearing stiffener near the compression flange (see Figure 3-9). The clamping sections are left in a "loose-fit" situation to ensure they only resist lateral load.

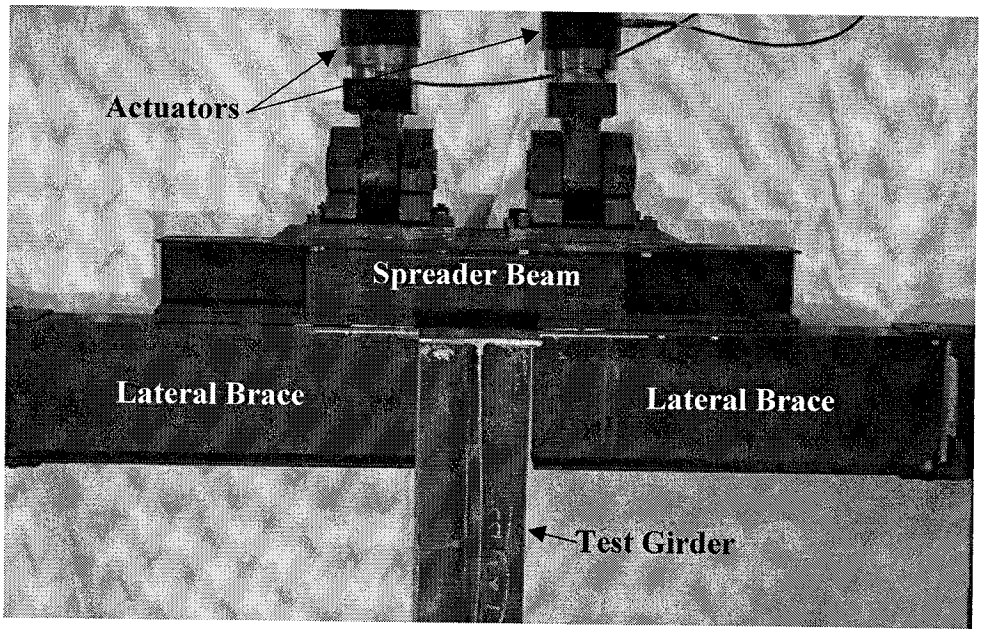

Figure 3-8. Load Application to Test Girder

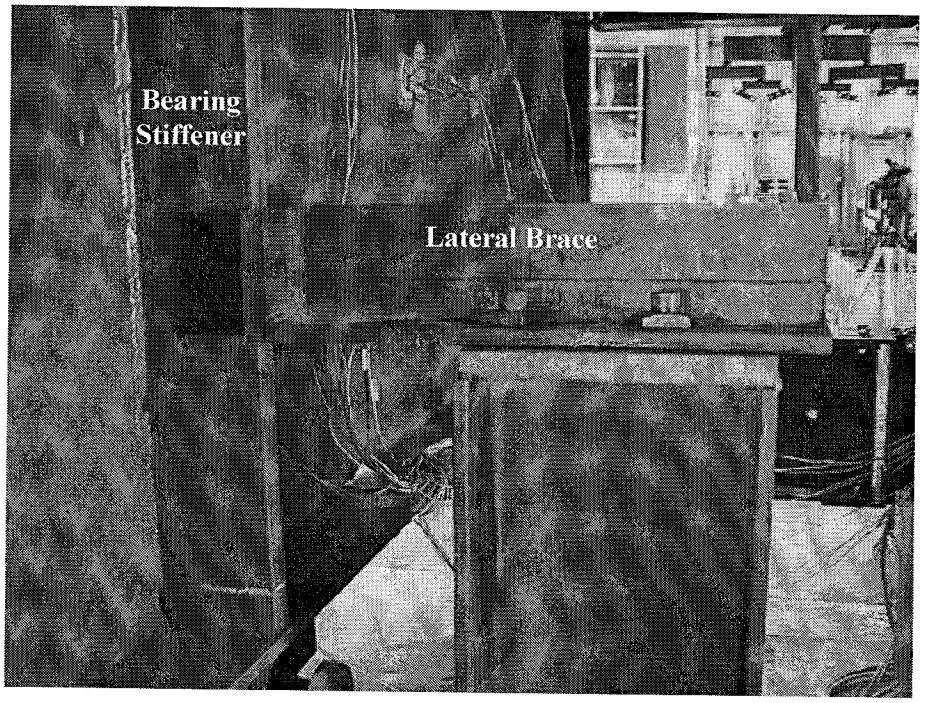

Figure 3-9. Lateral Bracing at Concrete Pedestal.

Lateral bracing was provided to all test girders at the actuator locations. The actuator lateral bracing not only needs to provide lateral support, but it also has to allow vertical displacement. This is accomplished by using horizontal brace members between the test girder and the load frame, with rollers on the outer end of the braces. Upper and lower braces are provided at each end of the test girder. The upper lateral bracing system consists of two braces, one on each side of the girder, as shown in Figure 3-8. The upper braces fasten to the spreader beam on the actuators, and steel clips bolted to the braces clamp the test girder in place. The lower lateral brace is a single piece with rollers on each end. This brace is clamped directly to the test girder using steel clips like those used on the upper bracing. The lateral bracing is tight-fit in the load frame, with the rollers bearing on steel plates supported by the load frame.

While the lateral bracing provided only at loading points is sufficient for the shorter test girders, additional lateral bracing is required for the two longer girders. For this purpose, special intermediate lateral braces were installed. The intermediate braces resemble C-clamps turned on their backs (see Figure 3-10). The braces are fastened to the strong-floor using the floor's tie-down holes. The braces then fasten to the compression flange of the test girder using sliding steel clamps. Lubricated bearing plates allow vertical and axial deflections of the girder while restricting lateral movement.

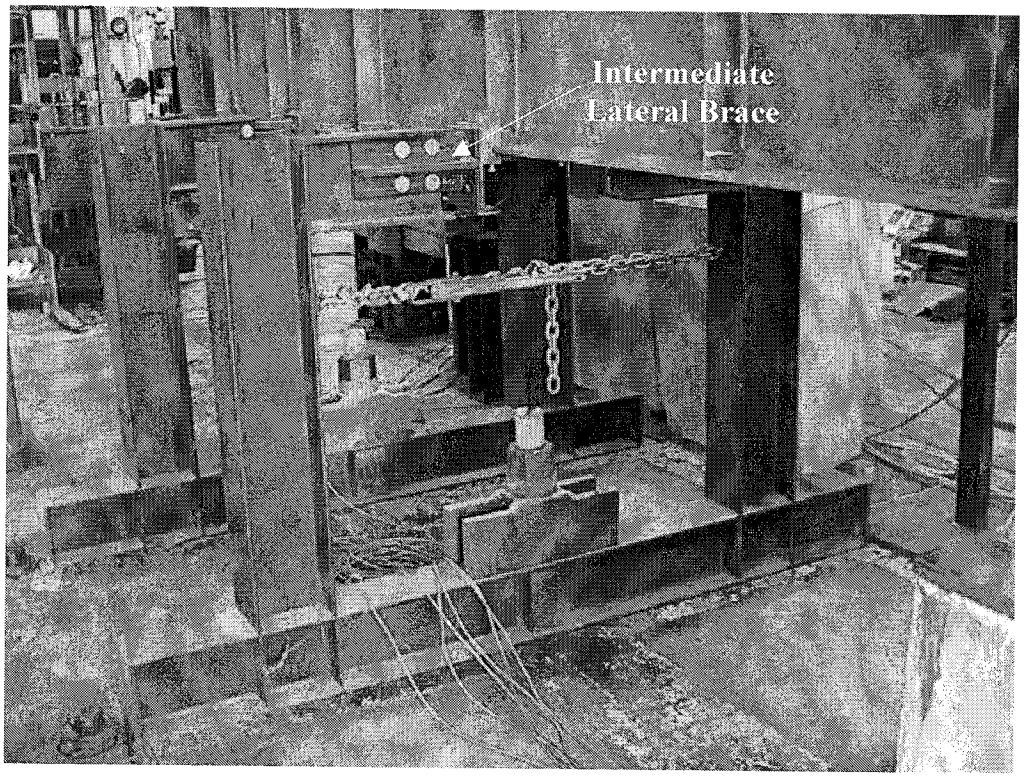

Figure 3-10. Intermediate Lateral Bracing used for Long Test Girders

3.3.3 Instrumentation

In order to record the behavior of the test girder during testing, the test setup included several types of instrumentation. As noted in Section 3.2, the instrumentation used for Series II testing is identical to that of the Series I tests. In addition to the actuators' load cells and LVDT's mentioned in Section 3.3.2, other types of instrumentation were installed to provide more data on the tension field action behavior of the test girders.

To detect anchorage of tension field action stresses, bondable linear strain gauges are installed on flanges and transverse stiffeners. Linear strain gauges, shown in Figure 3-11, are used to provide strain data along the axis of the strain gauge, so they are well suited for use when the direction of the strains is known and constant. However, linear gauges provide information along the axis of the gauge only.

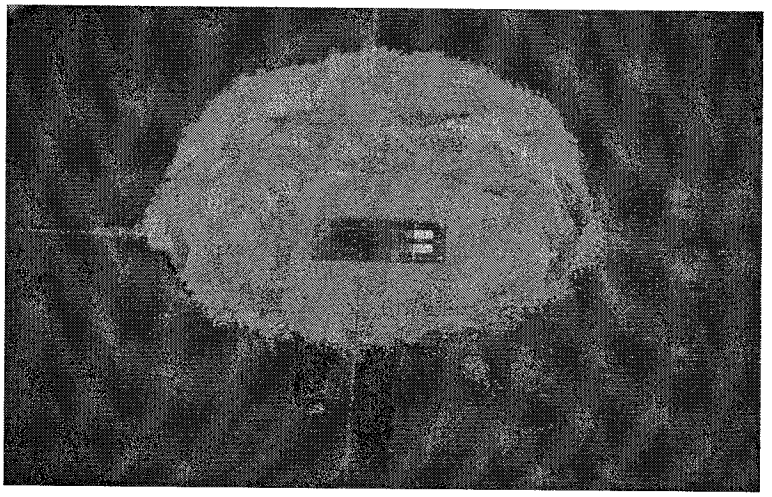

Figure 3-11. Linear Strain Gauge

More complete strain information is required for the web panel, so bondable rosette strain gauges are used to record strain data from the web. Rosette strain gauges consist of three linear strain gauges arranged such that a complete state-of-strain can be inferred from the data. Several types of rosette gauges are available, but rectangular rosettes were selected for this application. These gauges consist of three linear gauges arranged such that one gauge is aligned with the axis of the rosette and the other gauges are rotated 45° above and below the first gauge (see Figure 3-12). The rosette strain gauge provides information on the complete state of strain in the plane of the gauge.

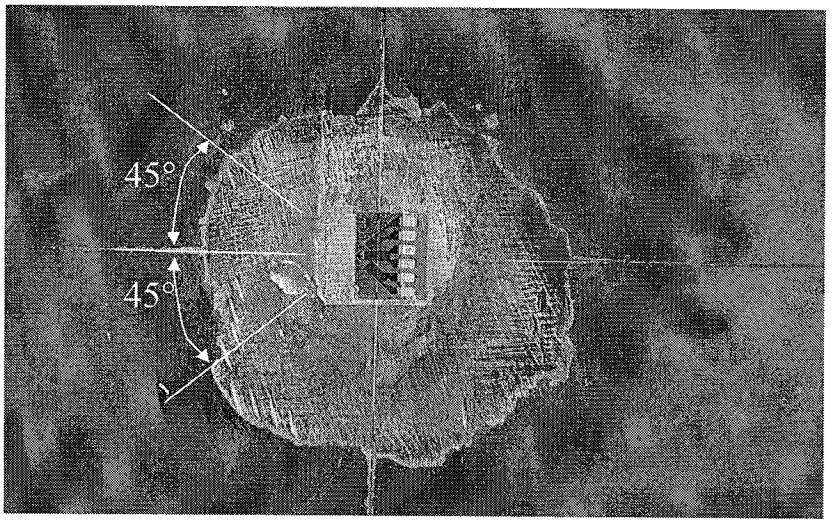

Figure 3-12. Rectangular Rosette Strain Gauge

In order to track the out-of-plane distortion expected due to web buckling, six string pots were attached to the web panel. The string pots are mounted on a frame that is attached to the test girder's flanges. This eliminates erroneous web deflection data due to relative displacements between the web panel and the string pot.

Out-of-plane effects regarding strain gauges are resolved by mirroring the strain gauge placement on either side of the test panel. By averaging the data taken from gauges on either side of the test panel, out-of-plane effects due to web buckling can be eliminated.

Strain gauge and string pot locations are shown in Figure 3-13 for the east face and Figure 3-14 for the west face of the test panel.

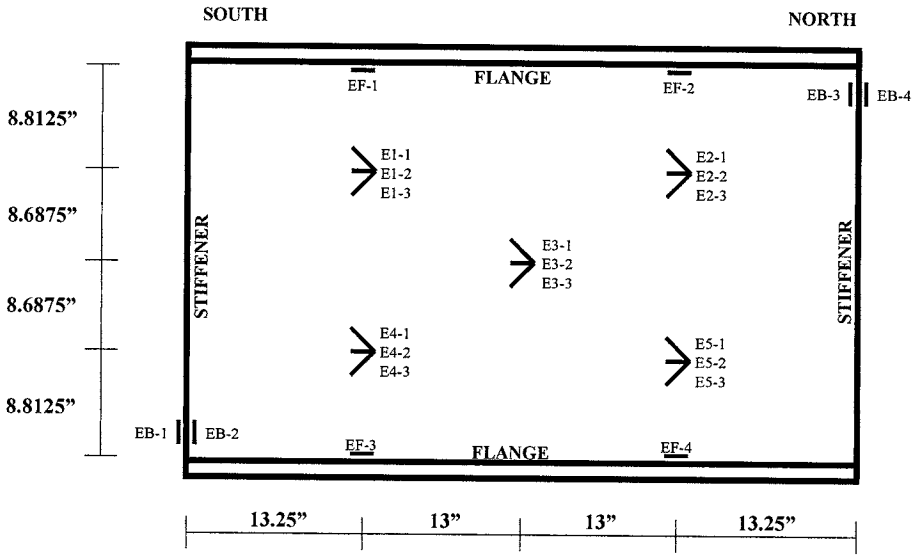

Figure 3-13. Strain Gauge Locations on East Face of Test Panel

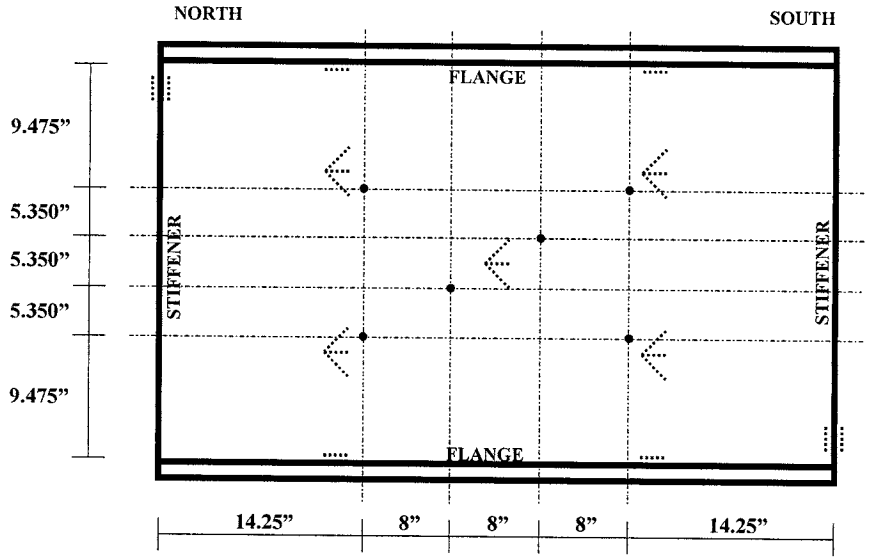

Figure 3-14. Strain Gauge and String Pot Locations on West Face of Test Panel

3.4 Summary of Test Specimens

Tension field action and existing and proposed hybrid moment-shear interaction diagrams are to be verified by two series of tests. Series I tests investigate the presence of tension field action stresses in hybrid plate girders subject to low moment-high shear loading. Series II tests will determine the tension field action behavior of hybrid plate girders subject to combined shear and bending. Using the testing procedures and data from the instrumentation described in this chapter, the validity of TFA and moment-shear interaction will be demonstrated.

3.5 Theoretical Data Analysis

3.5.1 Introduction

The purpose of this section is to describe in detail the process used to interpret the experimental data collected from Series II testing. In order to give meaning to the experimental data, theoretical stress values are calculated for reference against the experimental stresses. The theoretical stresses are calculated using Basler's (1961a) tension field action theory as outlined in Chapter 2. Experimental stresses are calculated from strain data recorded during testing. The methods used to calculate theoretical and experimental stresses will be shown in detail and example calculations given. Using the methods outlined in this chapter, the theoretical and experimental stresses will be compared in Chapter 4 to determine the effectiveness of tension field action in hybrid plate girders subject to concurrent bending and shear.

3.5.2 Theoretical Stress Analysis – Series II Tests

Stresses theoretically experienced by the test girders are computed using classical engineering theories along with Basler's tension field action equations. Using the test setup dimensions given in the previous sections and reproduced in Figure 3-15, the applied shear and moment can be calculated as a function of applied load for any point along the test girder's length. From the shear force diagram, note that the applied shear at every location in the test girder is always equal in magnitude to the applied load. For the location of the test panel:

$$V = -P \qquad \textbf{Equation 3-1}$$

The bending moment diagram shows that the applied moment is always negative and peaks at the central bearing stiffener with a value of –PL. In order to determine the bending moment at a distance x from the central bearing stiffener, the following equation may be used:

$$M(x) = -P \cdot (L - x) \qquad \textbf{Equation 3-2}$$

Equation 3-1 and Equation 3-2, along with classical beam theory, provide the relationships necessary to express the theoretical elastic stresses as functions of applied load.

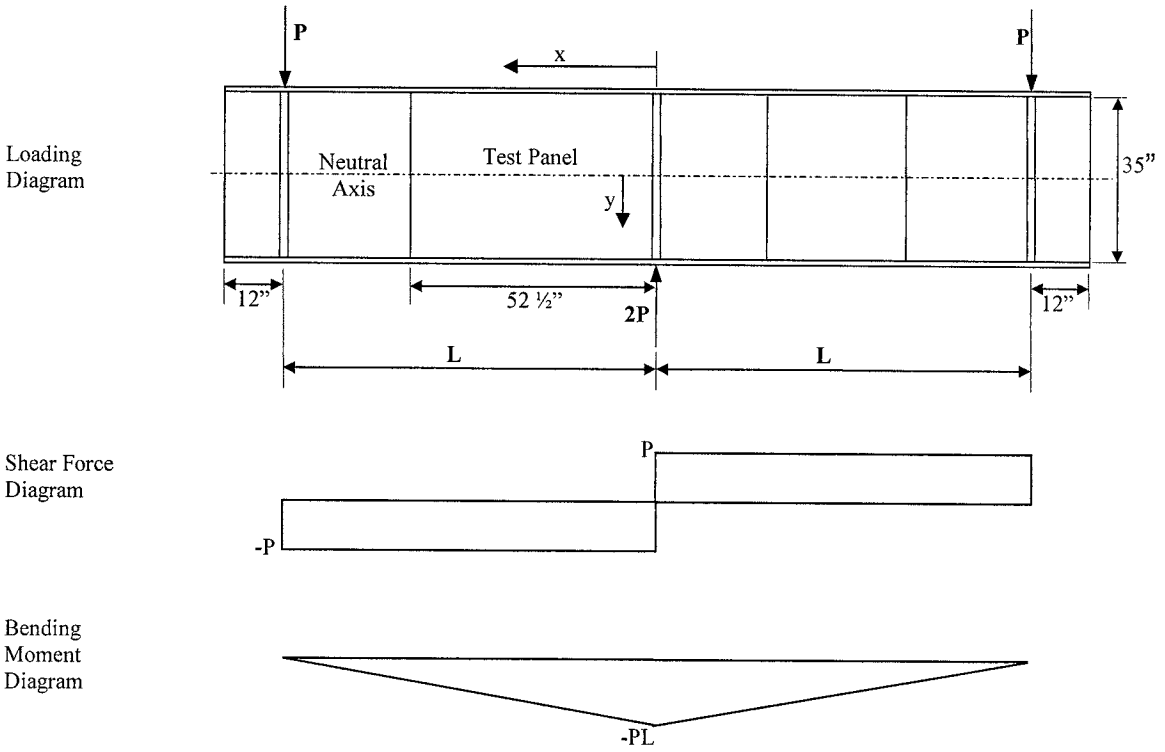

Figure 3-15. Series II Testing Configuration

3.5.2.1 Elastic Stresses

According to Basler's tension field action theory, the girder is assumed to resist loading in a beam-type manner prior to web buckling. Classical beam theory is used to express the theoretical stresses present in the test girder as a function of applied load, P. The flexure formula provides the normal stresses, σ_x, introduced to the girder due to bending. The linear flexural stress distribution is shown in Figure 3-16. The distance from the neutral axis, y, is defined to be positive when directed downward from the neutral axis. This results in a sign convention in which tensile stresses are positive and compressive stresses are negative.

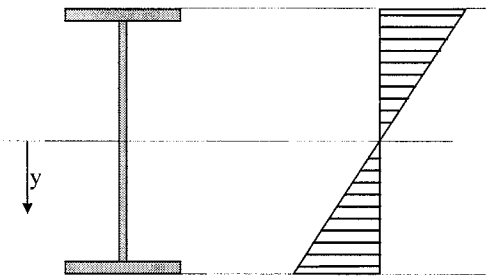

Figure 3-16. Theoretical Flexural Stress Distribution

The flexure formula is:

$$\sigma_x = \frac{M \cdot y}{I} \qquad \textbf{Equation 3-3}$$

Where:

I = strong axis moment of inertia

Substituting Equation 3-2 into Equation 3-3:

$$\sigma_x = \frac{-P \cdot y \cdot (L - x)}{I} \qquad \textbf{Equation 3-4}$$

Equation 3-4 is used to express the flexural stress for any given location on the test girder as a function of applied load. Similarly, the shear stress formula can be used to express the theoretical shear stress, τ_{xy}, at any location in the test girder as a function of applied load. The theoretical shear stress distribution is shown in Figure 3-17.

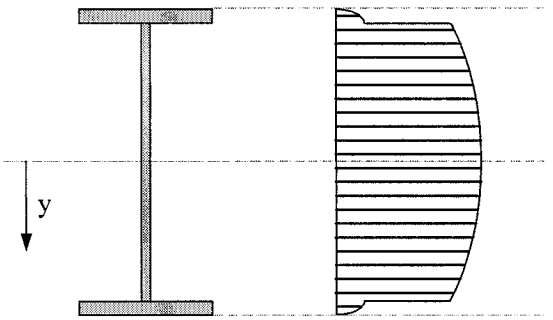

Figure 3-17. Theoretical Shear Stress Distribution

The transverse shear stress formula is:

$$\tau_{xy} = \frac{V \cdot Q}{I \cdot t}$$ **Equation 3-5**

Where:

Q = first moment of area about the neutral axis

$$= \frac{t_w}{2}\left(\frac{D^2}{4} - y^2\right) + \frac{b_f \cdot t_f}{2}\left(D + t_f\right) \qquad \text{for } |y| \le \frac{D}{2}$$

t = thickness of girder cross section at distance y from neutral axis

Substituting Equation 3-1 into Equation 3-5:

$$\tau_{xy} = \frac{-P \cdot Q}{I \cdot t}$$ **Equation 3-6**

Equation 3-6 gives the theoretical shear stress as a function of applied load for any given location on the test girder. Note that, according to the shear force diagram

(Figure 3-15), this equation is valid only for the half of the girder containing the test panel; the sign is reversed for the other half of the girder.

From the theoretical normal and shear stresses calculated above, the principal stresses can be computed. Using the equation of Mohr's circle, and taking into account that the vertical normal stress, σ_y, is theoretically zero, the principal stresses are:

$$\sigma_1 = \frac{\sigma_x}{2} + \sqrt{\left(\frac{\sigma_x}{2}\right)^2 + \tau_{xy}^2}$$ **Equation 3-7**

$$\sigma_2 = \frac{\sigma_x}{2} - \sqrt{\left(\frac{\sigma_x}{2}\right)^2 + \tau_{xy}^2}$$ **Equation 3-8**

Where:

σ_1 = major principal stress

σ_2 = minor principal stress

The orientation of the major principal stress from the x-axis is given as:

$$\theta_{\sigma 1} = -\frac{1}{2} \cdot \tan^{-1}\left(\frac{2\tau_{xy}}{\sigma_x}\right) \qquad \text{if } \sigma_x \text{ is a tensile stress}$$ **Equation 3-9**

$$\theta_{\sigma 1} = 90° - \frac{1}{2} \cdot \tan^{-1}\left(\frac{2\tau_{xy}}{\sigma_x}\right) \qquad \text{if } \sigma_x \text{ is a compressive stress}$$ **Equation 3-10**

$\theta_{\sigma 1}$ is defined as the angle from the x-axis (longitudinal axis of girder) to the plane of the major principal stress. Positive angles are counter-clockwise, negative angles are clockwise.

The complete theoretical state of stress at any given level of loading prior to web buckling can be defined either with x-y coordinate stresses or with principal stresses and

inclinations. The relationship of the x-y plane to the principal plane is best visualized by plotting them together on Mohr's circle, as in Figure 3-18.

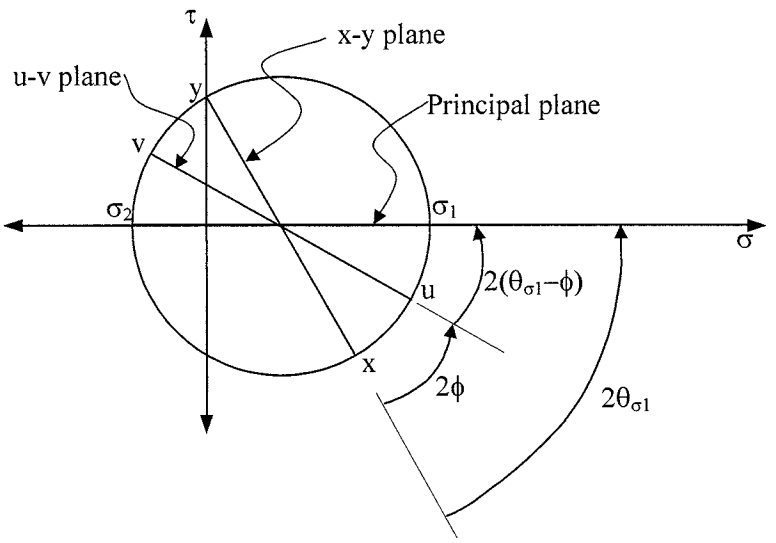

Figure 3-18. Relationship of Stress Planes

The theoretical stresses discussed in this section are limited to the elastic, or pre-buckling, load levels. The upper limit of elastic behavior is called the shear buckling load, V_{cr} (see derivation in Section 2.3.3). Basler's shear buckling load is calculated as:

Equation 3-11

$$V_{cr} = V_p \cdot \frac{\tau_{cr}}{\tau_y}$$

Recall from Basler's derivation that the shear buckling load is the level of applied shear that produces the shear buckling stress, τ_{cr}, which is sufficient to buckle the slender

web due to diagonal compression. As stated in Section 2.3.3, the state of stress of an element at the neutral axis at the shear buckling load is pure shear and:

$$\tau_{xy} = \tau_{cr} = k \cdot \frac{\pi^2 \cdot E}{12 \cdot (1 - \nu^2)} \cdot \left(\frac{t_w}{D}\right)^2$$ **Equation 3-12**

The state of stress described above is shown in Figure 3-19(a). This state of stress can be equivalently expressed in u-v coordinates, shown in Figure 3-19(b) and calculated as:

$$\sigma_u = \tau_{cr} \cdot \sin(2\phi)$$ **Equation 3-13**

$$\sigma_v = -\tau_{cr} \cdot \sin(2\phi)$$ **Equation 3-14**

$$\tau_{uv} = -\tau_{cr} \cdot \cos(2\phi)$$ **Equation 3-15**

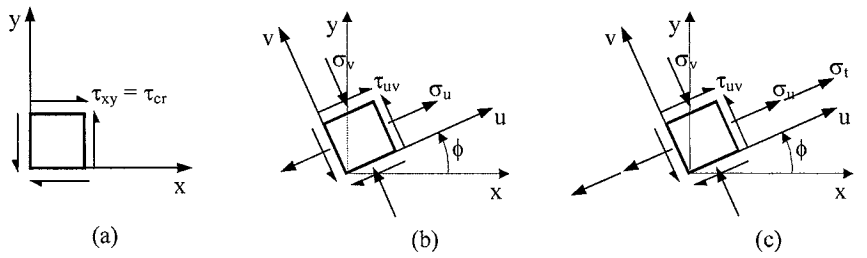

Figure 3-19. Neutral Axis States of Stress

In order to convert stresses on the u-v plane to the principal plane, the following equations may be used:

$$\sigma_1 = \frac{\sigma_u + \sigma_v}{2} + \sqrt{\left(\frac{\sigma_u - \sigma_v}{2}\right)^2 + \tau_{uv}^2}$$ **Equation 3-16**

$$\sigma_2 = \frac{\sigma_u + \sigma_v}{2} - \sqrt{\left(\frac{\sigma_u - \sigma_v}{2}\right)^2 + \tau_{uv}^2}$$ **Equation 3-17**

The angle from the u-v plane to the principal plane is expressed as $(\theta_{\sigma 1}-\phi)$, where $\theta_{\sigma 1}$ is the angle from the x-y plane to the principal plane and ϕ is the angle from the x-y plane to the u-v plane, as shown in Figure 3-18.

$$(\theta_{\sigma 1} - \phi) = -\frac{1}{2}\tan^{-1}\left(\frac{2\tau_{uv}}{\sigma_u - \sigma_v}\right) \qquad \text{if } \sigma_u \geq \sigma_v$$ **Equation 3-18**

$$(\theta_{\sigma 1} - \phi) = 45° - \frac{1}{2}\tan^{-1}\left(\frac{2\tau_{uv}}{\sigma_u - \sigma_v}\right) \qquad \text{if } \sigma_u < \sigma_v$$ **Equation 3-19**

3.5.2.2 Postbuckling Stresses

Equation 3-12 gives the value of the maximum shear stress that an element at the neutral axis will experience prior to web buckling. Following web buckling, the state of stress caused by the shear buckling stress on the v-axis is assumed to remain constant while tension field action stresses begin to form in the web in the direction of the u-axis, which is rotated an angle ϕ from the x-axis. The maximum magnitude of tension field action stress derived by Basler and stated in Section 2.3.3 as Equation 2-35 is:

$$\sigma_t = F_y \cdot \left(\sqrt{1 + \left(\frac{\tau_{cr}}{F_y}\right)^2 \cdot \left[\left(\frac{3}{2}\cdot\sin(2\phi)\right)^2 - 3\right]} - \frac{3}{2}\cdot\frac{\tau_{cr}}{F_y}\cdot\sin(2\phi) \right)$$ **Equation 3-20**

The tension field stress, σ_t, is the stress required to fulfill the von-Mises yield criterion when added to the shear buckling stress. When expressed in u-v coordinates, σ_t can be directly added to the normal stress σ_u, resulting in the following state of stress, shown in Figure 3-19(c):

$$\sigma_u = \tau_{cr} \cdot \sin(2\phi) + \sigma_t$$ **Equation 3-21**

$$\sigma_v = -\tau_{cr} \cdot \sin(2\phi)$$ **Equation 3-22**

$$\tau_{uv} = -\tau_{cr} \cdot \cos(2\phi)$$ **Equation 3-23**

Note that Equation 3-20 gives only the maximum tension field stress. Basler's tension field action theory does not specify how the incremental tension field stresses develop in the web (i.e. linearly with applied load, etc.). Hence, the theoretical state of stress is not explicitly defined for every given load level in the postbuckling region; only the limiting states of stress at web buckling and failure are theoretically defined.

The state of stress at failure can be converted to the principal plane as before using Equation 3-16 through Equation 3-19. From Basler's derivation, the applied shear required to fail the girder in shear is:

$$V_u = V_p \cdot \left[\frac{\tau_{cr}}{\tau_y} + \frac{\sqrt{3}}{2} \cdot \frac{\sigma_t}{F_y} \cdot \frac{1}{\sqrt{1 + \left(d_0 / D \right)^2}} \right]$$ **Equation 3-24**

3.5.2.3 Example Calculation of Theoretical Stresses

In order to compare with experimental stresses, the theoretical stresses will be calculated using the dimensions and properties of test Beam 6a. The girder is hybrid with a total span length of 13.5 feet. The target values for relative moment and shear are both 1.0, which means that the girder is expected to reach its full shear and moment capacities at approximately the same applied load. The given yield strengths are from tension tests performed on samples of the steel plates that make up the plate girders (Schreiner 2001). The properties are as follows:

Shear Span, L = 81"

Flange width, b_f = 8 ¾"

Flange thickness, t_f = ½"

Flange yield strength, F_{yf} = 91.0 ksi

Web depth, D = 35"

Web thickness, t_w = ¼"

Web yield strength, F_{yw} = 60.8 ksi

Modulus of Elasticity, E = 29,000 ksi (assumed)

Poisson's Ratio, ν = 0.3 (assumed)

To calculate the theoretical state of stress in the web, an applied shear of P = 60 kips will be assumed. Note that this load level is less than the critical buckling load, so tension field action stresses are theoretically absent. The stresses will be calculated at the location of Gauge 1 (see Figure 3-13). Gauge 1 has the following coordinates, defined in Figure 3-15:

x = 39.25 in (from center support)

y = -8.6875 in (from neutral axis, up negative)

First, the applied shear and bending moment is calculated. According to Equation 3-1, $V = -P = -60\,\text{kips}$.

The applied moment can be calculated with Equation 3-2, which gives:

$$M(x) = -P \cdot (L - x) = -60\,\text{kips} \cdot (81\,\text{in} - 39.25\,\text{in}) \cdot \frac{1\,\text{ft}}{12\,\text{in}} = -209\,\text{kip} \cdot \text{ft}$$

In order to calculate stresses, the moment of inertia of the cross section must be known. For this symmetric girder, the strong axis moment of inertia is:

$$I = \frac{1}{12} \cdot \left[b_f (D + 2t_f)^3 - (b_f - t_w) D^3 \right] = \frac{1}{12} \cdot \left[(8.75)(35 + 2 \cdot 0.5)^3 - (8.75 - 0.25)(35)^3 \right] = 3650\,\text{in}^4$$

From Equation 3-3, the flexural stress is:

$$\sigma_x = \frac{M \cdot y}{I} = \frac{(-209\,\text{kip} \cdot \text{ft}) \cdot (-8.6875\,\text{in})}{3650\,\text{in}^4} \cdot \frac{12\,\text{in}}{1\,\text{ft}} = 5.97\,\text{ksi}$$

In order to calculate the shear stress, the first moment of area about the neutral axis, Q, must be determined as follows:

$$Q = \frac{t_w}{2}\left(\frac{D^2}{4} - y^2 \right) + \frac{b_f \cdot t_f}{2}(D + t_f) = \frac{0.25}{2}\left(\frac{35^2}{4} - (-8.6875)^2 \right) + \frac{8.75(0.5)}{2}(35 + 0.25) = 106.5\,\text{in}^3$$

The shear stress is then calculated from Equation 3-5 as:

$$\tau_{xy} = \frac{V \cdot Q}{I \cdot t} = \frac{-60\,\text{kips} \cdot (106.5\,\text{in}^3)}{3650\,\text{in}^4 \cdot (0.25\,\text{in})} = -7.0\,\text{ksi}$$

Since the vertical normal stress, σ_y, is theoretically zero, the complete state of stress of an element located at Gauge 1 under an applied load of 60 kips is theoretically known (see Figure 3-20). It may be desirable to express this state of stress on the principal plane. The major principal stress can be found using Equation 3-7 as follows:

$$\sigma_1 = \frac{\sigma_x}{2} + \sqrt{\left(\frac{\sigma_x}{2}\right)^2 + \tau_{xy}^2} = \frac{5.97\,\text{ksi}}{2} + \sqrt{\left(\frac{5.97\,\text{ksi}}{2}\right)^2 + (-7.0\,\text{ksi})^2} = 10.6\,\text{ksi}$$

Using Equation 3-8, the minor principal stress is found to be:

$$\sigma_2 = \frac{\sigma_x}{2} - \sqrt{\left(\frac{\sigma_x}{2}\right)^2 + \tau_{xy}^2} = \frac{5.97\,\text{ksi}}{2} - \sqrt{\left(\frac{5.97\,\text{ksi}}{2}\right)^2 + (-7.0\,\text{ksi})^2} = -4.62\,\text{ksi}$$

Since σ_x is positive, it is a tensile stress and Equation 3-9 can be used to calculate the orientation of the principal plane.

$$\theta_{\sigma 1} = -\frac{1}{2} \cdot \tan^{-1}\left(\frac{2\tau_{xy}}{\sigma_x}\right) = -\frac{1}{2} \cdot \tan^{-1}\left(\frac{2 \cdot (-7.0\,\text{ksi})}{5.97\,\text{ksi}}\right) = 33.5°$$

Theoretical stresses can also be calculated for locations on the flange. To compare with experimental data, the flexural stress at the location of flange Gauge 1 will be calculated. This gauge is located at:

x = 39.25"

y = -17.5"

Since flange Gauge 1 is located the same distance from the central bearing stiffener as web Gauge 1, the applied moment at flange Gauge 1 is the same as that of web Gauge 1:

$M(x) = -209\,\text{kip} \cdot \text{ft}$

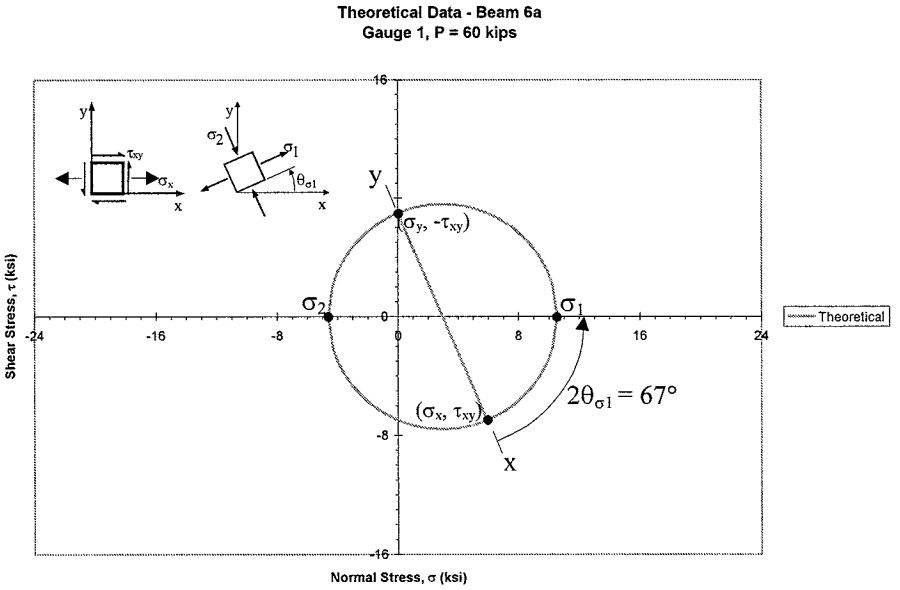

Figure 3-20. Mohr's Circle: Theoretical State of Stress at Gauge 1 (x-y Plane Shown)

The flexural stress is calculated in the same manner as for the web gauge:

$$\sigma_x = \frac{M \cdot y}{I} = \frac{(-209\,\text{kip}\cdot\text{ft})\cdot(-17.5\,\text{in})}{3650\,\text{in}^4}\cdot\frac{12\,\text{in}}{1\,\text{ft}} = 12.0\,\text{ksi}$$

The stresses calculated so far are valid for load levels less than the critical buckling load. The critical buckling load is defined as the shear load that causes the shear stress at the neutral axis to reach the shear buckling stress, τ_{cr}, defined in Equation 3-12.

For $d_0/D = \frac{52.5\,\text{in}}{35\,\text{in}} = 1.5 > 1.0$, the plate buckling coefficient is:

$$k = 5.34 + \frac{4.00}{\left(d_0/D\right)^2} = 5.34 + \frac{4.00}{(1.5)^2} = 7.12$$

The shear buckling stress can then be determined:

$$\tau_{cr} = k \cdot \frac{\pi^2 \cdot E}{12 \cdot (1-\nu^2)} \cdot \left(\frac{t_w}{D}\right)^2 = 7.12 \cdot \frac{\pi^2 (29{,}000\,\text{ksi})}{12 \cdot (1-0.3^2)} \cdot \left(\frac{0.25\,\text{in}}{35\,\text{in}}\right)^2 = 9.52\,\text{ksi}$$

The plastic shear force, V_p, is defined in Section 2.3.3 as:

$$V_p = \tau_y \cdot D \cdot t_w = \frac{60.8\,\text{ksi}}{\sqrt{3}} \cdot (35\,\text{in})(0.25\,\text{in}) = 307\,\text{kips}$$

The critical buckling load can now be calculated using Equation 3-11:

$$V_{cr} = V_p \cdot \frac{\tau_{cr}}{\tau_y} = \tau_y \cdot D \cdot t_w \cdot \frac{\tau_{cr}}{\tau_y} = D \cdot t_w \cdot \tau_{cr} = (35\,\text{in})(0.25\,\text{in})(9.52\,\text{ksi}) = 83.3\,\text{kips}$$

Theoretically, the state of stress at the neutral axis is pure shear. The magnitude of the shear stress is equal to the critical buckling stress when the critical buckling load is applied. It is useful to express this state of stress in u-v coordinates, which are rotated an angle ϕ from the x-y axes. The angle ϕ can be determined from Equation 2-17 as:

$$\phi = \frac{1}{2}\tan^{-1}\left(\frac{D}{d_0}\right) = \frac{1}{2}\tan^{-1}\left(\frac{35\,\text{in}}{52.5\,\text{in}}\right) = 16.8°$$

The normal stress along the u-axis is then calculated from Equation 3-13:

$$\sigma_u = \tau_{cr} \cdot \sin(2\phi) = (9.52\,\text{ksi}) \cdot \sin(2(16.8°)) = 5.27\,\text{ksi}$$

Equation 3-14 is used to calculate the normal stress along the v-axis:

$$\sigma_v = -\tau_{cr} \cdot \sin(2\phi) = -(9.52\,\text{ksi}) \cdot \sin(2(16.8°)) = -5.27\,\text{ksi}$$

Shear stresses in the u-v plane are calculated with Equation 3-15:

$$\tau_{uv} = -\tau_{cr} \cdot \cos(2\phi) = -(9.52\,\text{ksi}) \cdot \cos(2(16.8°)) = -7.93\,\text{ksi}$$

The complete state of stress at web buckling is shown in Mohr's circle in Figure 3-21. Equation 3-16 and Equation 3-17 are used to find the principal stresses from the state of stress given above:

$$\sigma_1 = \frac{\sigma_u + \sigma_v}{2} + \sqrt{\left(\frac{\sigma_u - \sigma_v}{2}\right)^2 + \tau_{uv}^2} = \frac{5.27 + (-5.27)}{2} + \sqrt{\left(\frac{5.27 - (-5.27)}{2}\right)^2 + (-7.93)^2} = 9.52\,\text{ksi}$$

$$\sigma_2 = \frac{\sigma_u + \sigma_v}{2} - \sqrt{\left(\frac{\sigma_u - \sigma_v}{2}\right)^2 + \tau_{uv}^2} = \frac{5.27 + (-5.27)}{2} - \sqrt{\left(\frac{5.27 - (-5.27)}{2}\right)^2 + (-7.93)^2} = -9.52\,\text{ksi}$$

Since $\sigma_u > \sigma_v$, Equation 3-18 is used to find the angle from the u-v plane to the principal plane:

$$(\theta_{\sigma 1} - \phi) = -\frac{1}{2}\tan^{-1}\left(\frac{2\tau_{uv}}{\sigma_u - \sigma_v}\right) = -\frac{1}{2}\tan^{-1}\left(\frac{2(-7.93)}{5.27 - (-5.27)}\right) = 28.2°$$

In order to determine the state of stress at failure, the maximum tension field stress, σ_t, is added to the buckling state of stress along the u-axis. The maximum tension field stress is calculated from Equation 3-20 as:

$$\sigma_t = F_y \cdot \left(\sqrt{1 + \left(\frac{\tau_{cr}}{F_y}\right)^2 \cdot \left[\left(\frac{3}{2} \cdot \sin(2\phi)\right)^2 - 3\right]} - \frac{3}{2} \cdot \frac{\tau_{cr}}{F_y} \cdot \sin(2\phi)\right)$$

$$= 60.8\,\text{ksi} \cdot \left(\sqrt{1 + \left(\frac{9.52\,\text{ksi}}{60.8\,\text{ksi}}\right)^2 \cdot \left[\left(\frac{3}{2} \cdot \sin(2 \cdot 16.8°)\right)^2 - 3\right]} - \frac{3}{2}\left(\frac{9.52\,\text{ksi}}{60.8\,\text{ksi}}\right) \cdot \sin(2(16.8°))\right) = 51.2\,\text{ksi}$$

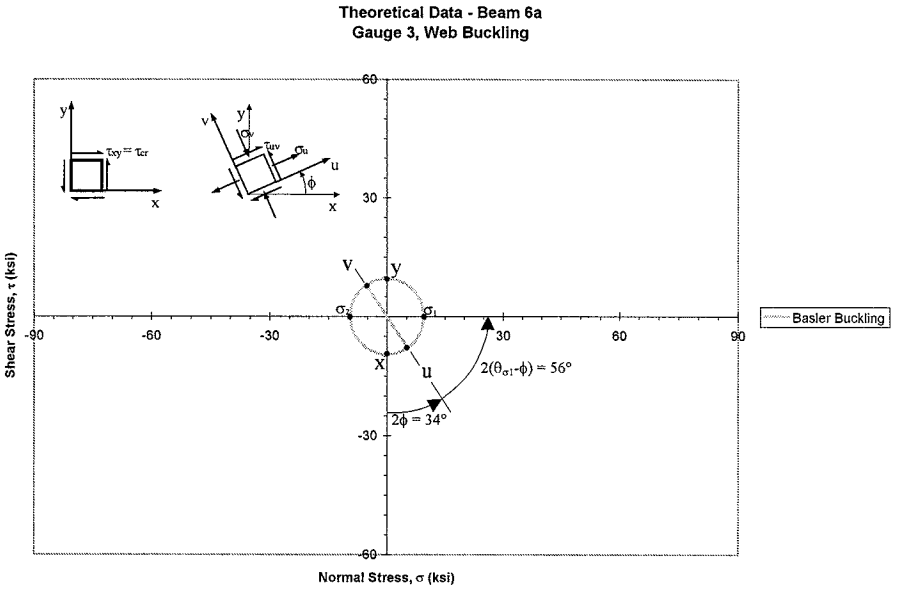

Figure 3-21. Mohr's Circle: State of Stress at Web Buckling (u-v Plane Shown)

The shear load that will cause failure of the girder is calculated from Equation 3-24:

$$V_u = V_p \cdot \left[\frac{\tau_{cr}}{\tau_y} + \frac{\sqrt{3}}{2} \cdot \frac{\sigma_t}{F_y} \cdot \frac{1}{\sqrt{1+\left(d_0/D\right)^2}} \right]$$

$$= (307\ \text{kips}) \cdot \left[\left(\frac{9.52\ \text{ksi}}{35.1\ \text{ksi}}\right) + \frac{\sqrt{3}}{2} \cdot \left(\frac{51.2\ \text{ksi}}{60.8\ \text{ksi}}\right) \cdot \frac{1}{\sqrt{1+\left(52.5\ \text{in}/35\ \text{in}\right)^2}} \right] = 207\ \text{kips}$$

The tension field stress is added to the u-axis buckling stress to determine the u-axis stress at failure (Equation 3-21):

$$\sigma_u = \tau_{cr} \cdot \sin(2\phi) + \sigma_t = 5.27\ \text{ksi} + 51.2\ \text{ksi} = 56.5\ \text{ksi}$$

The v-axis stress and shear stress theoretically remain constant from buckling to failure:

$$\sigma_v = -\tau_{cr} \cdot \sin(2\phi) = -5.27 \text{ ksi}$$

$$\tau_{uv} = -\tau_{cr} \cdot \cos(2\phi) = -7.93 \text{ ksi}$$

The Mohr's circle for the state of stress at theoretical failure is shown in Figure 3-22, with theoretical buckling shown for reference.

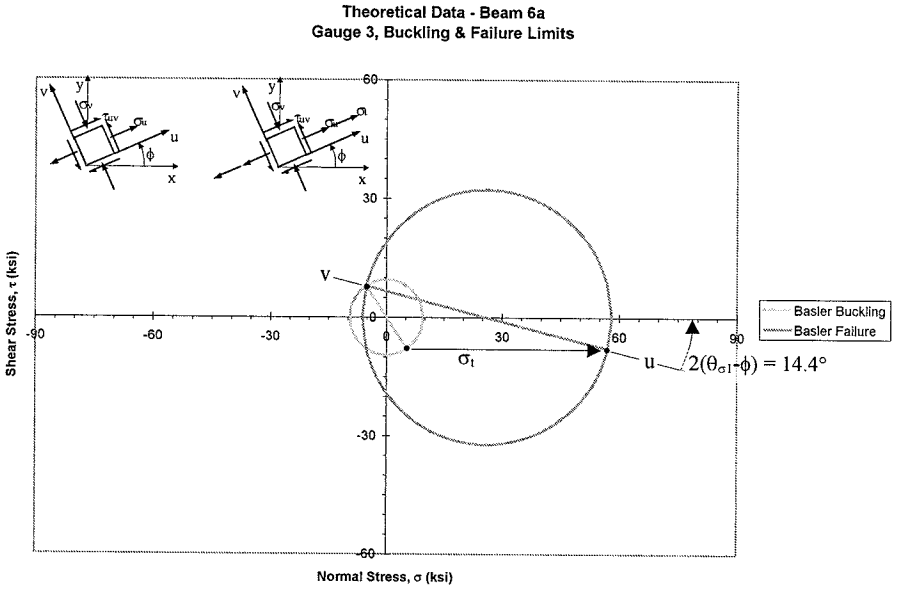

Figure 3-22. States of Stress at Buckling and Failure (u-v Planes Shown)

The principal stresses at failure are computed using Equation 3-16 and Equation 3-17:

$$\sigma_1 = \frac{\sigma_u + \sigma_v}{2} + \sqrt{\left(\frac{\sigma_u - \sigma_v}{2}\right)^2 + \tau_{uv}^2} = \frac{56.5 + (-5.27)}{2} + \sqrt{\left(\frac{56.5 - (-5.27)}{2}\right)^2 + (-7.93)^2} = 57.4 \text{ ksi}$$

$$\sigma_2 = \frac{\sigma_u + \sigma_v}{2} - \sqrt{\left(\frac{\sigma_u - \sigma_v}{2}\right)^2 + \tau_{uv}^2} = \frac{56.5 + (-5.27)}{2} - \sqrt{\left(\frac{56.5 - (-5.27)}{2}\right)^2 + (-7.93)^2} = -6.27 \text{ ksi}$$

Since $\sigma_u > \sigma_v$, Equation 3-18 is used to calculate the angle of inclination of the principal plane from the u-v plane:

$$(\theta_{\sigma 1} - \phi) = -\frac{1}{2}\tan^{-1}\left(\frac{2\tau_{uv}}{\sigma_u - \sigma_v}\right) = -\frac{1}{2}\tan^{-1}\left(\frac{2(-7.93)}{56.5 - (-5.27)}\right) = 7.2°$$

3.5.3 Experimental Stress Analysis

The objective of Series II testing is to show that tension field action stresses are present in hybrid plate girders subject to concurrent bending and shear, and that these stresses can anchor reasonably well to the stiffeners and flanges through web material that may be yielded due to flexural stresses. Interpretation of experimental data is a critical step in this process, so the method of data analysis will be given in detail. Example calculations will be given to clarify the process and to compare with the theoretical stresses calculated in Section 3.5.2.3. Comparison of experimental and theoretical stresses for Series II tests will be presented in Chapter 4.

3.5.3.1 Rosette Strain Gauge Data

As discussed in Section 3.3.3, rectangular rosette strain gauges were bonded to the web of the test panel in order to record strain information during testing. Each rosette provides three sets of strain data, each in a different direction. This data is used to infer a state of strain in the plane of the gauge. In order to remove erroneous data caused by out-of-plane effects, each strain gauge location was instrumented with two strain gauges, one on either side of the web that were averaged to take out out-of-plane stress fluctuations.

Therefore, six sets of strain data in three directions are used to determine the experimental state of strain at each gauge location on the web of the test panel.

Each strain gauge was given a designation in order to distinctly identify the data collected (Figures 3-13 and 3-14). The direction of strain recorded by each individual gauge included in the rectangular rosette configuration is apparent from its designation. The horizontal direction is designated as "2", whereas "1" is directed 45° clockwise from horizontal. Direction "3" is 45° counter-clockwise from horizontal, as shown in Figure 3-23.

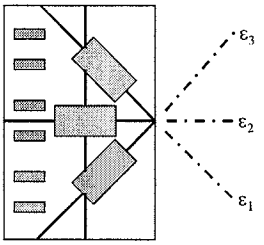

Directional strain gauges can be adversely affected by strains that act in directions other than the direction of the gauge. This effect is called transverse sensitivity. The errors due to the transverse sensitivity of rectangular rosette strain gauges in Series I testing were found to be less than 1% (Rush 2001). Therefore, transverse sensitivity corrections will not be included in Series II data analysis.

Figure 3-23. Rosette Strain Gauge Directions

Out-of-plane effects such as web buckling are taken into consideration by mirroring the strain gauge layout on either side of the web. It is assumed that if a gauge reports compressive strains due to out-of-plane bending of the web, then the gauge on the other side of the web will report tensile strains of the same magnitude. The data from

these gauges can then be averaged together in order to cancel out any strains caused by out-of-plane bending of the web.

Using the averaged data, a state of strain is inferred using Mohr's circle equations. First, the principal strains are determined using the following equations:

$$\varepsilon_P = \frac{\varepsilon_1 + \varepsilon_3}{2} + \frac{1}{\sqrt{2}}\sqrt{(\varepsilon_1 - \varepsilon_2)^2 + (\varepsilon_2 - \varepsilon_3)^2} \qquad \textbf{Equation 3-25}$$

$$\varepsilon_Q = \frac{\varepsilon_1 + \varepsilon_3}{2} - \frac{1}{\sqrt{2}}\sqrt{(\varepsilon_1 - \varepsilon_2)^2 + (\varepsilon_2 - \varepsilon_3)^2} \qquad \textbf{Equation 3-26}$$

Where:

ε_P = major principal strain

ε_Q = minor principal strain

ε_1 = measured strain in "1" direction

ε_2 = measured strain in "2" direction

ε_3 = measured strain in "3" direction

Principal stresses can be computed from the principal strains using Hooke's Law for biaxial stress. Hooke's Law assumes that the material in question is homogeneous, isotropic, and linear elastic. These assumptions are reasonably satisfied for load levels up until web buckling, but postbuckling behavior is clearly non-linear. However, the assumption of linear behavior will be extended into the postbuckling regime for analysis. The biaxial stress Hooke's Law equations are:

$$\sigma_P = \frac{E}{1-\nu^2}(\varepsilon_P + \nu \cdot \varepsilon_Q) \qquad \textbf{Equation 3-27}$$

$$\sigma_Q = \frac{E}{1-\nu^2}\left(\varepsilon_Q + \nu \cdot \varepsilon_P\right)$$ **Equation 3-28**

Where:

σ_P = major principal stress

σ_Q = minor principal stress

The experimental orientation of the principal plane, θ_{xp}, is then determined by the following equations:

$$\theta_{xp} = 135° - \frac{1}{2}\tan^{-1}\left(\frac{\varepsilon_1 - 2\varepsilon_2 + \varepsilon_3}{\varepsilon_1 - \varepsilon_3}\right) \quad \text{if } \varepsilon_1 \geq \varepsilon_3$$ **Equation 3-29**

$$\theta_{xp} = 45° - \frac{1}{2}\tan^{-1}\left(\frac{\varepsilon_1 - 2\varepsilon_2 + \varepsilon_3}{\varepsilon_1 - \varepsilon_3}\right) \quad \text{if } \varepsilon_1 < \varepsilon_3$$ **Equation 3-30**

Here, θ_{xp} is defined as the angle from the x-axis (horizontal) to the major principal plane. Counter-clockwise rotation is considered positive, while clockwise angles are negative. The experimental state of stress is now completely defined and can be expressed on any plane. In order to describe the state of stress on the original x-y coordinates, the following equations may be used:

$$\sigma_x = \frac{\sigma_P + \sigma_Q}{2} + \frac{\sigma_P - \sigma_Q}{2}\cos\left(2\theta_{xp}\right)$$ **Equation 3-31**

$$\sigma_y = \frac{\sigma_P + \sigma_Q}{2} - \frac{\sigma_P - \sigma_Q}{2}\cos\left(2\theta_{xp}\right)$$ **Equation 3-32**

$$\tau_{xy} = -\frac{\sigma_P - \sigma_Q}{2}\sin(2\theta_{xp})$$ **Equation 3-33**

In order to express the experimental state of stress in u-v coordinates (rotated counter-clockwise by any given angle ϕ from the x-y coordinate system), the following equations may be used:

$$\sigma_u = \frac{\sigma_P + \sigma_Q}{2} + \frac{\sigma_P - \sigma_Q}{2}\cos(2\theta_{xp} - 2\phi)$$ **Equation 3-34**

$$\sigma_v = \frac{\sigma_P + \sigma_Q}{2} - \frac{\sigma_P - \sigma_Q}{2}\cos(2\theta_{xp} - 2\phi)$$ **Equation 3-35**

$$\tau_{uv} = -\frac{\sigma_P - \sigma_Q}{2}\sin(2\theta_{xp} - 2\phi)$$ **Equation 3-36**

3.5.3.2 Linear Strain Gauge Data

Linear strain gauges are used to collect experimental strain information from the test girder's flanges and stiffeners. The linear gauges collect the strain information in the same manner as the rosette gauges, but only in the direction of the gauge axis. For this reason, only the stress in that direction can be computed as opposed to the complete state of stress calculated for the rosette gauges.

As shown in Figure 3-13, linear strain gauges are bonded to the inside surfaces of the flanges of the test panel. Also, both sides of the bearing stiffeners and intermediate transverse stiffeners bordering the test panel are instrumented with linear gauges. The gauges are oriented such that the flange gauges record strains along the longitudinal axis of the girder and the stiffener gauges record axial strains in the transverse stiffeners. The

objective of gauging the stiffeners and flanges is to detect a change in stresses caused by anchorage of a tension field (see Figure 3-24).

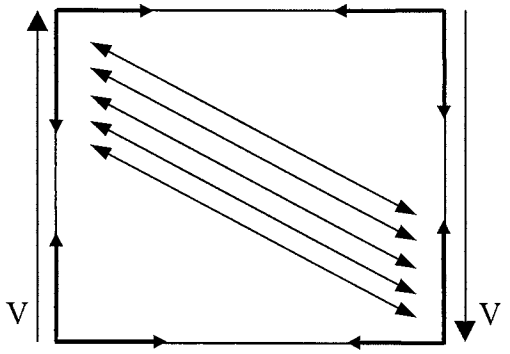

Figure 3-24. Anchorage of TFA Stresses

Since linear strain gauges report strains in only one direction, Hooke's Law for uniaxial stress can be used to convert the strain information to stresses. Hooke's Law again assumes the material to be homogeneous, isotropic, and linear elastic. These assumptions are reasonably satisfied for the linear gauges, as no yielding is expected at these locations prior to failure. Hooke's Law for uniaxial stress is:

$$\sigma = E \cdot \varepsilon \qquad \textbf{Equation 3-37}$$

3.5.3.3 String Pot Data

Similar to strain gauges, the data from the string pots is recorded as voltages. The string pots were calibrated at the testing facility prior to Series I testing, and calibration factors for each string pot were obtained. These calibration factors convert the voltages directly into length measurements. The objective of instrumenting the test panel with

string pots is to track out-of-plane web deflections across the tension field as well as to attempt to determine the load level that causes web buckling in the test girders. The locations of the string pots are shown on the instrumentation layout diagram, Figure 3-14.

3.5.3.4 Example Experimental Stress Calculations

The following example calculations detail how the test data is reduced to engineering terms. The following example is based on data taken from test Beam 6a at a load level of P = 60.1 kips. The equations used in this example are typical of all tests and load levels. Below, recorded strain data from both rosette gauges at gauge location 1 (see Figure 3-13) is given in micro-strains:

E1-1: 1.71 με	W1-1: -374 με
E1-2: 303 με	W1-2: 108 με
E1-3: 436 με	W1-3: 248 με

The data from opposite sides of the web panel is averaged to remove out-of-plane effects:

$$A1-1 = \frac{(E1-1)+(W1-1)}{2} = \frac{(1.71)+(-374)}{2} = -186\,\mu\varepsilon = \varepsilon_1$$

$$A1-2 = \frac{(E1-2)+(W1-2)}{2} = \frac{(303)+(108)}{2} = 206\,\mu\varepsilon = \varepsilon_2$$

$$A1-3 = \frac{(E1-3)+(W1-3)}{2} = \frac{(436)+(248)}{2} = 342\,\mu\varepsilon = \varepsilon_3$$

The major principal strain is determined using Equation 3-25:

$$\varepsilon_P = \frac{\varepsilon_1 + \varepsilon_3}{2} + \frac{1}{\sqrt{2}}\sqrt{(\varepsilon_1 - \varepsilon_2)^2 + (\varepsilon_2 - \varepsilon_3)^2}$$

$$= \frac{-186 + 342}{2} + \frac{1}{\sqrt{2}}\sqrt{(-186 - 206)^2 + (206 - 342)^2} = 371\,\mu\varepsilon$$

Similarly, the minor principal strain is determined with Equation 3-26:

$$\varepsilon_Q = \frac{\varepsilon_1 + \varepsilon_3}{2} - \frac{1}{\sqrt{2}}\sqrt{(\varepsilon_1 - \varepsilon_2)^2 + (\varepsilon_2 - \varepsilon_3)^2}$$

$$= \frac{-186 + 342}{2} - \frac{1}{\sqrt{2}}\sqrt{(-186 - 206)^2 + (206 - 342)^2} = -215\,\mu\varepsilon$$

From the principal strains, the principal stresses are determined using Hooke's Law for biaxial stress. As before, Young's Modulus and Poisson's Ratio are assumed to be 29,000 ksi and 0.3, respectively. Using Equation 3-27 and Equation 3-28:

$$\sigma_P = \frac{E}{1-\nu^2}(\varepsilon_P + \nu \cdot \varepsilon_Q) = \frac{29{,}000\text{ ksi}}{1-(0.3)^2}\left(0.000371\,{}^{\text{in}}/_{\text{in}} + (0.3)\cdot\left(-0.000215\,{}^{\text{in}}/_{\text{in}}\right)\right) = 9.77\text{ ksi}$$

$$\sigma_Q = \frac{E}{1-\nu^2}(\varepsilon_Q + \nu \cdot \varepsilon_P) = \frac{29{,}000\text{ ksi}}{1-(0.3)^2}\left(\left(-0.000215\,{}^{\text{in}}/_{\text{in}}\right) + (0.3)\cdot\left(0.000371\,{}^{\text{in}}/_{\text{in}}\right)\right) = -3.30\text{ ksi}$$

Since $\varepsilon_1 < \varepsilon_3$, Equation 3-30 is used to calculate the angle from the x-y plane to the principal plane:

$$\theta_{xp} = 45° - \frac{1}{2}\tan^{-1}\left(\frac{-186 - 2(206) + 342}{-186 - 342}\right) = 32.1°$$

The state of stress on the x-y plane can now be expressed using Equation 3-31, Equation 3-32, and Equation 3-33:

$$\sigma_x = \frac{\sigma_P + \sigma_Q}{2} + \frac{\sigma_P - \sigma_Q}{2}\cos(2\theta_{xp}) = \frac{9.77 + (-3.30)}{2} + \frac{9.77 + (-3.30)}{2}\cos(2 \cdot 32.1°) = 6.08 \text{ ksi}$$

$$\sigma_y = \frac{\sigma_P + \sigma_Q}{2} - \frac{\sigma_P - \sigma_Q}{2}\cos(2\theta_{xp}) = \frac{9.77 + (-3.30)}{2} - \frac{9.77 - (-3.30)}{2}\cos(2 \cdot 32.1°) = 0.39 \text{ ksi}$$

$$\tau_{xy} = -\frac{\sigma_P - \sigma_Q}{2}\sin(2\theta_{xp}) = -\frac{9.77 - (-3.30)}{2}\sin(2 \cdot 32.1°) = -5.88 \text{ ksi}$$

Figure 3-25 shows how the experimental data corresponds with the theoretical predictions for this pre-buckling load level.

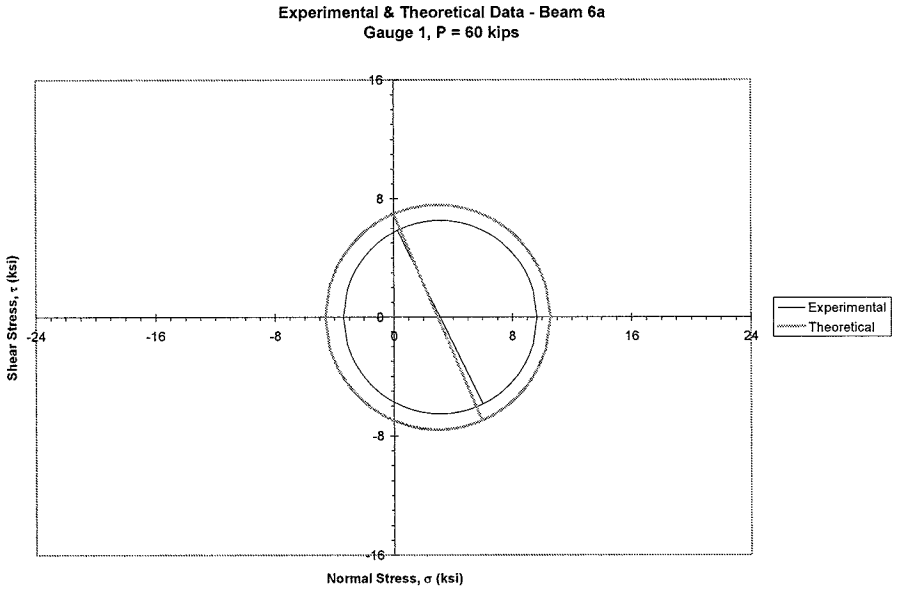

Figure 3-25. Mohr's Circles: State of Stress Comparison (x-y Planes Shown)

At the same load level, the flexural stress can be calculated at the flange gauge locations. Strain data from flange Gauge 1 on either side of the web is given as:

EF1: 435 με WF1: 342 με

Averaging the data from opposite sides of the web panel:

$$AF1 = \frac{EF1 + WF1}{2} = \frac{435 + 342}{2} = 389\,\mu\varepsilon = \varepsilon$$

Using Hooke's Law as given in Equation 3-37:

$$\sigma = E \cdot \varepsilon = (29{,}000\text{ ksi}) \cdot \left(0.000389\,{}^{\text{in}}/_{\text{in}}\right) = 11.3\text{ ksi}$$

Theory predicted the flexural stress at this location to be 12.0 ksi.

Stiffener gauges are dealt with in a similar manner. Strain data from stiffener gauge location 1 is given as:

EB1: 3.13 με WB1: 24.5 με

Average value of the recorded strain data is:

$$AB1 = \frac{EB1 + WB1}{2} = \frac{3.13 + 24.5}{2} = 13.8\,\mu\varepsilon = \varepsilon$$

The normal stress is determined using Hooke's Law:

$$\sigma = E \cdot \varepsilon = (29{,}000\text{ ksi}) \cdot \left(0.0000138\,{}^{\text{in}}/_{\text{in}}\right) = 0.40\text{ ksi}$$

Theory assumes this stress to be zero.

3.5.4 Summary Theoretical Behavior

The methods used for calculating theoretical and experimental stresses for Series II testing, as well as example calculations of each, were presented in this chapter. Theoretical stresses are calculated using classical engineering equations and Basler's tension field action theory. Experimental stresses are calculated from strain data recorded during testing. Mohr's circle equations and Hooke's Law for biaxial stress states are used to determine experimental stresses.

Included in the analysis procedure is an assumption of linear-elastic material behavior. While postbuckling behavior (yielding) is clearly non-linear, the assumption is extended to the postbuckling regions for comparison purposes nonetheless.

In the next chapter, the stresses calculated from experimental data will be compared with theory in an effort to determine if tension field action stresses are present and effectively anchored.

3.6 Summary

Chapter 3 presented the Series I (low moment high shear) and Series II (high moment high shear) test specimens and the test set up and procedures. They were selected to demonstrate tension field action in hybrid girders and to examine the moment-shear interaction of hybrid girders. Chapter 3 also demonstrated theoretical and example calculations to examine shear capacities and experimental stresses.

Chapter 4 will examine one of the Series II test girders in detail. Tension field action and moment-shear interaction will be demonstrated, along with comparison of experimental behavior to theoretical expectations. The equations demonstrated here will be used in these analyses, but the reader is referred to Zentz (2002) for a complete explanation of the procedures. Series I test results and analyses will not be shown here. The reader is referred to Rush (2001) for an equivalent presentation of the Series I tests.

Chapter 4 - Experimental Results

4.1 Introduction

The objective of this chapter is to determine the experimental tension field action shear capacity of the Series II hybrid plate girders, verify that the capacity is indeed due to tension field action stresses, and compare the results to theoretical values calculated from Basler's tension field action theory. Through physical observation of the Series II tests, the ultimate shear capacity and interaction characteristics of the test girders will be investigated, and the tension field action contribution to shear resistance will be quantified. The data taken from the tests will be used to investigate both the elastic and postbuckling stresses present in the test girders in order to verify the presence of tension field action. The Series I test girders will not be shown, except for overall behavior, since the Series II tests demonstrate the topics to be covered. The reader is referred to Rush (2001) and Schreiner (2001) for full details on the Series I test girders.

In order to maintain the flow of the text without repetition, experimental data will primarily only be presented from Beam 6a throughout this chapter. Data for all of the Series II test girders is included in the Results Volume (Zentz 2002), and will be referred to whenever experimental results are presented. Also, many of the experimental data graphs include vertical lines marked V_{cr}, V_n, M_y, or M_n. These lines represent the theoretical load levels corresponding to the critical shear buckling load, nominal shear capacity, yield moment, and nominal moment capacity, respectively.

4.2 Physical Observations

The physical observations of the experimental tests are considered prior to the interpretation of test data. The first observation is the ultimate shear capacity of the test girders, which has the potential to demonstrate that hybrid plate girders do exhibit tension field action shear capacities that can be reasonably predicted by the current AASHTO design codes. Next, the moment-shear interaction characteristics of the test girders are considered, with the intention to define what special interaction reductions, if any, hybrid plate girders might be subject to if tension field action capacity is allowed in their design. The physical failure mechanisms of the test girders are explored in order to correctly interpret the strain and deflection data taken from the tests. Finally, the experimental tension field action contribution to shear capacity will be investigated.

4.2.1 Experimental Shear Capacities

The most important observation from Series II experimental testing is the experimental shear capacity of each test girder. The experimental shear capacity has the potential to show that hybrid plate girders do have shear capacities comparable to those of similarly proportioned homogeneous girders. It will be left up to the experimental stress analysis to verify that the shear capacity is due to tension field action behavior, rather than some other mechanism.

The theoretical shear and moment capacities for the experimental test girders have been calculated using AASHTO's 1998 LRFD design equations, including tension field action for hybrid girders, and neglecting moment-shear interaction reductions. The

hybrid reduction factor, R_h, and the load-shedding reduction factor, R_b, have been included in the calculation of theoretical moment capacity for the test girders.

Shown in Table 4-1 are the experimental capacities of Series I test girders. The table illustrates the girder composition, the theoretical buckling and shear capacity, and the experimental buckling and shear capacity. The specifics on the data reduction and buckling capacity determination is not shown here for the Series I tests. The reader is referred to Rush (2001) and Schreiner (2001) for the results shown in Table 4-1. Table 4-2 are the theoretical and experimental shear capacities for the Series II test girders. All but one of the Series II test girders are hybrid 50-70 girders similar to test girders 3a and 3b in the Series I set. The following sections will present the analyses for Series II girder 6a.

Table 4-1. Theoretical and Experimental Capacities of Series I Test Girders

Test Number	Test Girder	Theoretical Shear Buckling Capacity (kips)	Theoretical Total Shear Capacity (kips)	Experimental Shear Buckling Capacity (kips)	Experimental Total Shear Capacity (kips)
1	50-50 Homogeneous	84.15	192.45	90	204.8
2	70-70 Homogeneous	84.15	208.37	143	>218
3a	50-70 Hybrid	84.15	192.45	116	211.0
3b	50-70 Hybrid	84.15	192.45	106	207.3

Table 4-2. Theoretical and Experimental Capacities of Series II Test Girders

	Beam 4	Beam 5	Beam 6a	Beam 6b	Beam 7	Beam 8
Ultimate Experimental Shear, V_u (kips)	201.0	151.0	190.3	190.6	86.3	183.4
Nominal Shear Capacity, V_n (kips)	193.3	193.3	193.3	193.3	193.3	193.3
Ultimate Experimental Moment, M_u (k-ft)	1088.8	1459.7	1284.5	1286.6	1438.3	947.6
Nominal Moment Capacity, M_n (k-ft)	1385	1385	1385	1385	1385	820
Ultimate Normalized Shear, V_u/V_n	1.04	0.78	0.98	0.99	0.45	0.95
Ultimate Normalized Moment, M_u/M_n	0.79	1.05	0.93	0.93	1.04	1.16

For both the Series I and II test girders, the shear capacity meets the AASHTO shear capacity for girders controlled by a shear only failure (Series I tests 1-3b and Series II tests 4, 6a, and 6b) ignoring moment-shear interaction reductions. The other Series II tests, tests 5, 7 and 8 were controlled by moment or moment-shear interaction failures.

AASHTO currently limits the design shear capacity of hybrid plate girders to the shear buckling capacity. As shown by Table 4-2 above, the girders failing due to shear displayed an experimental capacity of about twice the theoretical shear buckling capacity.

The experimental capacities recorded from Series I and II testing show that hybrid plate girders are capable of reaching the shear capacity calculated using AASHTO's current tension field action design equations for homogeneous sections. The strain data recorded from the experimental testing will be used later in this chapter to verify that tension field action stresses are present and responsible for the postbuckling shear capacity. In the next section, the moment-shear interaction characteristics of the test girders will be compared with proposed interaction diagrams for hybrid girders.

4.2.2 Moment-Shear Interaction

As discussed in Chapter 2, much of AASHTO's current moment-shear interaction diagram is unavailable for hybrid plate girders. For this reason, Hurst (2000) has proposed a Modified Basler Interaction Diagram for hybrid girders that greatly increases the available shear capacity for hybrid girders (see Figure 4-1). However, as discussed above, the experimental shear capacity of Series II test girders was found to be within 5% of the nominal shear capacity as computed with AASHTO's current tension field action design equations, neglecting moment-shear interaction altogether. This leads to the hypothesis that moment-shear interaction can be ignored for design. The three possible interaction diagrams (AASHTO, Hurst, No Interaction) are shown in Figure 4-2.

In order to determine which interaction diagram is most applicable to the experimental data, the experimental data will be plotted on the interaction diagrams. First, the design values of normalized shear and moment are plotted in Figure 4-3 for comparison with the experimental interaction values shown in Figure 4-4.

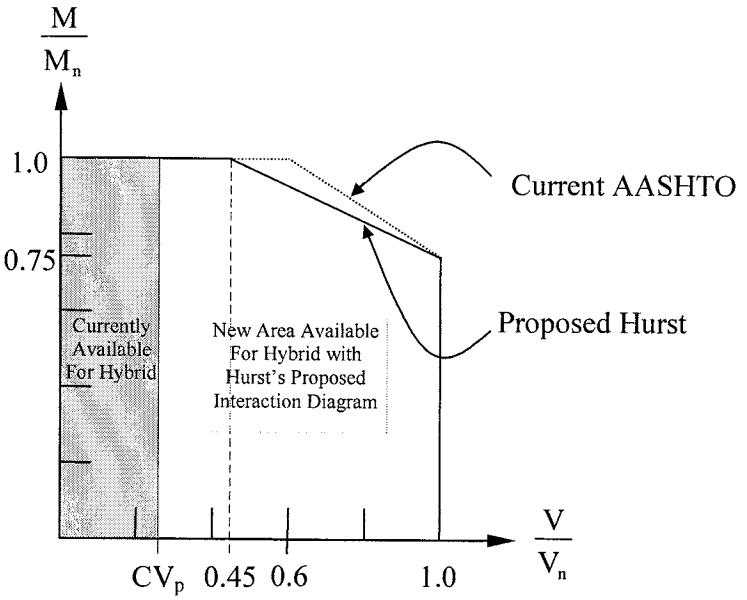

Figure 4-1. Proposed Interaction Diagram.

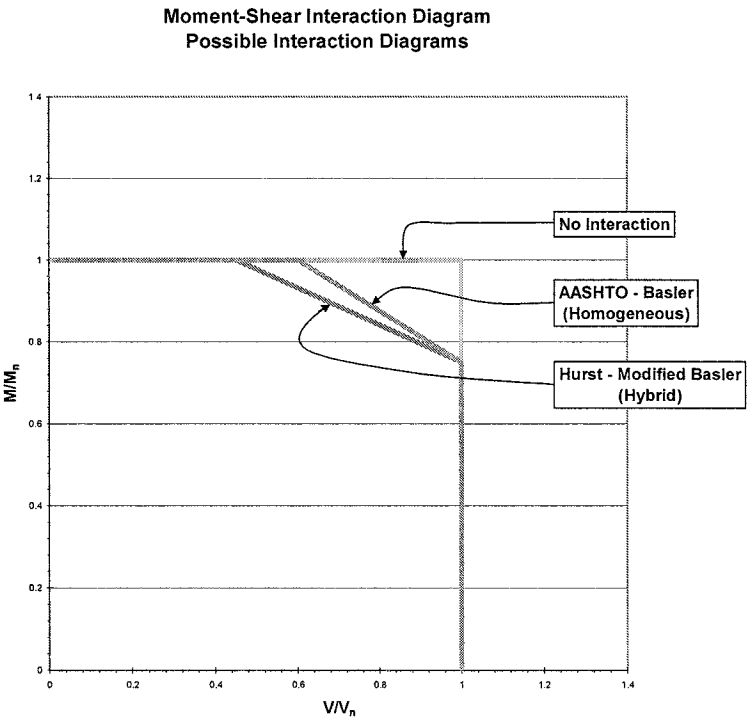

Figure 4-2. Possible Interaction Diagrams

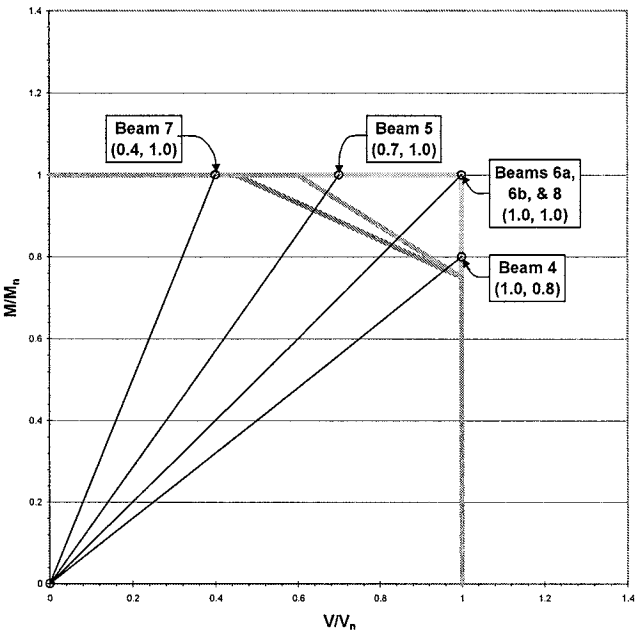

Figure 4-3. Series II Interaction Design Values

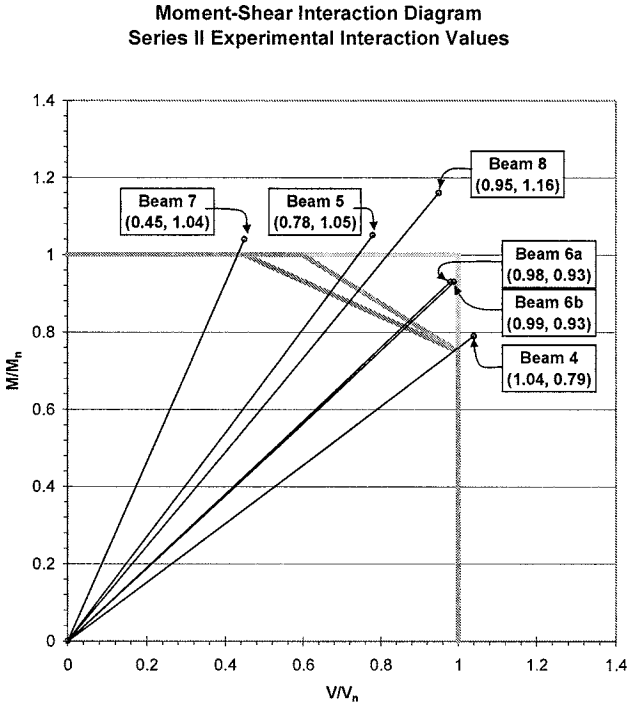

Figure 4-4. Series II Ultimate Interaction Values

From the experimental data shown in Figure 4-4, it appears that moment-shear interaction can be ignored for design. With the exception of Beams 6a & 6b, all of the test girders plot outside of the "no interaction" envelope, which indicates that those beams have more capacity than would be calculated if interaction were considered. Table 4-2 shows that Beams 6a & 6b are less than 2% below the nominal shear capacity (including TFA) at failure. This difference is within the uncertainty of shear design (Aydemir 2000).

Recent research performed at the Georgia Institute of Technology recommends that moment-shear interaction be removed from design criteria (Aydemir 2000). Aydemir performed a parametric study of tension field action behavior in hybrid plate

girders using finite element analysis. The conclusion of the study was that only girders with high depth of web in compression to web depth ratios ($D_c/D \geq 0.65$) experienced any moment-shear interaction. The extent of the interaction for these girders was small enough to suggest that the interaction be accounted for by adjustment of AASHTO resistance factors (ϕ factors) rather than traditional moment-shear interaction reductions (Aydemir 2000).

However, if the moment-shear interaction reduction is not removed from the design requirements, Figure 4-4 shows that AASHTO's current moment-shear interaction diagram for homogeneous girders is valid and conservative for the Series II hybrid test girders. Hurst's proposed hybrid interaction diagram is also valid for the test girders as shown, but is less conservative and more accurate than the current AASHTO homogeneous interaction diagram.

The experimental capacities recorded from Series II testing show that hybrid plate girders are capable of reaching the shear capacity calculated using AASHTO's current tension field action design equations for homogeneous sections. The moment-shear interaction characteristics of the test girders suggest that the interaction reduction is conservative or that the moment-shear interaction reduction may even be removed for all plate girders.

The next section will investigate the observable failure mechanisms from the Series II tests. Visual inspection of the failed test panels helps to properly interpret the test data.

4.2.3 Failure Mechanisms

The observable failure mechanisms for Series II tests varied depending upon the type of failure. Beams 4, 6a, and 6b failed in shear, while Beam 7 experienced failure due to flexure. Beams 5 and 8 showed signs of a combined moment-shear failure. All of the Series I test girders (Schreiner 2001) failed in a shear mode (except the homogeneous 70 ksi girder which did not fail). Only the Series II test girders will be discussed here.

In general, the characteristics of each failure include lateral web buckling and development of a tension strut, followed by formation of a plastic hinge in the compression flange. Visual out-of-plane distortion was observed to begin at load levels well below the theoretical buckling load. While theory assumes that buckling of the web plate does not occur until the critical shear buckling stress is obtained, it is intuitive that buckling of a slender plate with some initial curvature will begin as soon as a compressive load is applied to the plate. Although each test was unique, out-of-plane web distortion was visually apparent at load levels as low as 40 kips (about half of the calculated shear buckling load). At high load levels, the diagonal strains across the shear panel became large enough to cause shedding of mill scale, forming a visible tension strut across the web. Eventually, a plastic hinge forms in the compression flange where the tension strut anchors to the flange. When the hinge forms, end deflections of the girder increase rapidly and the girder is considered failed.

A typical shear failure is shown in Figure 4-5. A tension strut running diagonally from the upper corner of the test panel at the bearing stiffener to the opposite lower corner of the panel characterizes a shear failure. Since the tension strut runs along the diagonal of the test panel, it appears that the tension field stresses also act along the angle

of the diagonal (33.7°), rather than at half of the angle of the diagonal of the panel (16.8°), as suggested by Basler (Rush 2001). Figure 4-6 compares the indicated angles on the failed test panel from Beam 6b.

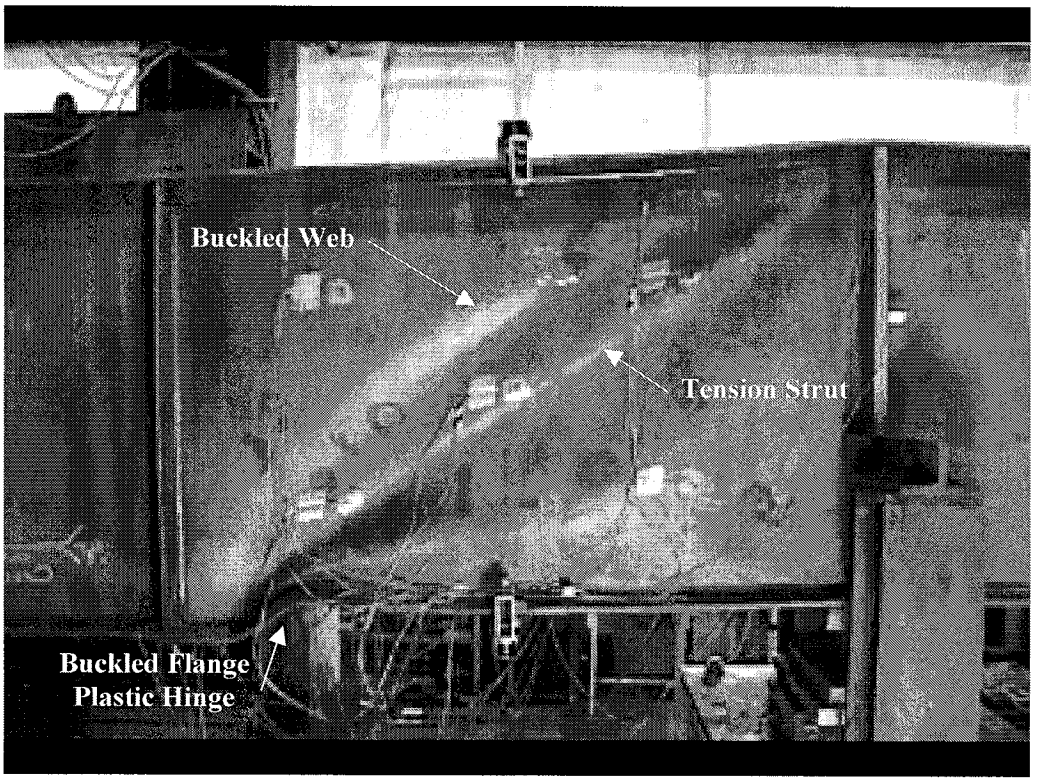

Figure 4-5. Typical Shear Failure Characteristics (Beam 6a)

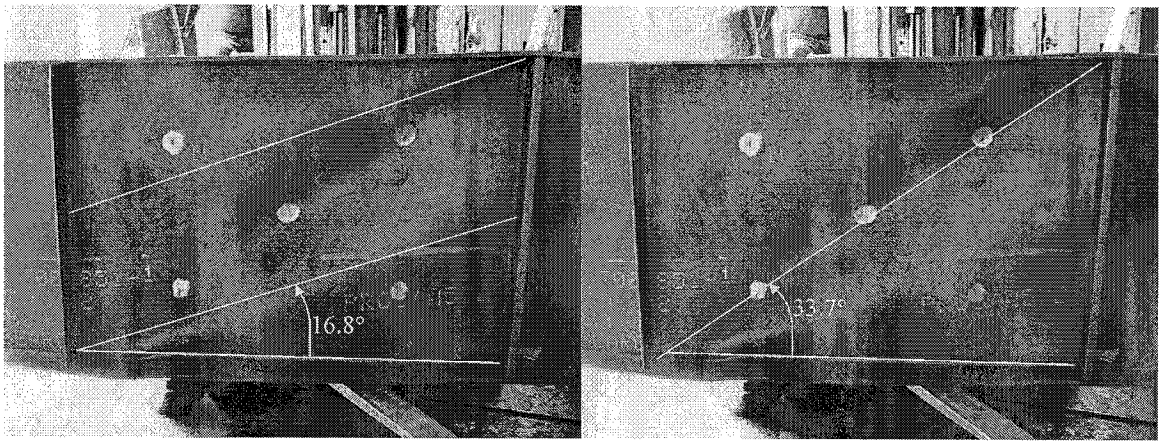

Figure 4-6. Tension Field Stress Direction Comparison for Shear Failure (Beam 6b)

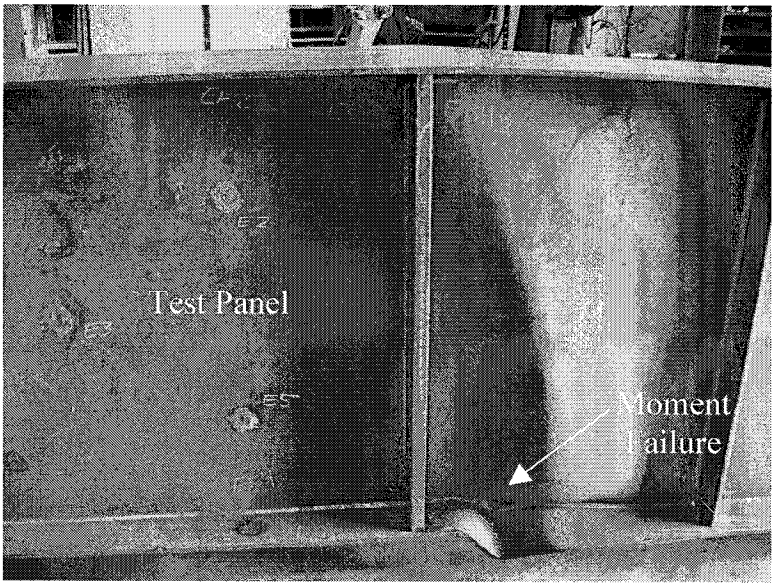

Figure 4-7. Moment Failure in Adjacent Shear Panel

Moment failures do not have tension struts running across the diagonal of the test panel. Rather, the web buckles along a line from the upper corner of the test panel at the bearing stiffener to the compression flange at a steep angle, intersecting the flange within the shear panel length. The compression flange buckles at this point and forms a plastic hinge, signifying failure of the beam. The general characteristics of a moment failure are shown in Figure 4-7.

Beam 7 ($M/M_n = 1.04$, $V/V_n = 0.45$, Hybrid) was designed as a flexural test with relatively low shear levels. Although precautions were not to force failure in the test panel, the girder experienced a flexural failure in the shear panel adjacent to the test panel, as shown in Figure 4-7.

Strain data taken from Beam 7 prior to buckling is still valid (Zentz 2002) and postbuckling data still reflects the strains experienced by the test panel, but that data does not represent a failure in the panel. Since Beam 7 was designed such that the nominal

moment capacity would be reached at nearly the same load level as the shear buckling capacity, very little postbuckling information was expected from this test, so the location of the failure is not a concern.

As mentioned above, Beams 5 and 8 experienced a combined moment-shear failure. The test panel of Beam 8 ($M/M_n = 1.16$, $V/V_n = 0.95$, Homogeneous) is shown below in Figure 4-8. Note that the partially developed tension strut suggests a shear failure, but the plastic hinge in the compression flange is typical of a moment failure.

The observable failure mechanisms are important to take note of in order to correctly interpret the test data. A visual inspection of the failed girder can reveal the failure type, locations of high strains, and other important information that may not be apparent from the recorded test data. After consideration is given to the observable failure mechanisms, the test data can be properly interpreted as needed. The next section will attempt to determine the experimental web buckling load using various forms of recorded test data.

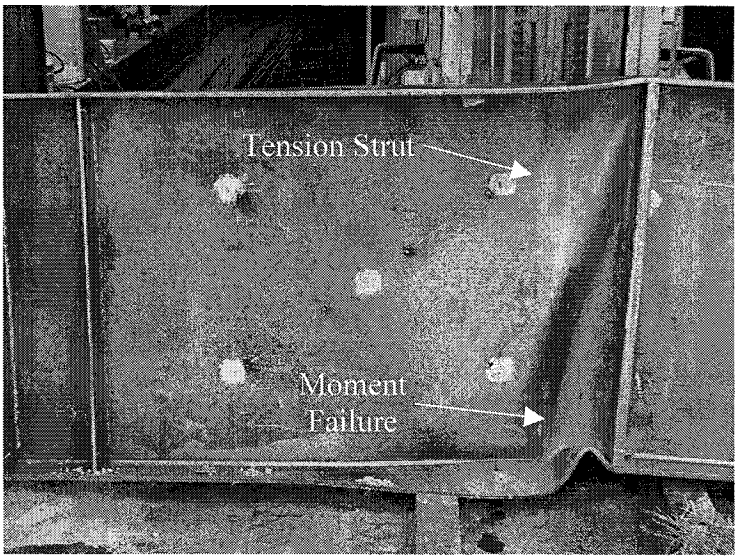

Figure 4-8. Combined Moment-Shear Behavior (Beam 8)

4.2.4 Experimental Web Buckling

In an attempt to quantify the experimental tension field action contribution to total shear capacity, an experimental shear buckling capacity is required. Once an experimental shear buckling capacity is determined, any additional capacity beyond buckling could be attributed to tension field action, provided the experimental strain patterns agree with tension field action theory.

In the interest of brevity, Beam 6a ($M/M_n = 0.93$, $V/V_n = 0.98$, Hybrid) will be used to present experimental and theoretical data for the remainder of the chapter. Full data from all test girders is included in the Results Volume (Zentz 2002). Significant data from other test girders is discussed and shown in this chapter when necessary.

As mentioned in Section 4.2.3, out-of-plane web buckling in the test girders was visually noticeable at low load levels, prior to the theoretical critical buckling load. This suggests a gradual transition from beam-type shear resistance to tension field action behavior, rather than an abrupt switch from beam to TFA resistance as suggested by theory. Therefore, it is likely that there is not a clearly defined experimental shear buckling load, but it may be possible to determine an effective shear buckling load based on the recorded data.

In the following sections, experimental web buckling will be investigated using a variety of test data. First, string pot deflection data will be used in an attempt to determine the experimental buckling load. Then the differences in data recorded by the rosette strain gauges on either side of the web will be examined. Anchorage stresses caused by the tension field may be useful in establishing the experimental buckling load, so these will be explored, as well as postbuckling stress behavior in the web panel.

4.2.4.1 String Pot Data

The most straightforward way to investigate out-of-plane buckling based on the Series II test setup and instrumentation is to use the string pot data, which tracks out-of-plane deflections of the web panel. The experimental buckling load could be determined if the string pot data showed a sharp increase in web deflection at a certain load level. Data recorded from Beam 6a is shown in Figure 4-9. Data for all tests can be found in Results Volume Chapter A (Zentz 2002).

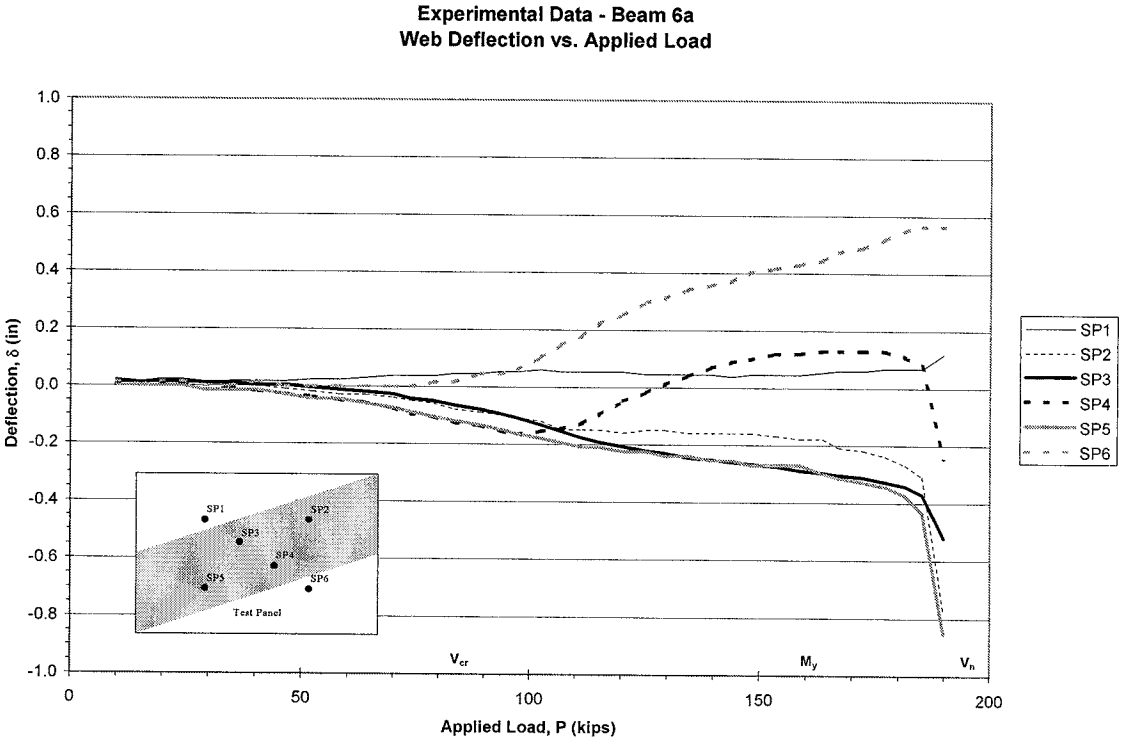

Figure 4-9. Web Deflection vs. Applied Load

The string pot web deflection data shows that the out-of-plane web deflections begin from initial loading, and increase relatively smoothly as additional load is applied.

There are no sharp changes or discontinuities in the web deflection data that would indicate a clear point of buckling. The gradual deflections, beginning at low load levels, indicate a smooth transition from beam-type shear resistance to tension field action shear resistance. Another attempt to determine the experimental buckling load using rosette strain gauge data is presented in the next section.

4.2.4.2 Rosette Strain Gauge Data

As mentioned in Chapter 3, the rosette strain gauge layout is mirrored on either side of the web of the test panel in order to eliminate out-of-plane effects. It may be possible to use the raw strain data from either side of the web to determine the point of experimental web buckling.

Theoretically, the strain data recorded from the east and west rosette at any particular gauge location should be identical until web buckling. At the point of web buckling, the strain data from the east and west rosette should theoretically diverge from one another due to the curvature of the buckled web.

Web buckling is expected to be most pronounced in the center of the web of the test panel, so rosette Gauge 3 will be used for this investigation. A change in strain due to buckling is most likely to be recorded by a strain gauge oriented perpendicular to the direction of buckling. Gauge direction 1 is most nearly perpendicular to the expected direction of web buckling, so east and west gauge 3-1 will be used for this investigation. Strain data from Beam 6a is shown in Figure 4-10. Data for all test girders can be found in Results Volume Chapter B (Zentz 2002).

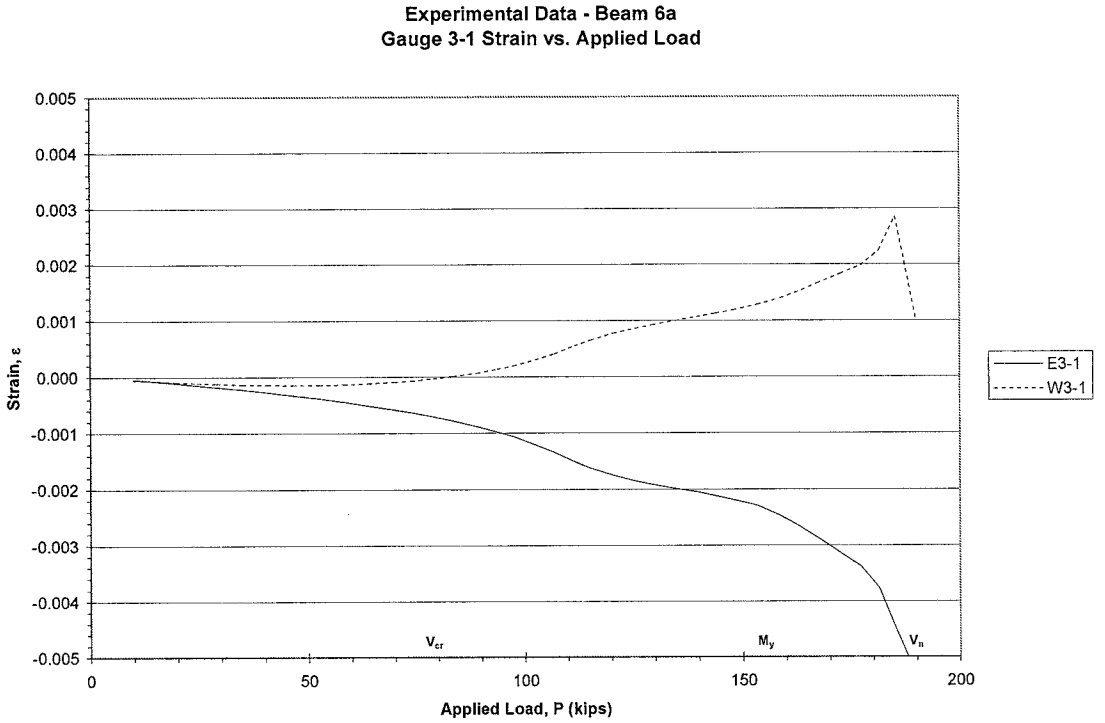

Figure 4-10. Raw Strain Data from Gauge Location 3-1

The rosette strain gauge data shows that the strains recorded from the east and west sides of the web panel begin to diverge at very low load levels. There are no sharp discontinuities in the data that suggest a definite buckling load. The data agrees with the theory of a gradual transition from beam to TFA shear resistance. Anchorage stresses caused by the tension field will be inspected in the next section.

4.2.4.3 Tension Field Anchorage Stresses

According to Basler's tension field action theory, tension field action stresses anchor to the stiffeners and flanges that make up the border of each shear panel. Theoretically, the anchorage stresses tend to cause increased compressive stresses in both

the stiffeners and flanges. Since the tension field stresses are theoretically not present in the web prior to buckling, there should be no anchorage stresses until buckling.

To investigate the appearance of anchorage stresses, the linear strain gauges on the stiffeners and flanges will be used. The experimental stresses in the stiffeners and flanges are plotted as a function of applied load. The anchorage stresses should cause the experimental stresses in theses members to become more compressive following web buckling. Figure 4-11 shows experimental stiffener stresses. Flange stresses are displayed in Figure 4-12. Stiffener and flange stress data for all tests can be found in Results Volume Chapters C and D (Zentz 2002), respectively.

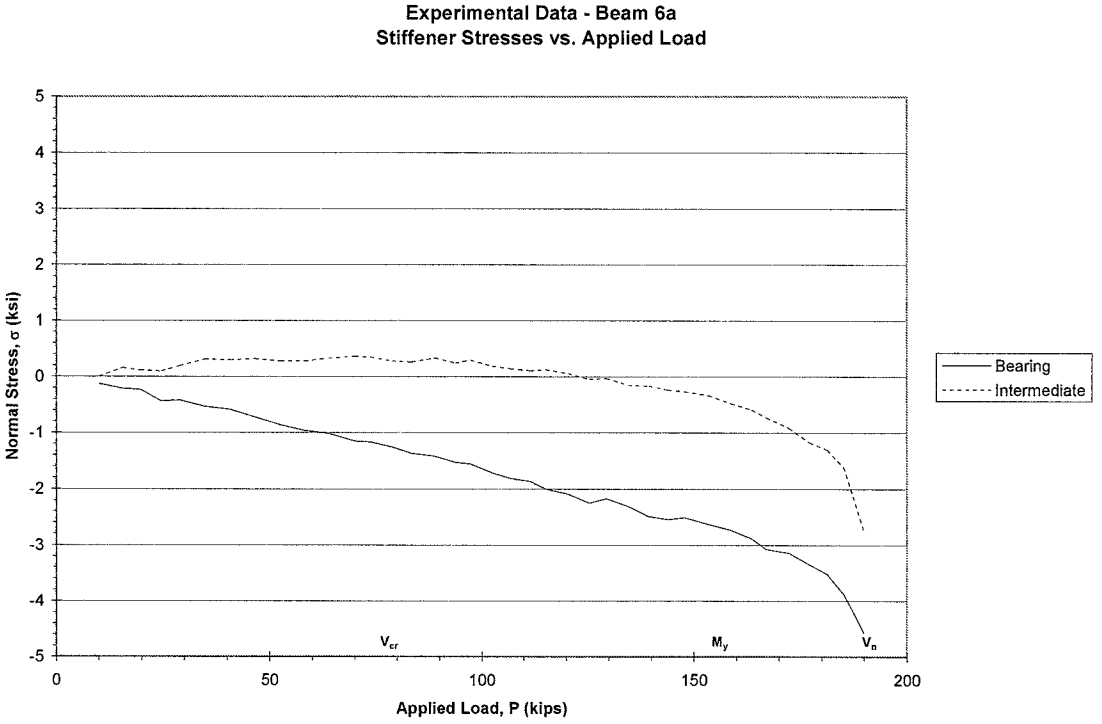

Figure 4-11. Stiffener Stresses vs. Applied Load

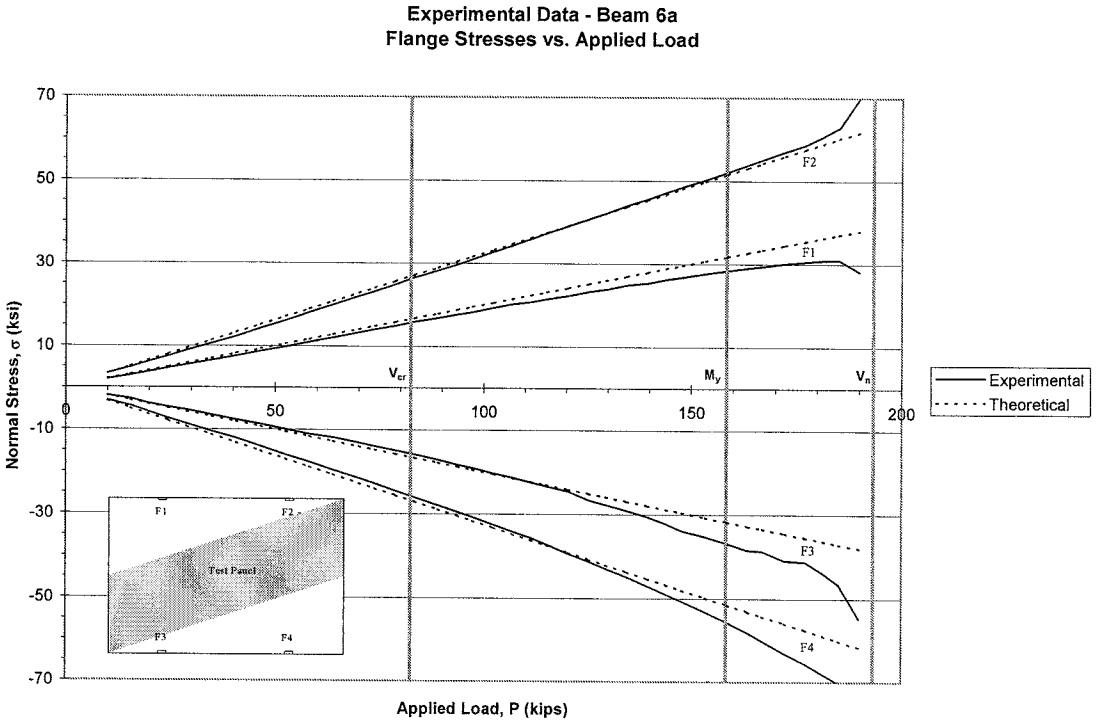

Figure 4-12. Flange Stresses vs. Applied Load

The flange and stiffener data provides little information on the experimental buckling load. Flange stresses appear to be linear, as predicted by beam theory, and neither the flange nor stiffener data show any significant compressive discontinuities that would indicate the introduction of anchorage stresses. Rather, it appears that any compressive stresses due to tension field anchorage increase gradually from initial loading, which again suggests a gradual transition from beam to TFA shear resistance.

4.2.4.4 Postbuckling Stress Behavior

The experimental web buckling load could potentially be determined through the web stress behavior that occurs after buckling. As discussed in Chapter 2, Basler assumes that once the critical shear buckling stress is reached, the shear on the u-v plane remains constant. Basler derived the postbuckling stresses using an element at the neutral axis, so the experimental investigation will use Gauge 3, located at the neutral axis in the center of the test panel. Recall that Basler calculated the angle of inclination of the u-v plane to be 16.8° for our test panel dimensions.

The experimental shear buckling load is calculated by the intersection of trend lines that represent the initial slope of the shear stress plot and the stress level at which the shear becomes constant (Zentz 2002). Figure 4-13 shows the determination of the experimental shear buckling load for Basler's u-v plane. Data for all tests can be found in Results Volume Chapter E (Zentz 2002).

As discussed in Section 4.2.3, it has been observed that the apparent angle of tension field stresses is equal to the diagonal angle of the shear panel. The angle of application of tension field stresses is how Basler defines the u-v plane, but that angle was calculated to be half of the panel diagonal angle. During the analysis of Series I tests, Rush (2001) found that the tension field stresses acted along the shear panel diagonal and the experimental stresses more closely matched their theoretical values if ϕ is taken to be the angle of the panel diagonal. The Series II test analysis also includes this investigation. The determination of the experimental shear buckling stress for Rush's u-v plane is shown in Figure 4-14. Data for all tests is given in Results Volume Chapter E (Zentz 2002).

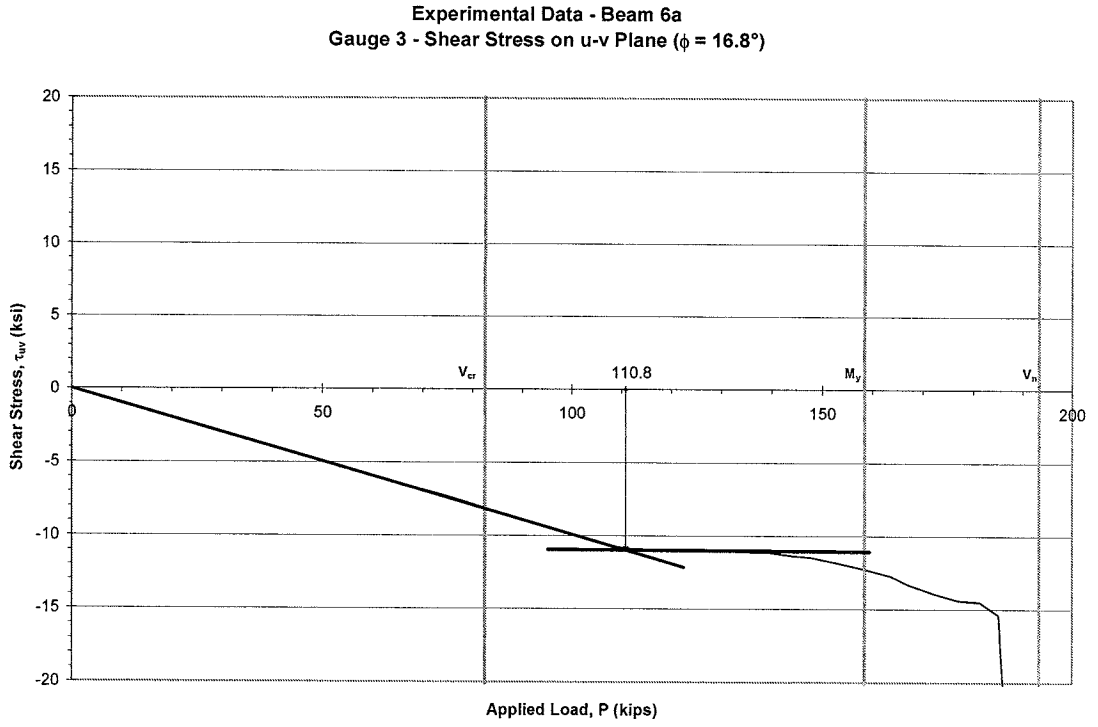

Figure 4-13. Shear Stress vs. Applied Load (Basler u-v Plane)

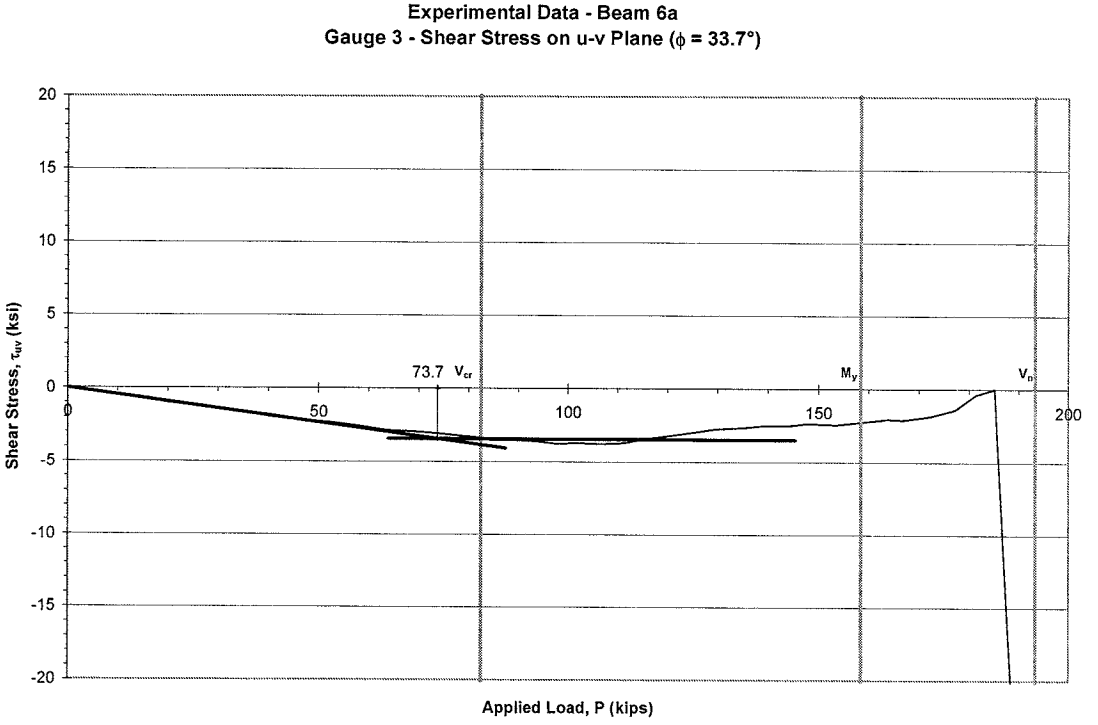

Figure 4-14. Shear Stress vs. Applied Load (Rush u-v Plane)

As is apparent from the above charts, the inclination of the u-v plane has a significant impact on the measured experimental buckling load. For $\phi = 16.8°$, the experimental buckling load is found to be 110.8 kips, compared to 73.7 kips for $\phi = 33.7°$. Recall that the theoretical buckling load was calculated to be 82.4 kips.

4.2.4.5 Results of Experimental Web Buckling Investigation

The original purpose of investigating the experimental web buckling load was to be able to quantify the tension field action shear resistance of the hybrid test girders. It was found that string pot deflections, discrepancies between rosette strain gauge data from either side of the web, and anchorage stresses in the transverse stiffeners and flanges did not show a clear experimental buckling load. Postbuckling stress patterns, namely the constant shear stress on the u-v plane following buckling, were finally used to estimate the experimental web buckling load. However, this method is sensitive to the angle of inclination of the u-v plane. An investigation into the experimental inclination of the u-v plane is included later in this chapter (see Section 4.4).

The results from the investigation into experimental web buckling for all Series II test girders are shown in Table 4-3. Experimental buckling loads were found using the method shown above for all test girders except Beam 8, for which no experimental buckling load was found. For Beam 8, the shear stresses on the u-v plane increased linearly almost until failure for both $\phi = 16.8°$ and $\phi = 33.7°$ without becoming constant or changing slope significantly, so no experimental buckling load could be determined.

Table 4-3. Experimental Web Buckling Results

		Beam 4	Beam 5	Beam 6a	Beam 6b	Beam 7	Beam 8
Theoretical	Shear Buckling Capacity (kips)	82.4	82.4	82.4	82.4	82.4	82.4
	Nominal Shear Capacity (kips)	193.3	193.3	193.3	193.3	193.3	193.3
	Nominal Moment Capacity (kip-ft)	1385.0	1385.0	1385.0	1385.0	1385.0	780.0
	TFA Shear Capacity (kips)	110.9	110.9	110.9	110.9	110.9	110.9
Experimental	Shear Buckling Capacity (kips)	47.2	72.3	73.7	88.6	46.2	NA
	Ultimate Shear Capacity (kips)	201.0	Combined M-V Failure	190.3	190.6	Moment Failure	Combined M-V Failure
	Ultimate Moment Capacity (kip-ft)	Shear Failure	1459.7	Shear Failure	Shear Failure	1438.3	947.6
	TFA Shear Capacity (kips)	153.8	Combined M-V Failure	116.6	102.0	Moment Failure	Combined M-V Failure

Notice in Table 4-3 that the experimental tension field action shear capacity is close to the theoretical values for the beams that failed due to shear (Beams 4, 6a, and 6b). This helps to demonstrate that the current AASHTO tension field action design equations for homogeneous girders predict the postbuckling shear capacity of hybrid girders reasonably well. Note that the experimental TFA shear capacity of moment failures is inconclusive, since these girders do not develop the full TFA capacity before failing in flexure.

Now that the experimental buckling load and TFA shear capacities have been determined, the stress analysis needs to show that the experimental stresses in the test girders behave according to Basler's tension field action theory in order to verify that the additional shear capacity beyond beam theory is in fact due to tension field action. The next section will begin by verifying pure beam behavior at low levels of applied load.

4.3 Elastic Stresses

In order to verify tension field action behavior in the Series II test girders, it is necessary to show that the girders initially resist shear in a beam-type manner, as assumed by Basler. For this purpose, experimental data recorded by the rosette strain gauges will be compared to beam theory, calculated as demonstrated in Chapter 3. Experimental data involved in the elastic stress investigation includes x-y plane stresses, principal stresses, Mohr's circles to describe the states of stress at a discrete load levels, and flexural stress distributions.

First, the normal and shear stresses on the x-y plane are plotted as a function of applied load. The x-y stresses can be compared to theory for every gauge location on the web in order to verify beam behavior at low load levels. As an example, the x-y stresses in the elastic range for Gauge 3 are compared to theoretical values in Figure 4-15. The data for all tests and gauge locations can be found in Results Volume Chapter F (Zentz 2002).

From the data shown in Figure 4-15, it appears that the experimental x-y plane stresses closely follow the stresses calculated from beam theory at low load levels. At an applied load of about 40 kips, the x and y normal stresses (both theoretically zero for Gauge 3) begin to gain tension. This supports the hypothesis that beam-type shear resistance gradually shifts to tension field action shear resistance beginning with low load levels. Further inspection of the test data for other gauges and test girders in Results Volume Chapter F (Zentz 2002) reveals similar trends.

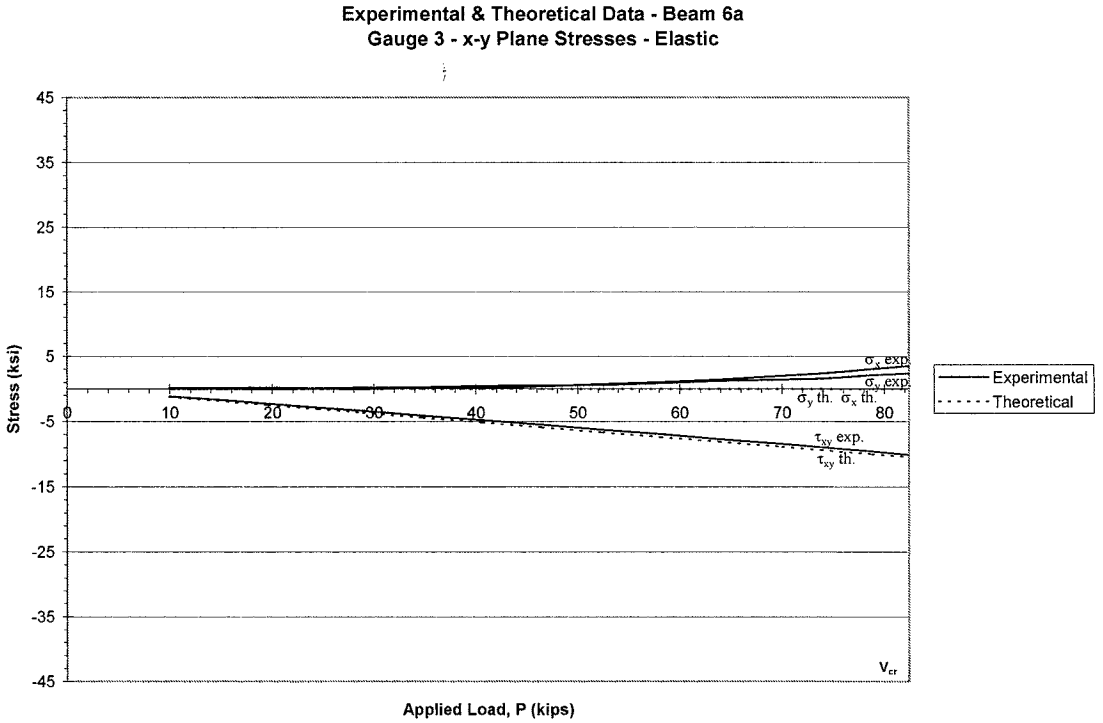

Figure 4-15. x-y Plane Stresses vs. Applied Load at Gauge 3

Next, principal stresses are computed, as well as the inclination of the principal plane. The calculations are performed for both theoretical and experimental data at every web gauge location. The experimental data is expected to closely correlate with beam theory for low load levels. As the applied shear increases, the experimental data is expected to differ from beam theory as the shear resistance mechanism gradually shifts from beam action to tension field action. The principal stresses and orientation of the principal plane in the elastic range for Gauge 3 are shown in Figure 4-16 and Figure 4-17, respectively. Refer to Results Volume Chapter G (Zentz 2002) for similar information on all gauge locations and test girders.

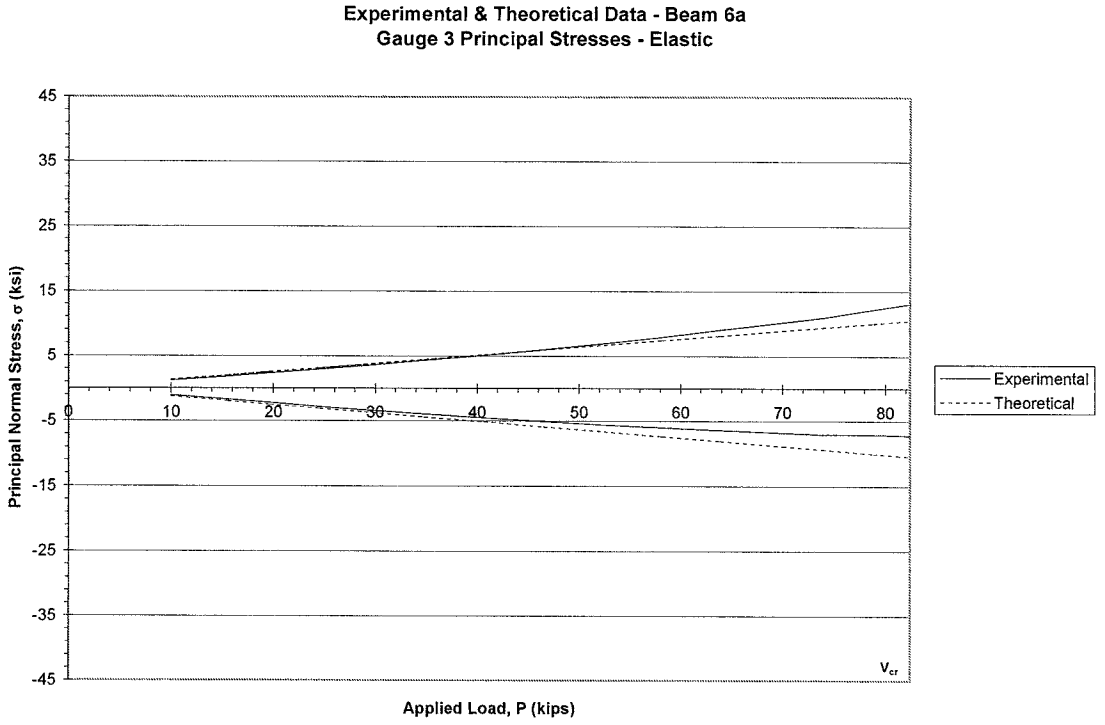

Figure 4-16. Principal Stresses vs. Applied Load for Gauge 3

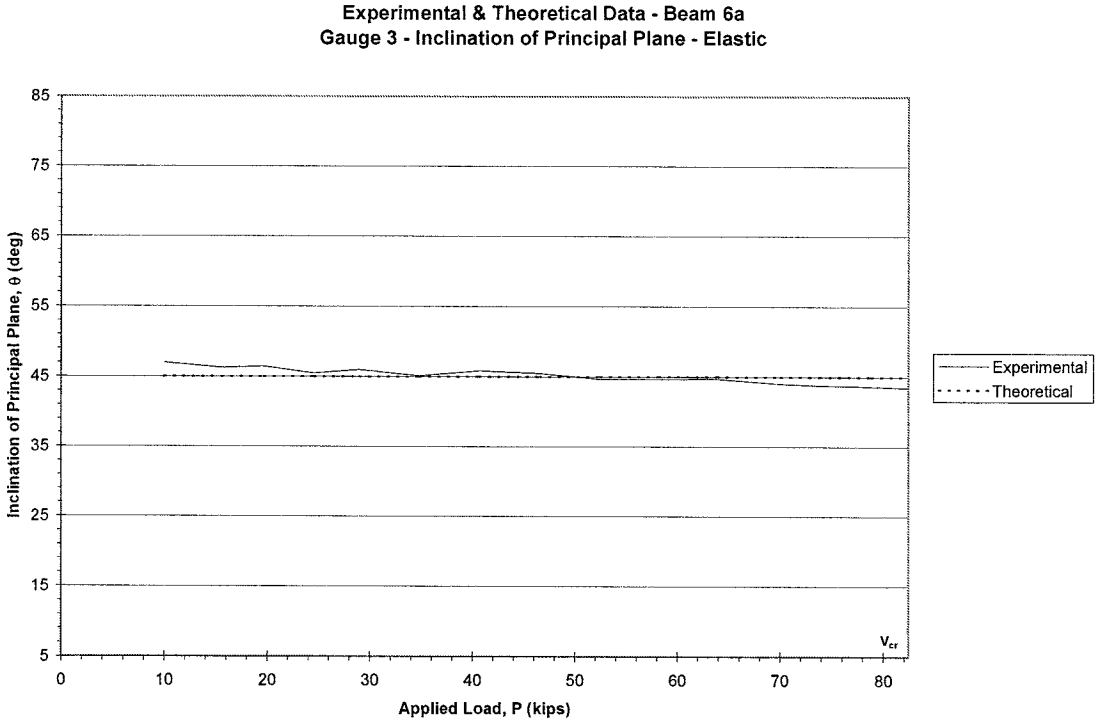

Figure 4-17. Orientation of Principal Plane vs. Applied Load at Gauge 3

Once again, the experimental data closely correlates with beam theory for low loads, but begins to gradually deviate from beam theory as the applied load increases. As expected, the principal stresses begin to become more tensile than beam theory, consistent with tension field action behavior. Also, the orientation of the principal plane begins to decrease from the theoretical 45° as tension field stresses begin to develop in the web along the u-axis. Data from Results Volume Chapter G (Zentz 2002) supports these findings.

Another way to visualize the relationship of experimental stresses to theoretical stresses is to use Mohr's circle. Mohr's circle is useful for displaying the complete state of stress at a given load level. For the elastic region, the experimental Mohr's circle can be compared to theory at every gauge location. As an example, the Mohr's circle for stress at Gauge 3 is shown for load levels of 20, 40, 60, and 80 kips in Figure 4-18 through Figure 4-21. Mohr's circle data for other gauge locations and test girders can be found in Results Volume Chapter H (Zentz 2002).

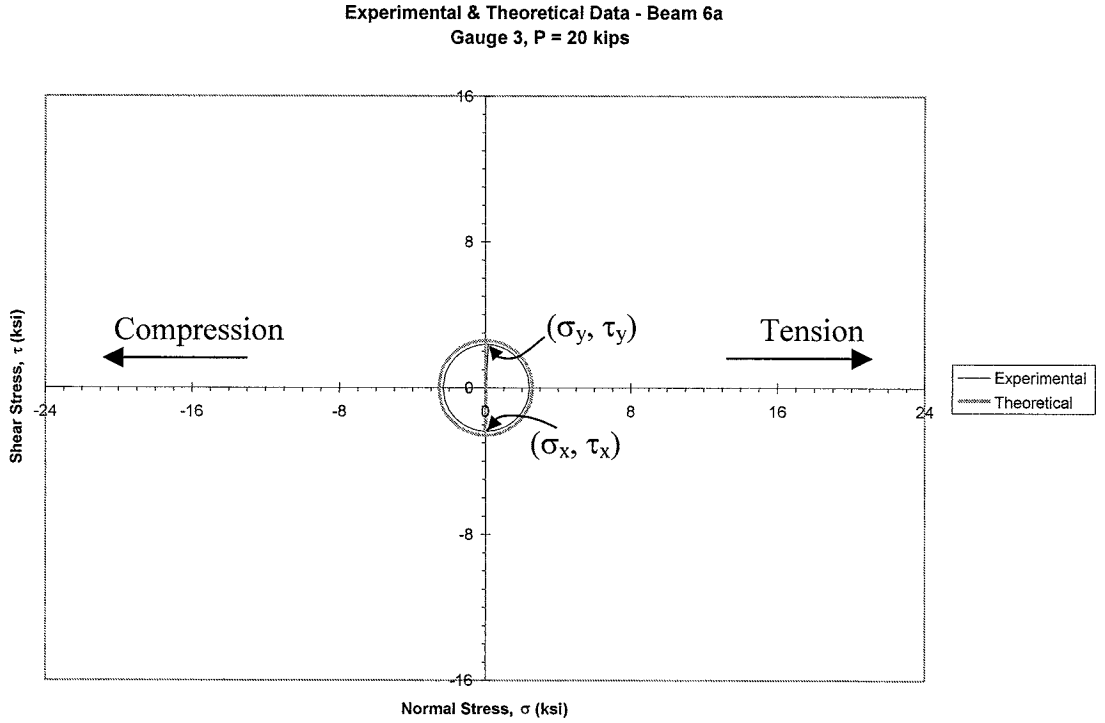

Figure 4-18. Mohr's Circle at Gauge 3 for 20 kip Applied Load

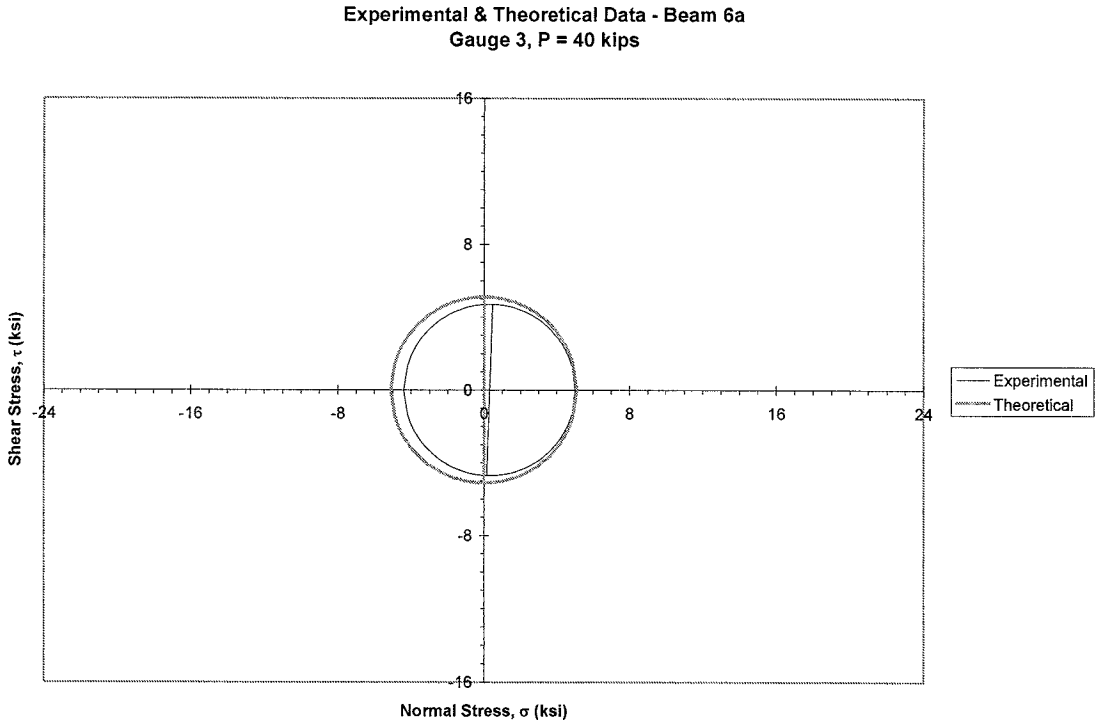

Figure 4-19. Mohr's Circle at Gauge 3 for 40 kip Applied Load

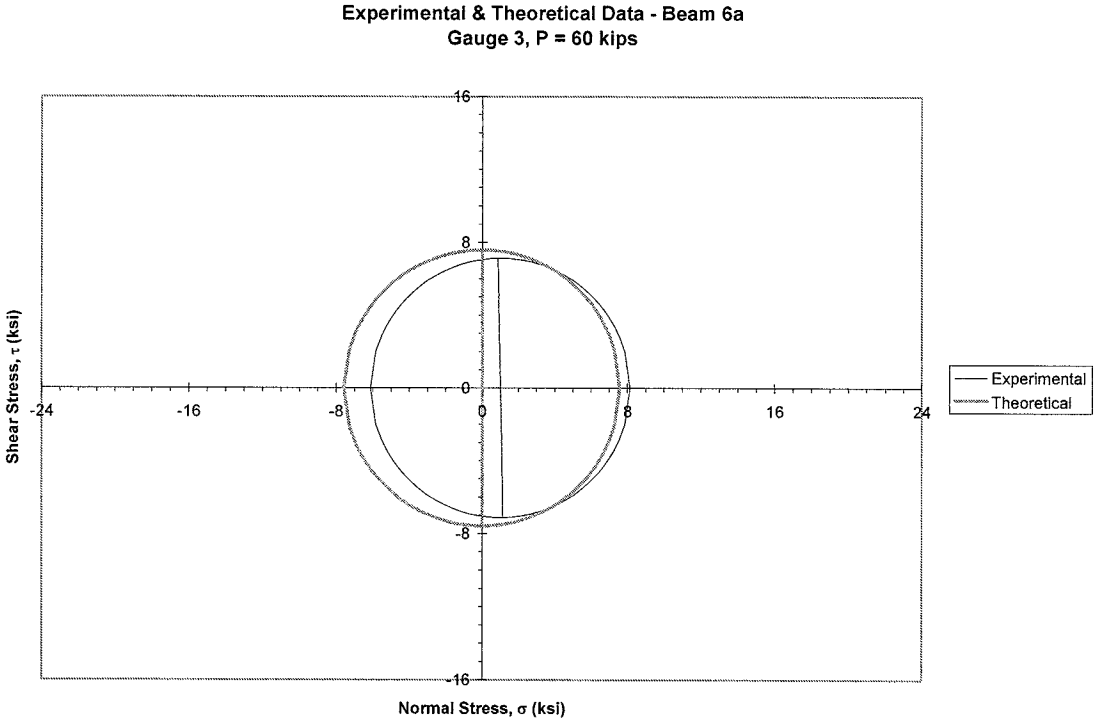

Figure 4-20. Mohr's Circle at Gauge 3 for 60 kip Applied Load

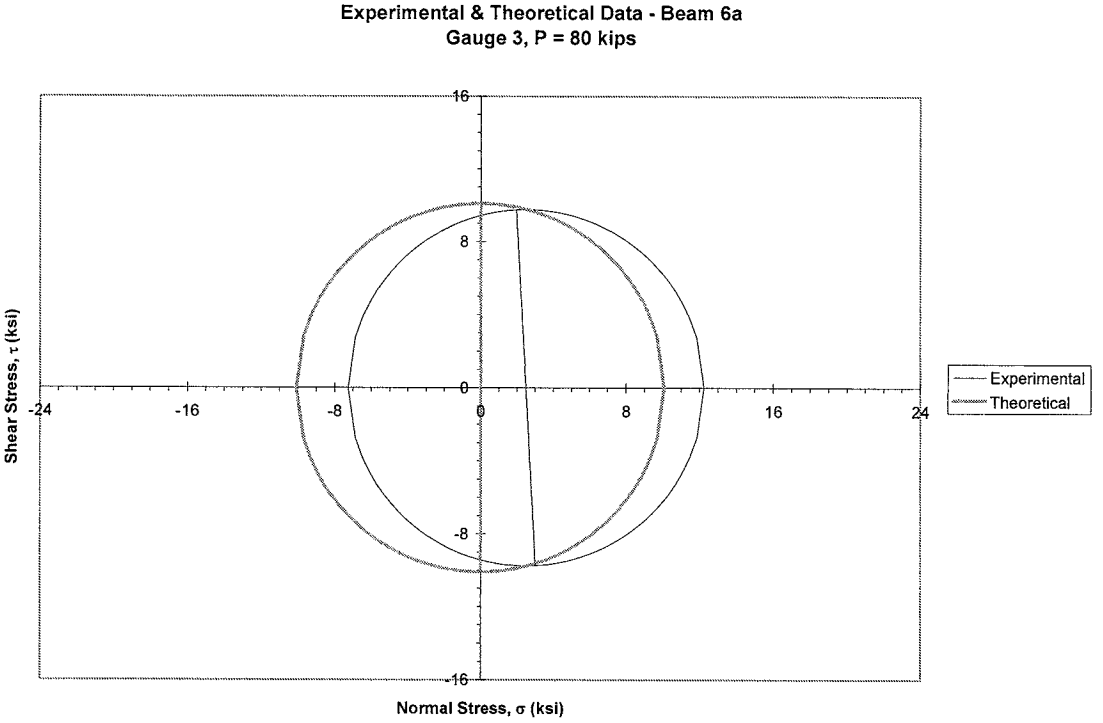

Figure 4-21. Mohr's Circle at Gauge 3 for 80 kip Applied Load

The Mohr's circle data shows that the experimental state of stress is nearly identical to the theoretical state of stress for lower load levels. As the applied load increases, the experimental state of stress experiences slightly more tension than predicted by theory, which again suggests the gradual shift from beam action to tension field action. Data from Results Volume Chapter H (Zentz 2002) shows similar trends for other gauges and test girders.

One characteristic of classical beam action is a linear flexural stress distribution. In order to investigate the experimental flexural stress distribution in the Series II test girders, a cross section is taken vertically through the center of the test panel, as shown in Figure 4-22. The x-axis normal stress from Gauge 3 is used directly, but stresses from gauges on opposite sides of the cross-section are averaged to give an approximate flexural stress value at the center of the test panel. With a limited number of gauge points and the use of averaged data, the experimental flexural stress distribution is approximate at best, but is useful for display and visualization purposes. Figure 4-23 through Figure 4-26 show the flexural stress behavior for Beam 6a in the elastic region. Results Volume Chapter I (Zentz 2002) shows flexural stress distribution data for all test girders.

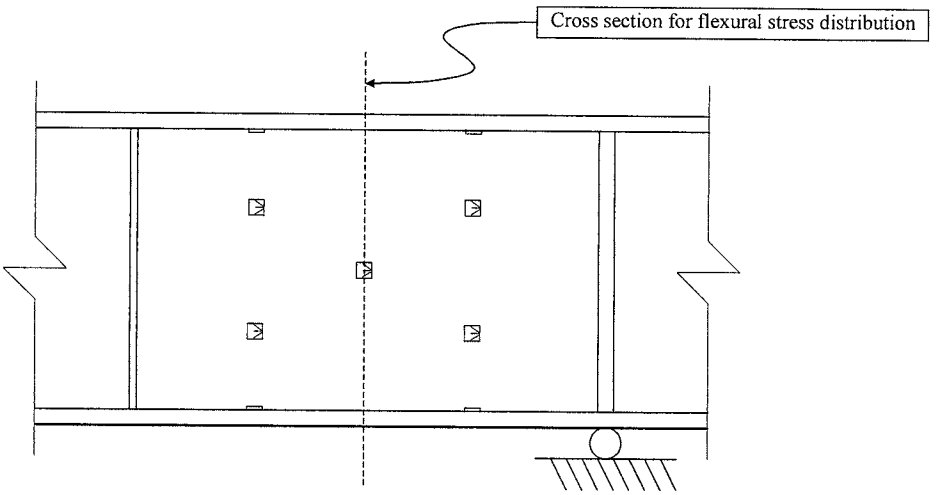

Figure 4-22. Cross Section Used To Calculate Flexural Stress Distribution

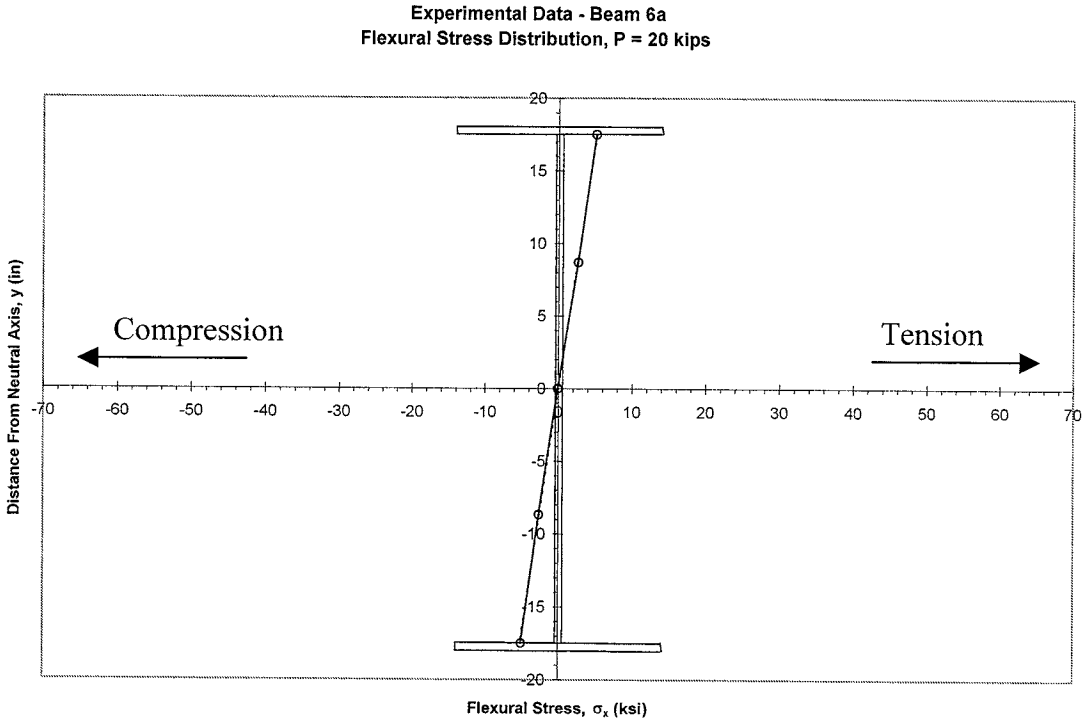

Figure 4-23. Flexural Stress Distribution for 20 kip Applied Load

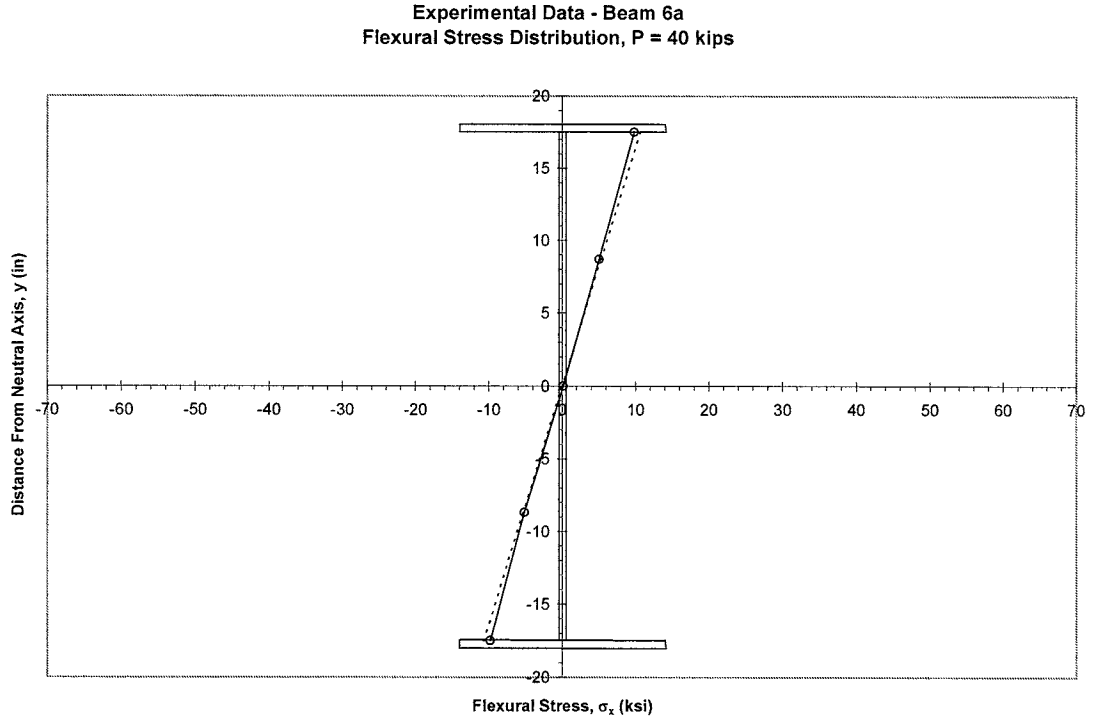

Figure 4-24. Flexural Stress Distribution 40 kip Applied Load

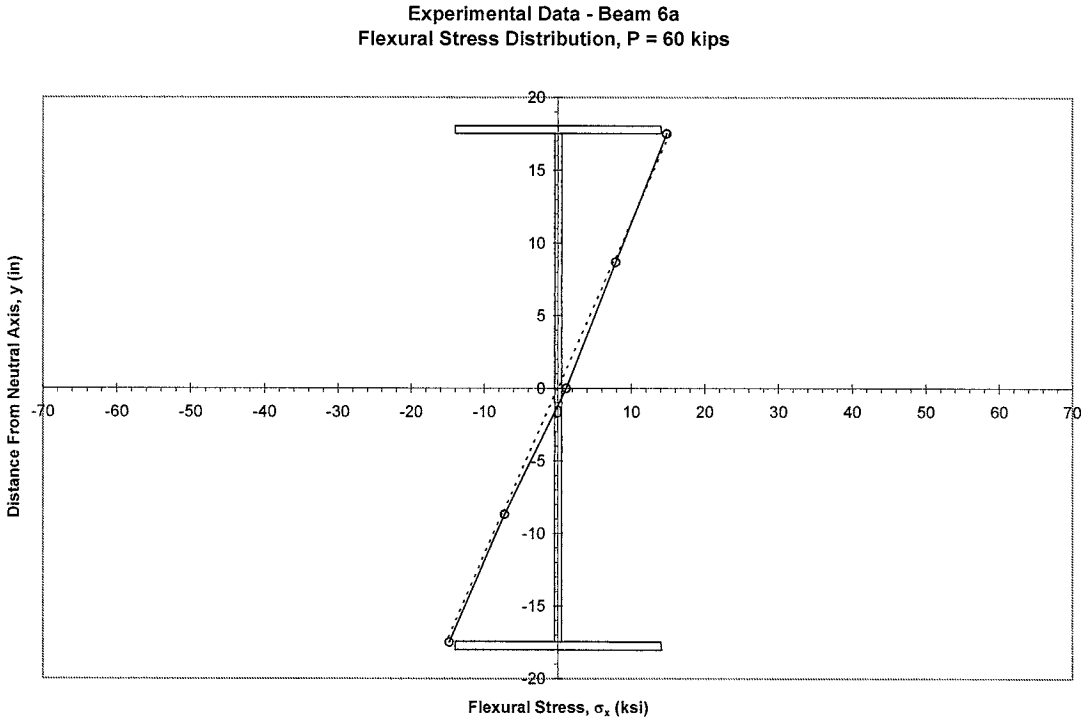

Figure 4-25. Flexural Stress Distribution for 60 kip Applied Load

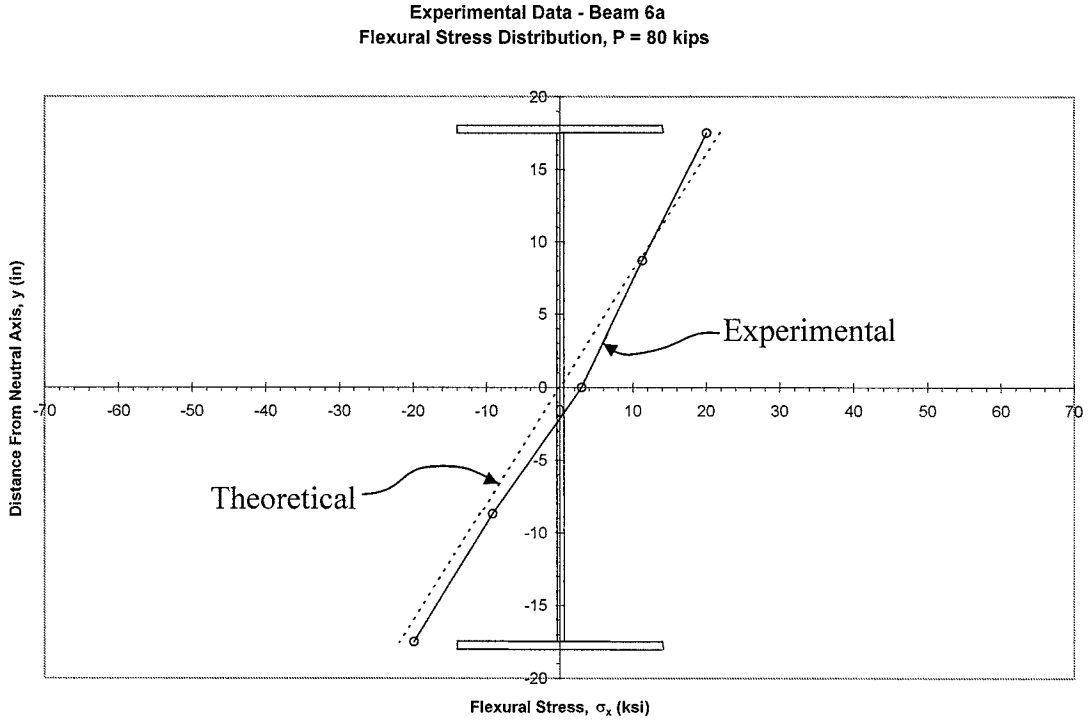

Figure 4-26. Flexural Stress Distribution for 80 kip Applied Load

The experimental flexural stress distribution data is identical to data provided by beam theory for low load levels. Notice that, as the applied load increases, the experimental flexural stress at the center of the cross section is more tensile than the theoretical value. This is the location where the tension strut will develop through this cross section. Further discussion of this topic will be left until postbuckling stresses are investigated in Section 4.4. Results are similar for other test girders, as shown in Results Volume Chapter I (Zentz 2002), with the exception of Beam 4.

During the analysis of data from Beam 4, the flexural stress distribution showed that the web stresses were not behaving as predicted. As shown in Figure 4-27, the flexural stress at the center of the test panel, which is theoretically zero, becomes

compressive as the applied load increases. Additional loading increases the compression at the center of the test panel, which raises the neutral axis toward the tension flange, which is contrary to theory at the center of the test panel.

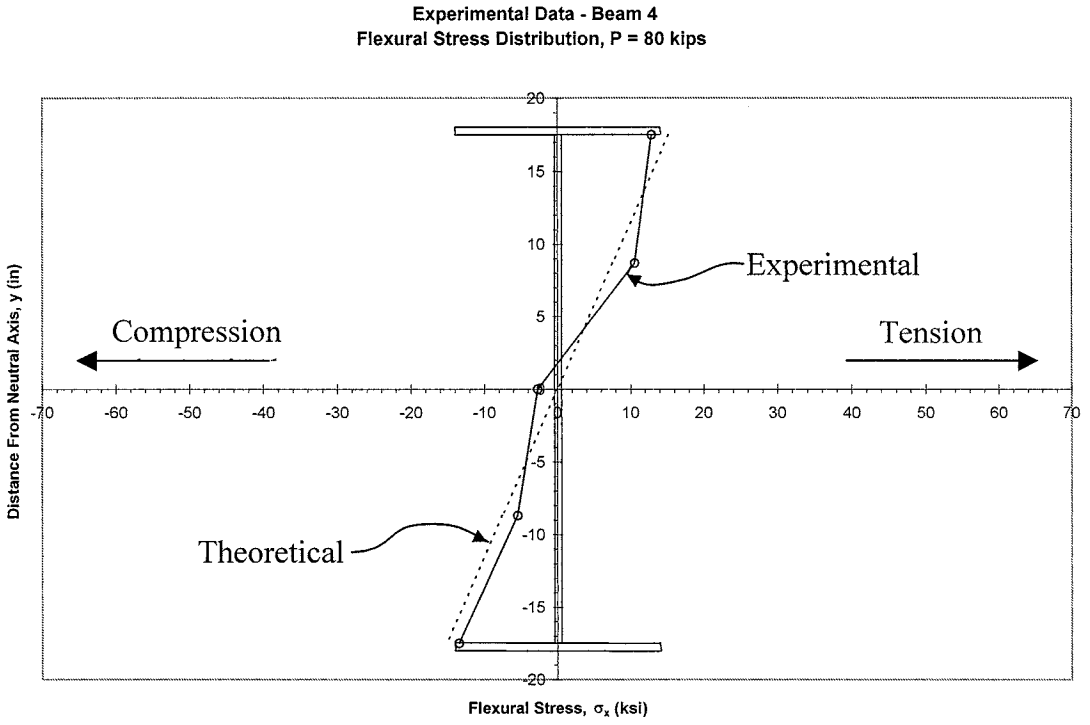

Figure 4-27. Flexural Stress Distribution for Beam 4 at 80 kip Applied Load.

Upon further inspection of Beam 4, it was concluded that the unexpected stress patterns were due to deep beam action. Deep beam action can occur in beams with a span-to-depth ratio of two or less, if simply supported (Park & Paulay 1975). Deep beam action results in a deviation of stress patterns from the classical beam theory. A typical flexural stress distribution for a simply supported deep beam under uniform load is shown in Figure 4-28.

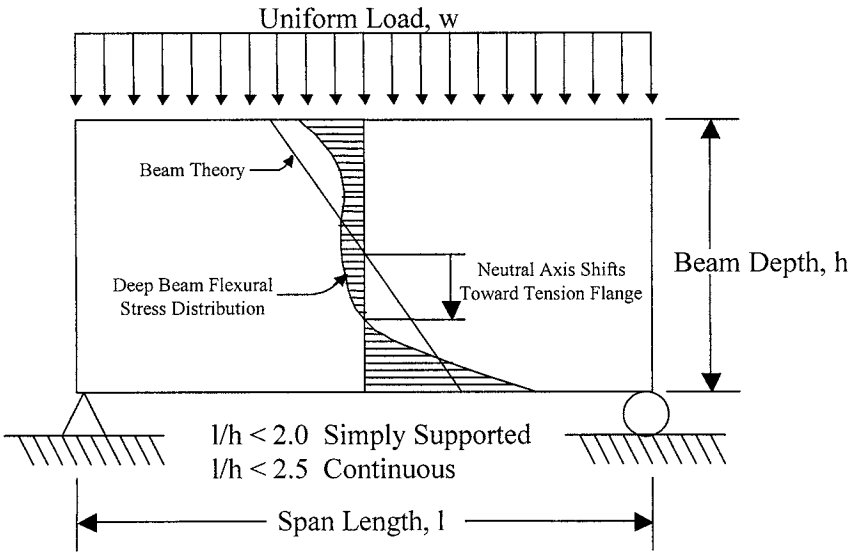

Figure 4-28. Mid-span Flexural Stress Distribution of Simply Supported Deep Beam

Beam 4 has a shear span-to-depth ratio of 65"/36" = 1.81. The flexural stress distribution for Beam 4 at a load of 160 is shown in Figure 4-29. The experimental flexural stress distribution resembles the distribution for deep beams shown in Figure 4-28. It is believed that the stress patterns present in Beam 4 are due to deep beam action. The interaction of deep beam action and tension field action is beyond the scope of this thesis and will not be investigated here. However, the ultimate shear capacity is still considered valid since the failure mechanism involved web buckling, formation of a visible tension strut, and formation of a plastic hinge in the compression flange, which is consistent with a tension field action shear failure.

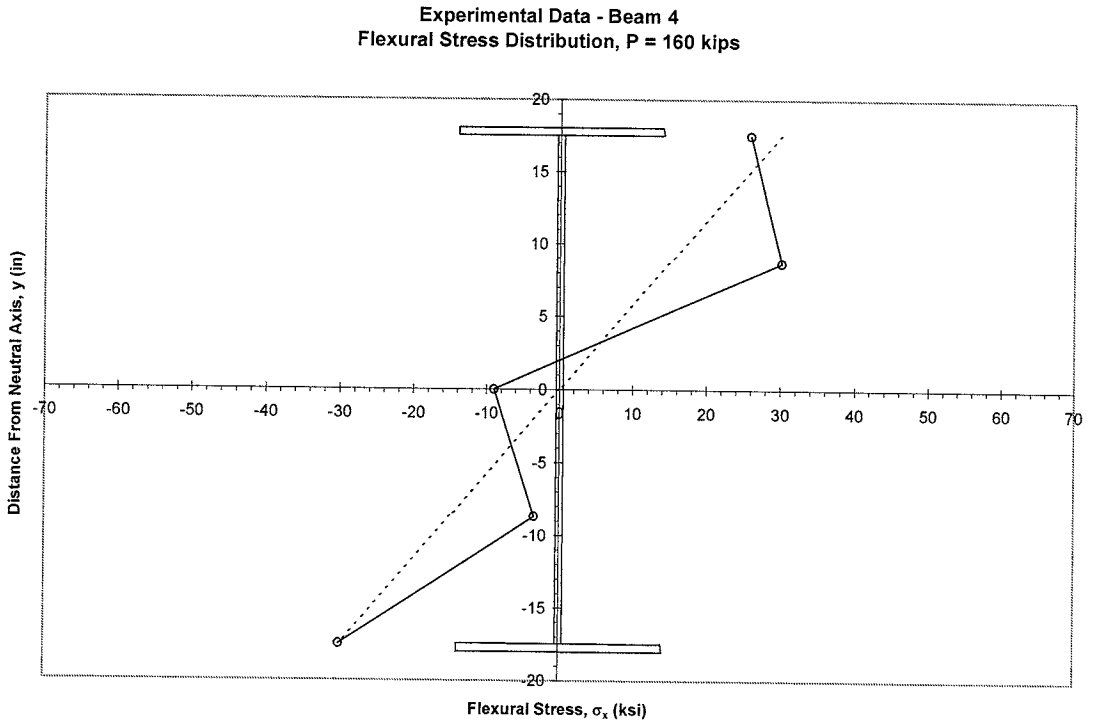

Figure 4-29. Flexural Stress Distribution for Beam 4 at 160 kip Applied Load

Several types of data from the elastic range have been presented in this section: x-y plane stresses, principal stresses, Mohr's circles, and flexural stress distributions. The common trend from all this data is that the test girders behave in a beam manner for low load levels. However, as applied load increases, the stress patterns begin to gradually shift from beam behavior to tension field action behavior. This behavior is expected since web buckling does not occur at a defined load level, but it rather slowly buckles beginning with initial loading.

Basler assumes that transversely stiffened plate girders initially resist shear in a beam-type manner, and then tension field action resists any shear load beyond the critical buckling load. The experimental buckling loads have been determined and the elastic beam stresses have been verified. The next section will investigate the presence of tension field action stresses in the postbuckling region.

4.4 Postbuckling Stresses

The final step necessary to demonstrate the tension field action shear capacity of the Series II test girders is to verify that the postbuckling stresses agree with Basler's tension field action theory. The data used to verify the postbuckling stresses includes u-v plane stresses, principal stresses, Mohr's circles, and flexural stress distributions.

Basler's tension field action theory is derived using an element at the neutral axis, so most of the experimental data used to compare with theory will come from Gauge 3, located at the center of the test panel. Theory does not provide information in the postbuckling region on the stress states of elements that are not located on the neutral axis at the center of a shear panel. Therefore, strain data recorded from gauge locations other than Gauge 3 is of limited usefulness, since there is no theoretical equivalent with which to compare.

Recall from Chapter 2 that the theoretical web buckling load is defined as the load that produces the critical shear buckling stress in an element at the neutral axis. To find the state of stress at failure, the ultimate tension field stress, σ_t, is added to the buckling state of stress along the u-axis. Basler does not specify how the incremental tension field stresses develop in the web (i.e. linearly, etc.), so for display purposes, the incremental

tension field forces will be assumed to increase linearly with applied load from theoretical buckling until failure. The theoretical stresses on the u-v plane are plotted as a function of applied load in Figure 4-30 for $\phi = 16.8°$ and Figure 4-31 for $\phi = 33.7°$.

As mentioned earlier in this chapter, it is expected that the experimental shear resistance of the test girders begins as pure beam action and gradually shifts into tension field action, rather than the abrupt change in shear resistance suggested by theory. Also, it is expected that the tension field stresses act along the diagonal of the shear panel, so the experimental data is expected to relate more closely to the theoretical stresses calculated with $\phi = 33.7°$. Figure 4-32 through Figure 4-37 compare the u-v plane stresses for $\phi = 16.8°$ and $\phi = 33.7°$. Similar data for other test girders is given in Chapter R10 (Zentz 2002).

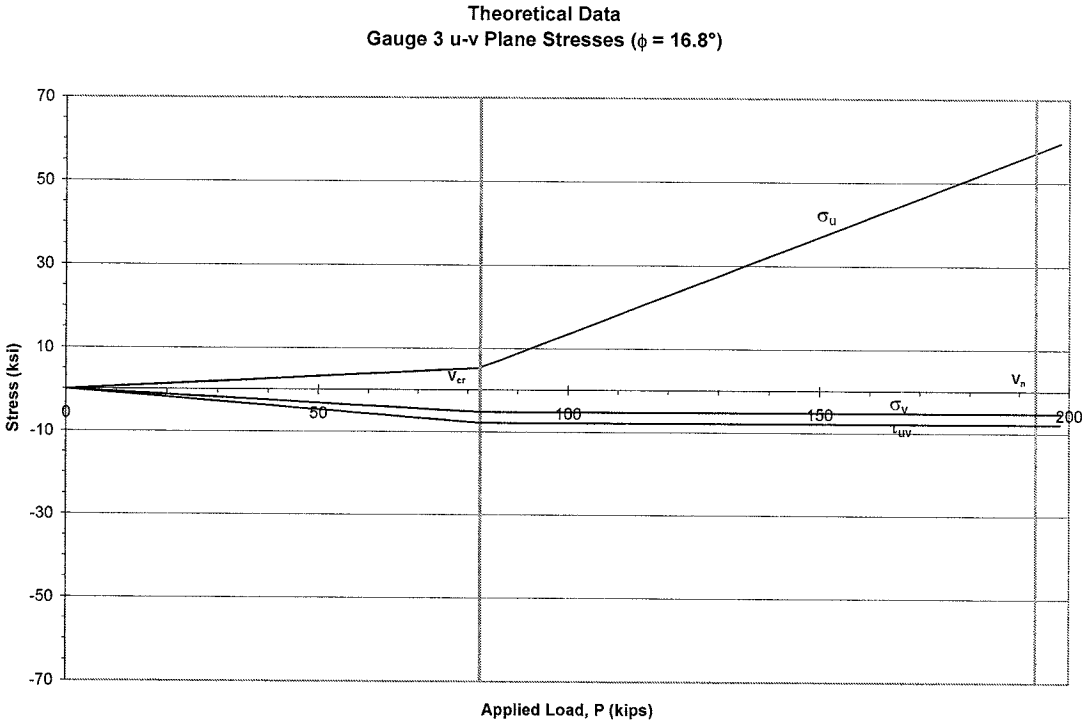

Figure 4-30. Theoretical u-v Plane Stresses for $\phi = 16.8°$

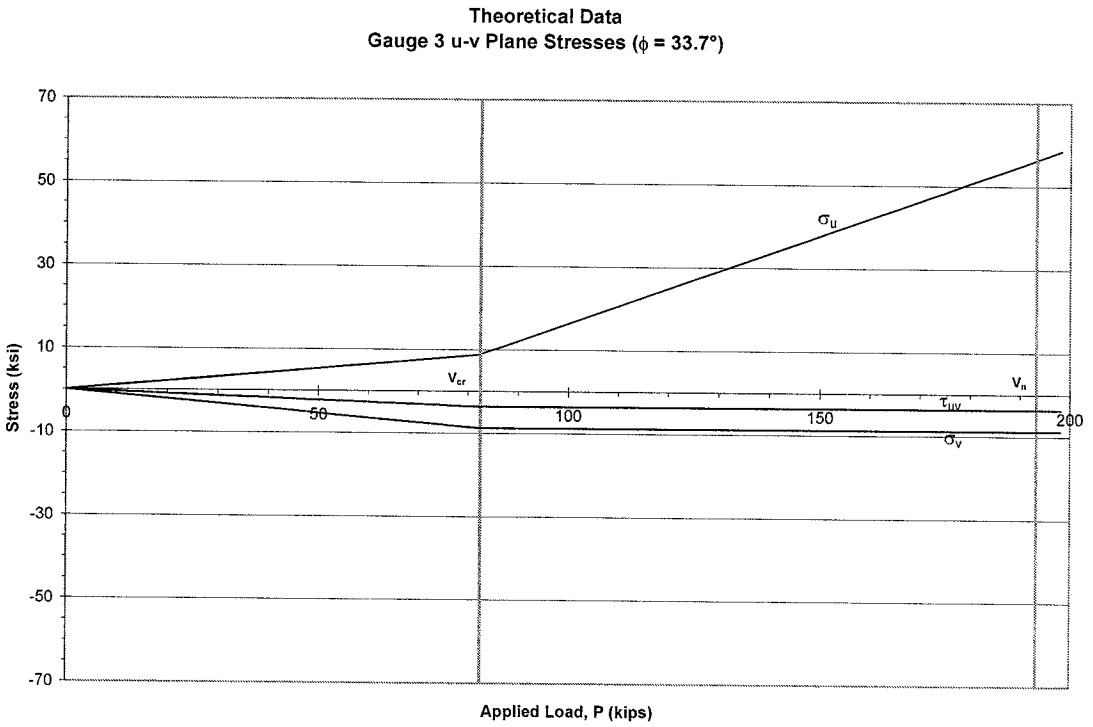

Figure 4-31. Theoretical u-v Plane Stresses for $\phi = 33.7°$

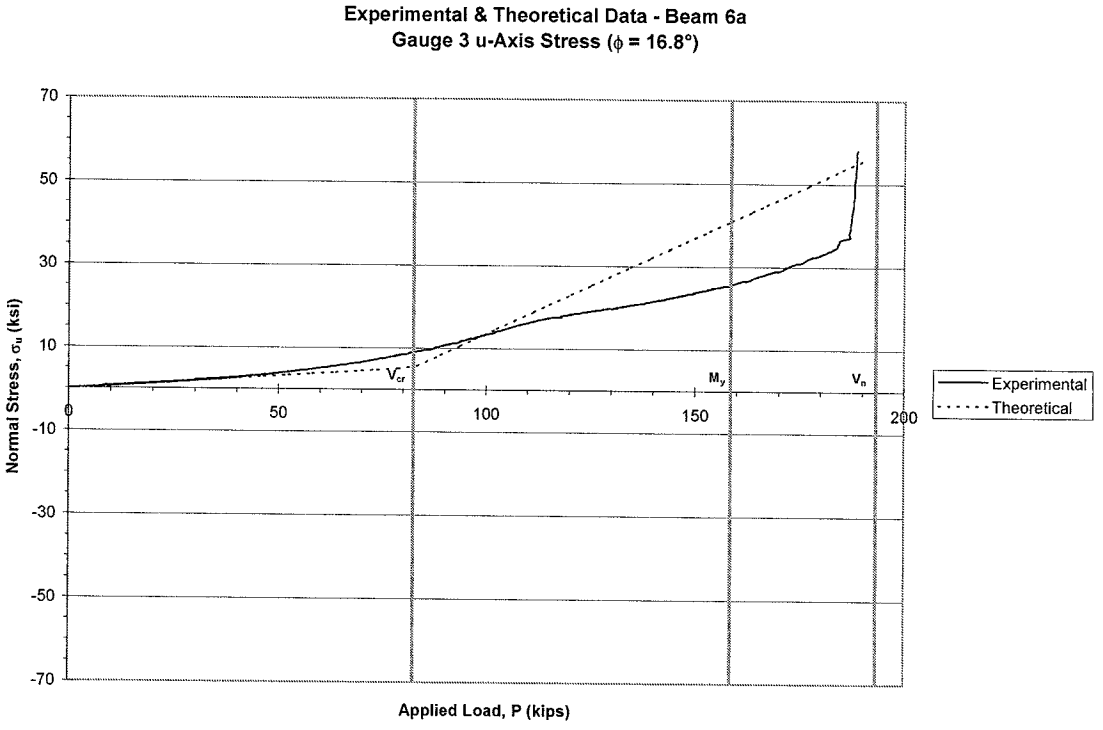

Figure 4-32. u-axis Normal Stress for $\phi = 16.8°$

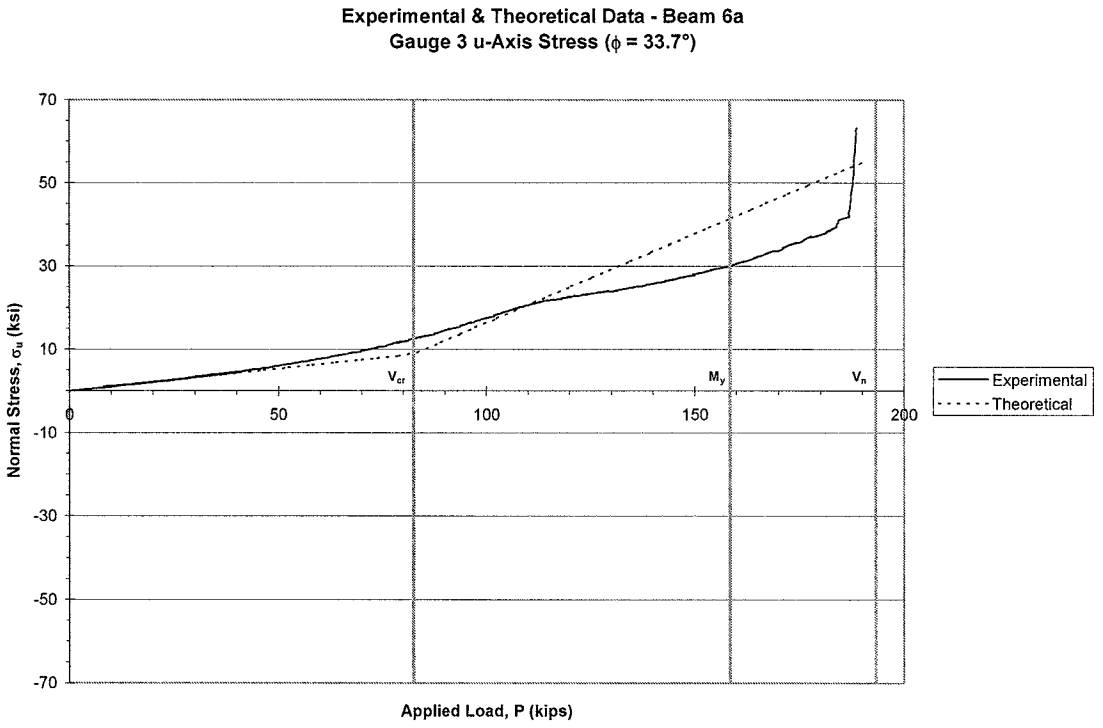

Figure 4-33. u-axis Normal Stress for $\phi = 33.7°$

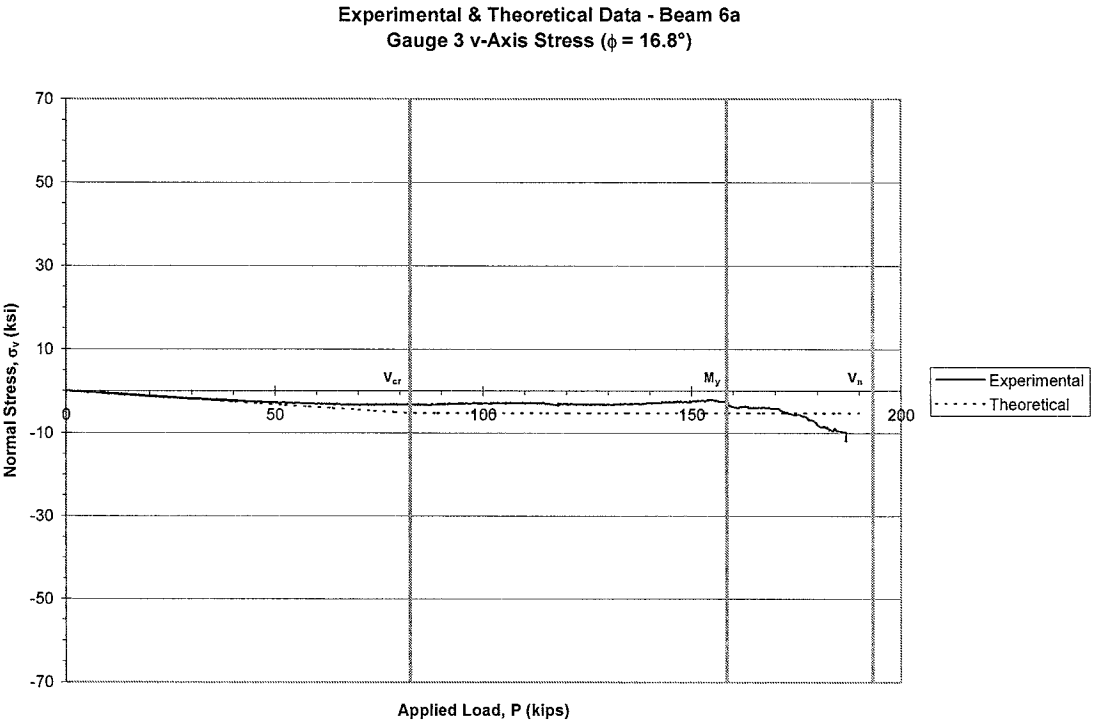

Figure 4-34. v-axis Normal Stress for $\phi = 16.8°$

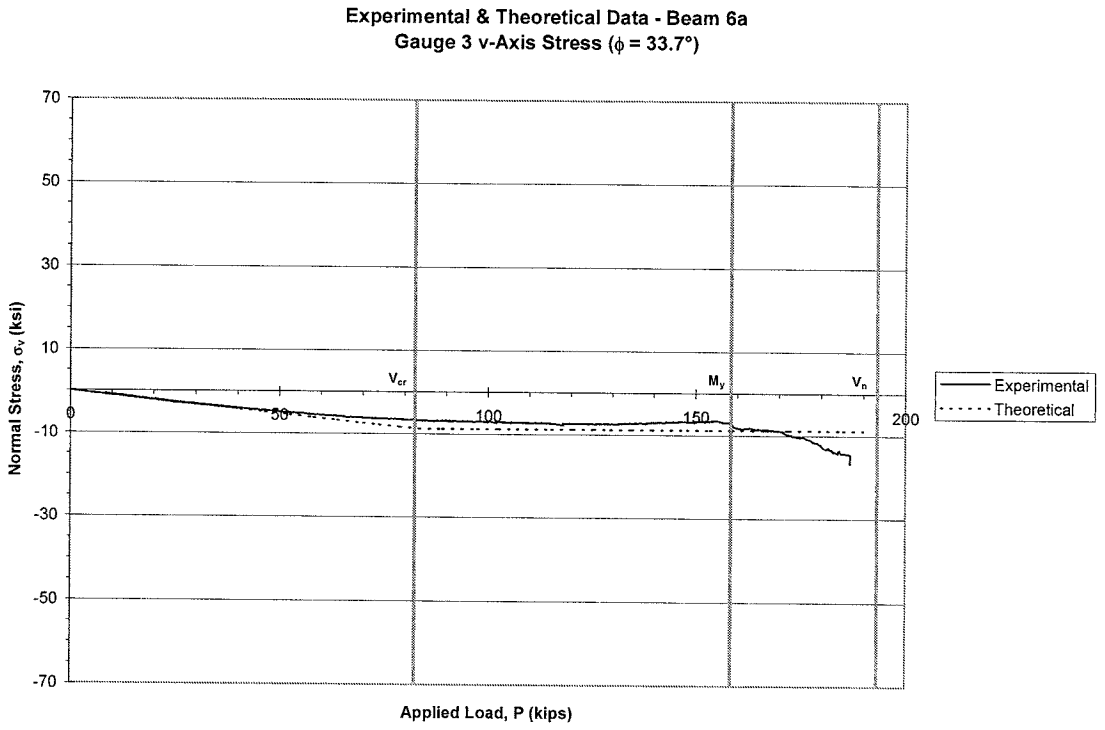

Figure 4-35. v-axis Normal Stress for $\phi = 33.7°$

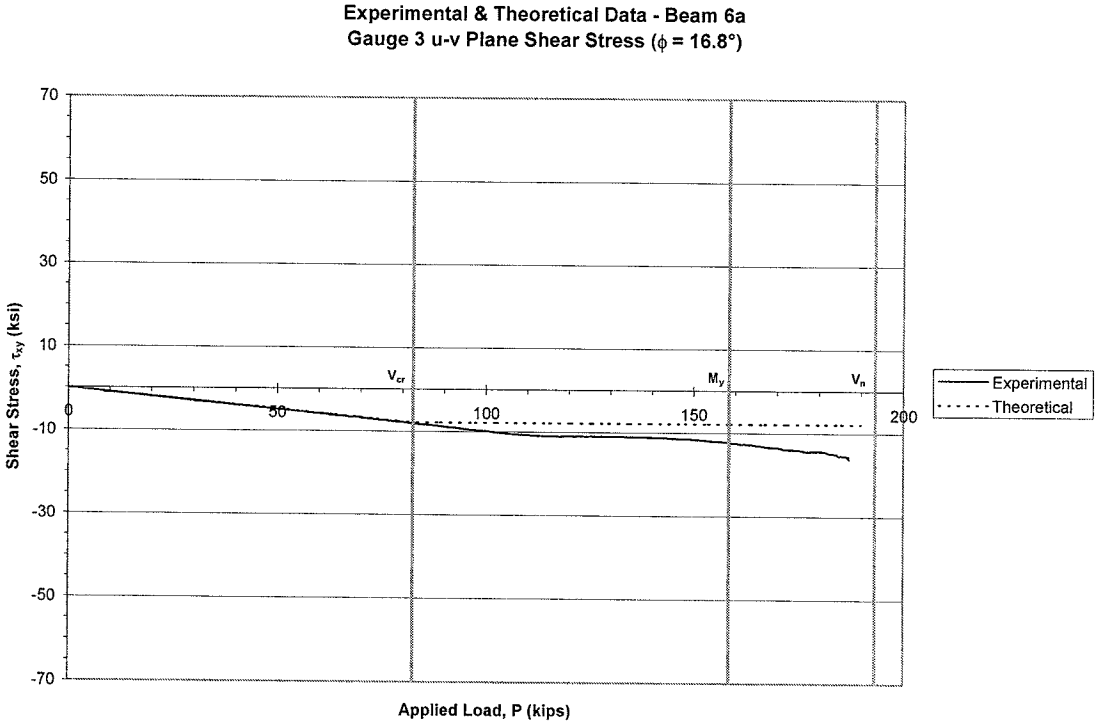

Figure 4-36. u-v Plane Shear Stress for $\phi = 16.8°$

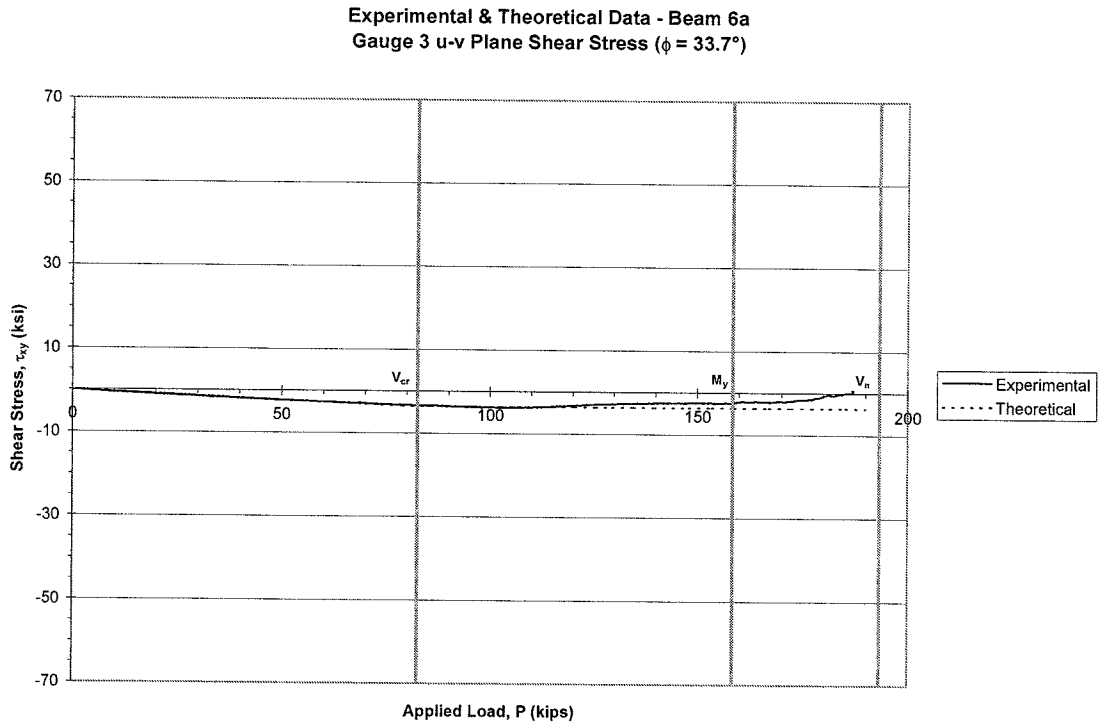

Figure 4-37. u-v Plane Shear Stress for $\phi = 33.7°$

From the u-v plane stress data, it appears that the experimental data matches the theoretical data reasonably well. As expected, the transition from beam action to tension field action is more gradual for the experimental data than the theoretical data. Also, the experimental data appears to more closely resemble the theoretical data for $\phi = 33.7°$. This is especially true for the shear stress on the u-v plane, which was used to determine the experimental web buckling load in Section 4.2.4. Data from Results Volume Chapter J (Zentz 2002) gives similar results.

Next, principal stresses can be easily calculated from the u-v plane stresses above and plotted against theoretical values. More importantly, the inclination of the principal plane can also be computed and compared to theory. Since an element located at the neutral axis is theoretically subject to pure shear prior to buckling, the inclination of the

principal plane for this element should theoretically be 45° from the horizontal (x-axis). As tension field stresses become more prominent, the inclination of the principal plane should asymptotically approach the angle at which the tension field stresses are acting. This should verify the angle at which tension field stresses act. Figure 4-38 through Figure 4-43 compare the principal stresses and angles for $\phi = 16.8°$ and $\phi = 33.7°$. Similar data for all test girders can be found in Results Volume Chapter K (Zentz 2002).

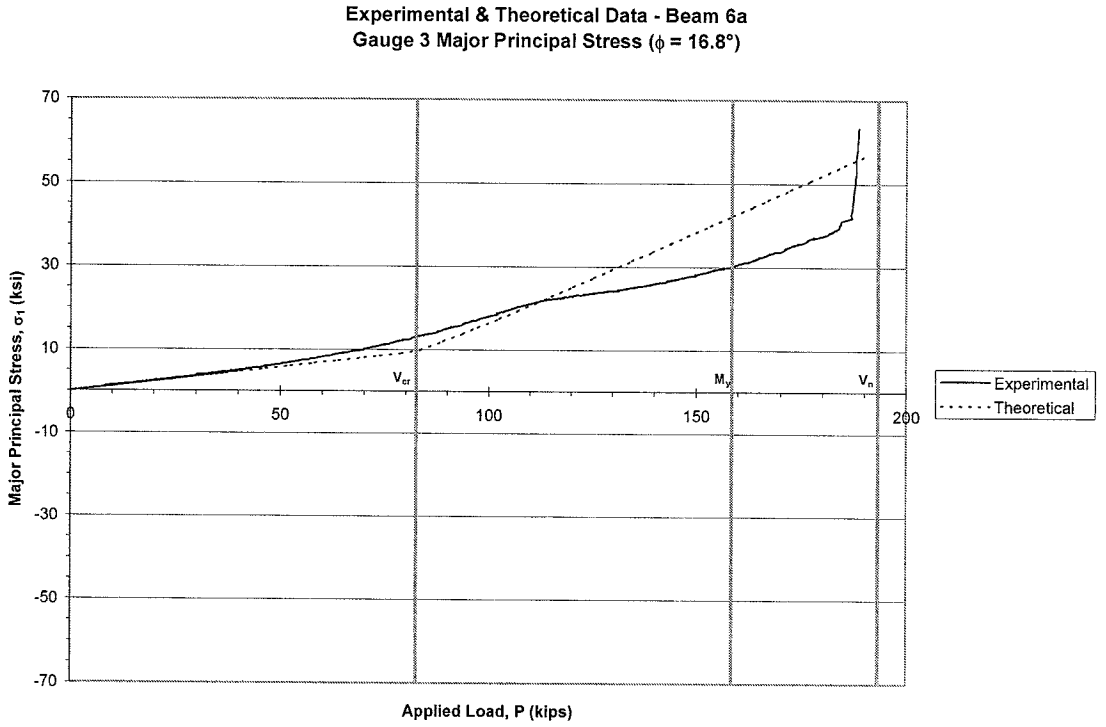

Figure 4-38. Major Principal Stress for $\phi = 16.8°$

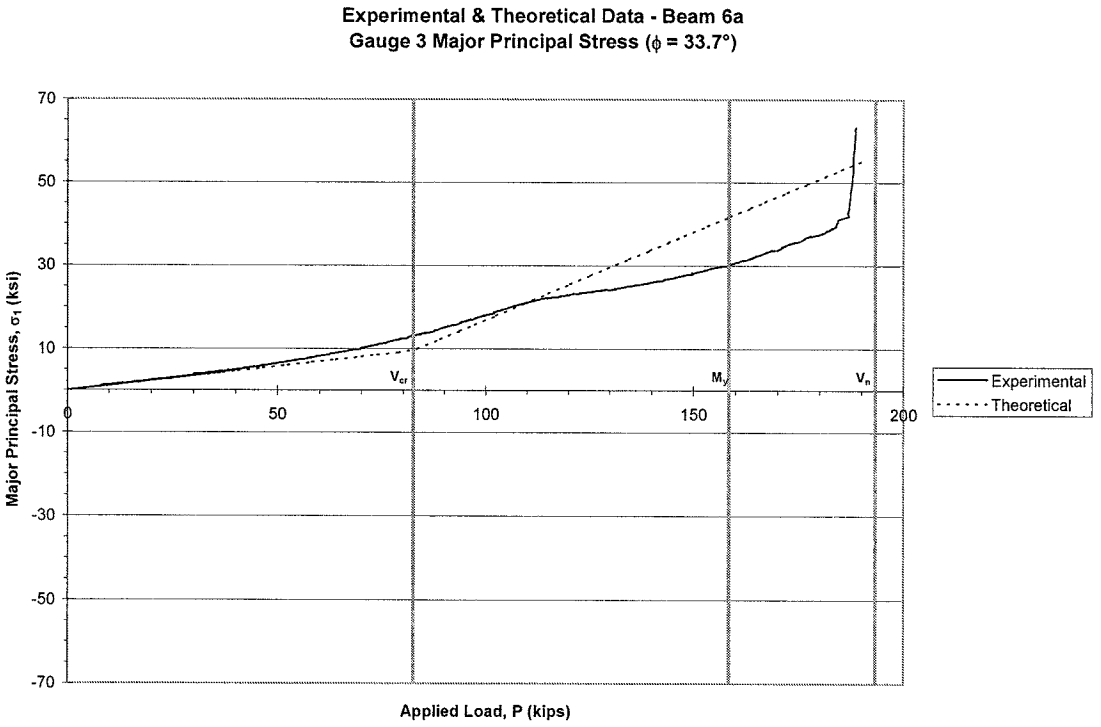

Figure 4-39. Major Principal Stress for $\phi = 33.7°$

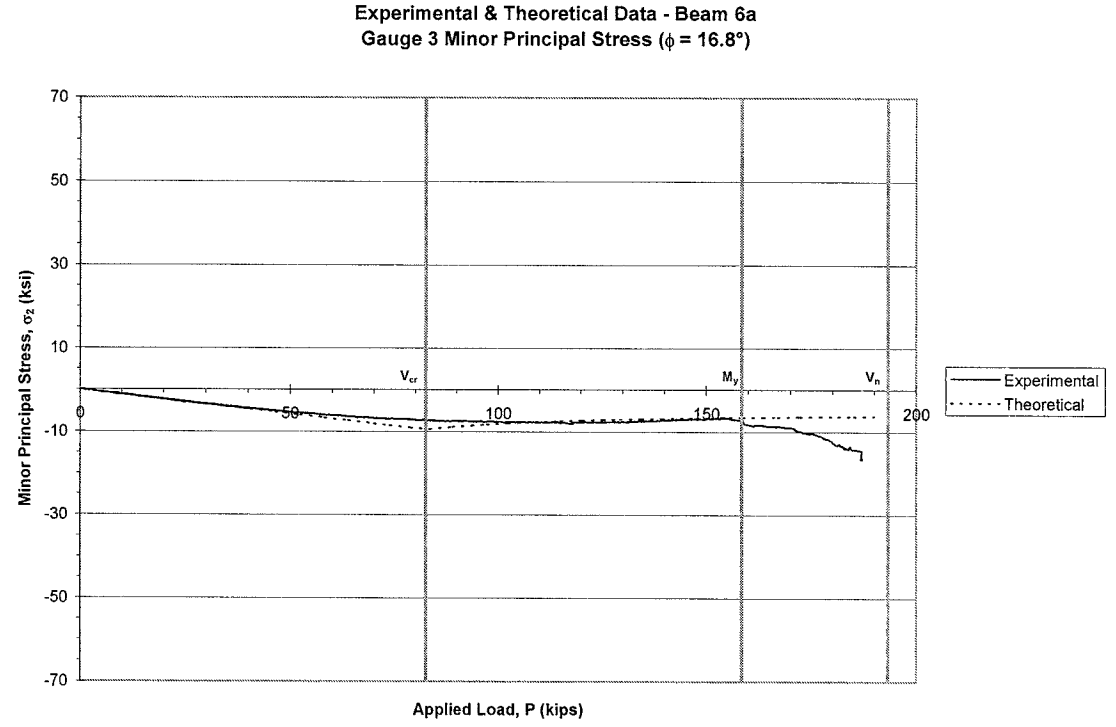

Figure 4-40. Minor Principal Stress for $\phi = 16.8°$

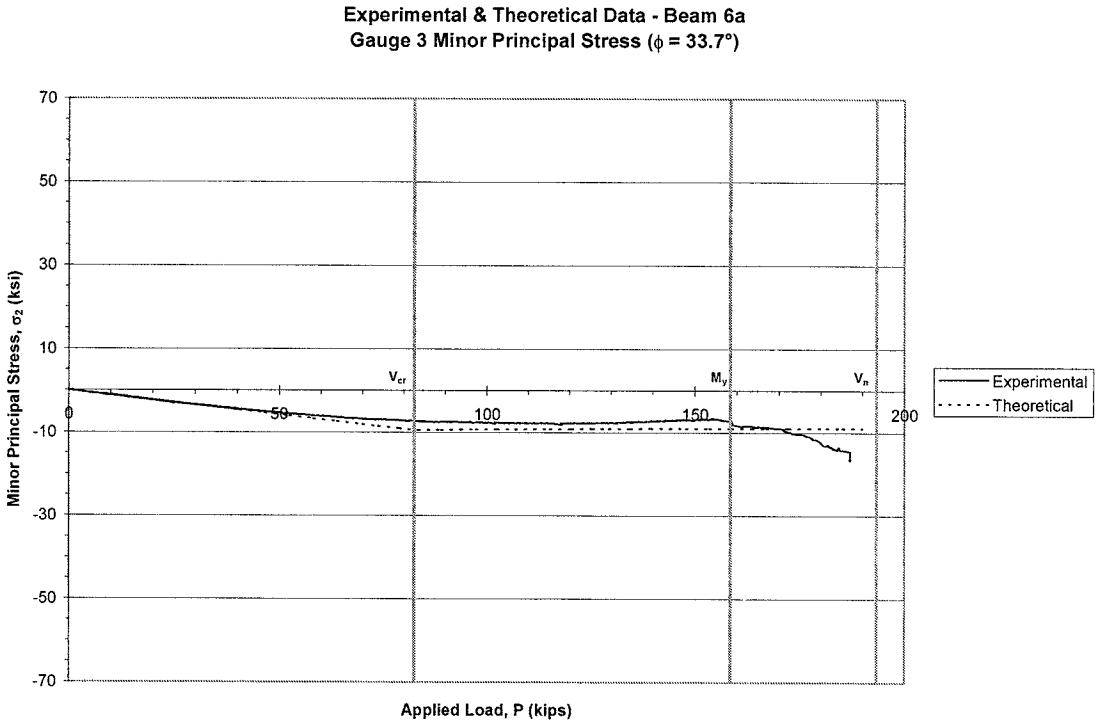

Figure 4-41. Minor Principal Stress for ϕ = 33.7°

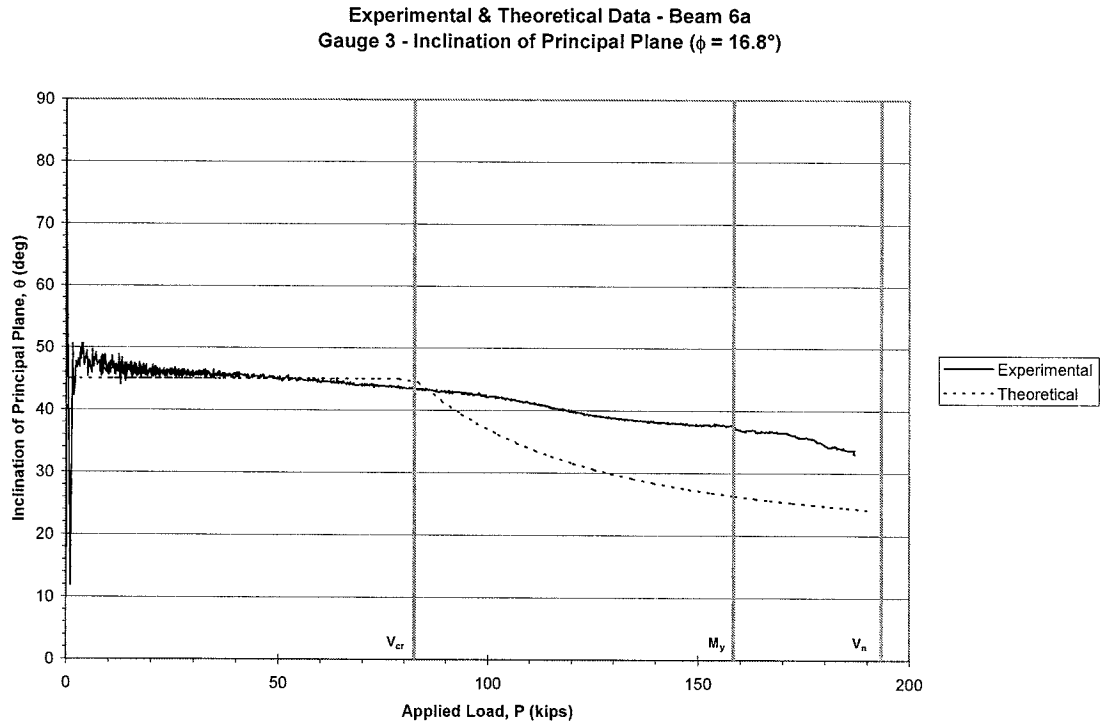

Figure 4-42. Orientation of Principal Plane for ϕ = 16.8°

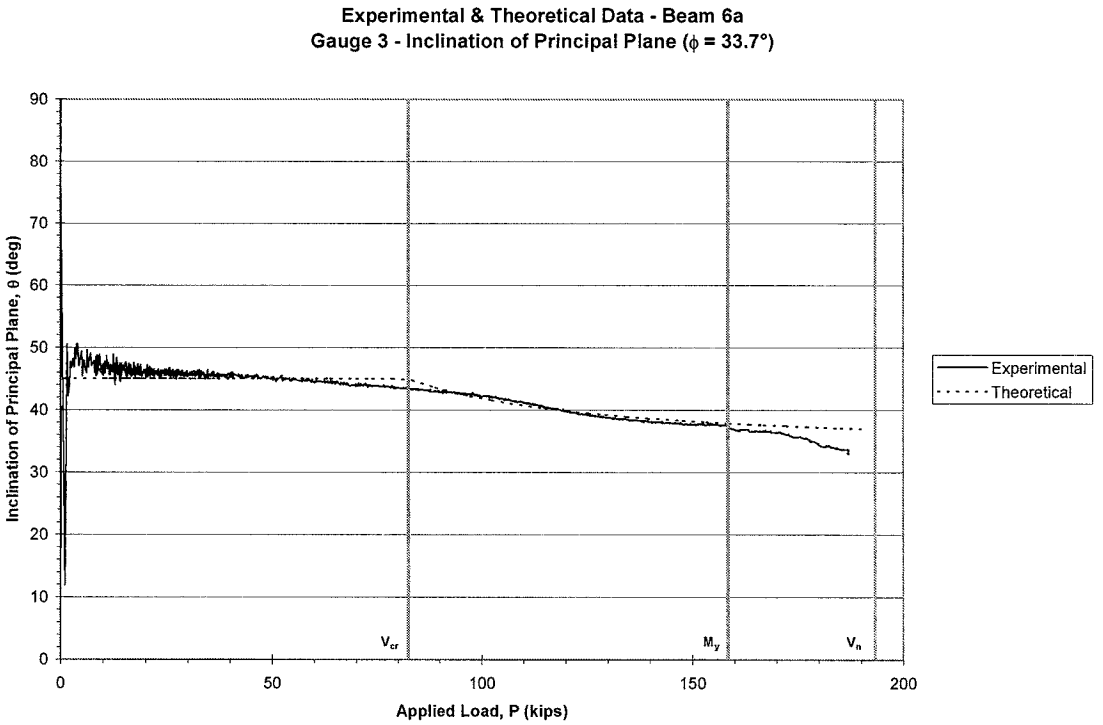

Figure 4-43. Orientation of Principal Plane for $\phi = 33.7°$

There is very little difference in the theoretical principal stress data for $\phi = 16.8°$ and $\phi = 33.7°$, so the experimental data matches reasonably well with both sets. The important point of the principal stress data is the orientation of the principal plane. The inclination of the principal plane should start at 45° for an element at the neutral axis and then it should approach the angle of tension field stresses as they become more pronounced at higher load levels. The experimental data begins at about 48° and approaches 34° just prior to failure. For this reason, it appears that the inclination of the u-v plane is equal to the angle of the panel diagonal (33.7°) at the failure state, since the u-v plane is defined as the plane on which tension field stresses are applied to obtain the

failure state of stress from the buckling state of stress. This also implies that the u-v plane is concurrent with the principal plane at failure for an element at the neutral axis. This is logical, since at failure, the tension field stresses are at a maximum and would tend to dominate the state of stress at the neutral axis where there are no flexural stresses with which to interact. Data from other tests resulting in shear failures, given in Results Volume Chapter K (Zentz 2002), generally support these findings. Moment failures do not fully develop the tension field stresses, so the orientation of the principal plane does not reach the angle of the panel diagonal, but the principal plane does shift toward the panel diagonal at low load levels.

Using Mohr's circle to display the state of stress at a discrete load levels, the development of stresses on all planes can be observed. Since only the buckling and failure states are theoretically defined, it is not possible to compare experimental data to theory at every load level. Rather, the development of stresses can be observed as the experimental Mohr's circle develops from the theoretical buckling to the theoretical failure state. The development of experimental stresses at the center of the test panel for Beam 6a from initial loading through the theoretical buckling and failure states is shown in Figure 4-44 through Figure 4-59. Due to the findings from the principal stress data, the Mohr's circle data is only shown for $\phi = 33.7°$. Mohr's circle data for other test girders is given in Results Volume Chapter L (Zentz 2002).

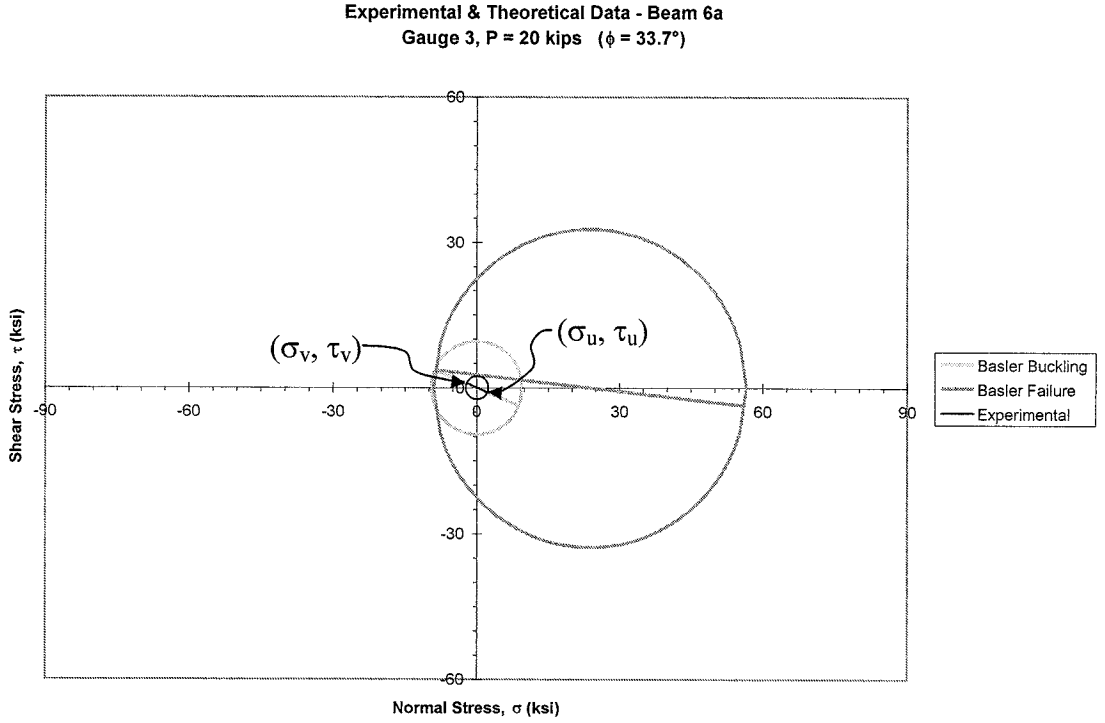

Figure 4-44. Mohr's Circle at 20 kip Applied Load

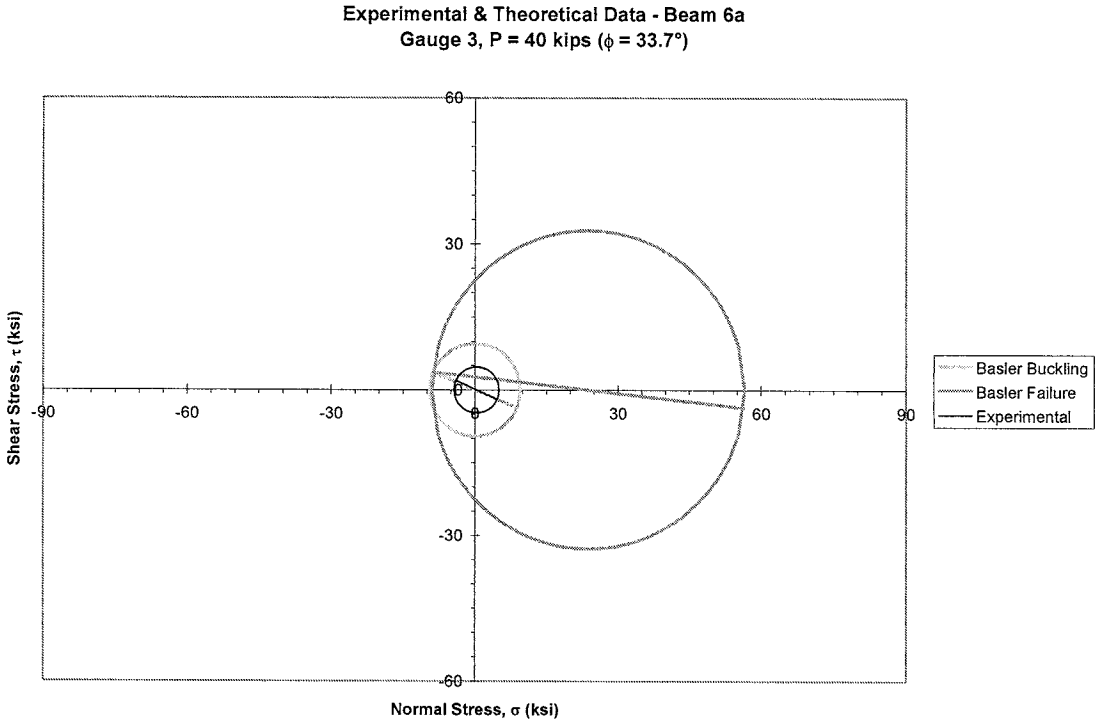

Figure 4-45. Mohr's Circle at 40 kip Applied Load

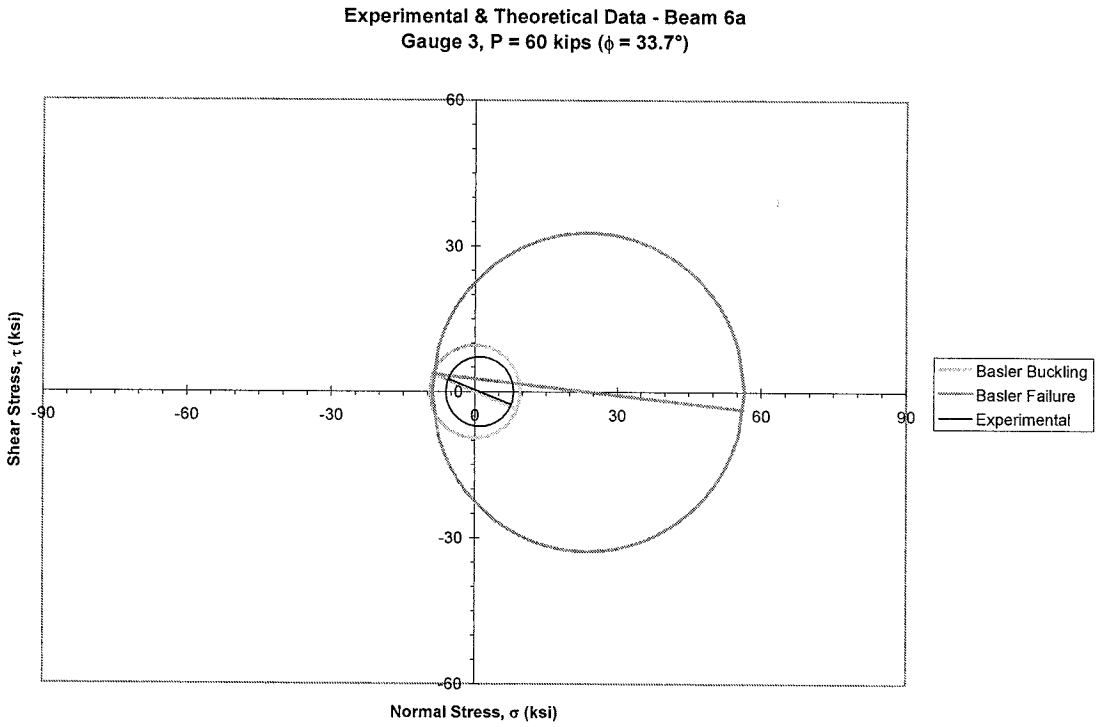

Figure 4-46. Mohr's Circle at 60 kip Applied Load

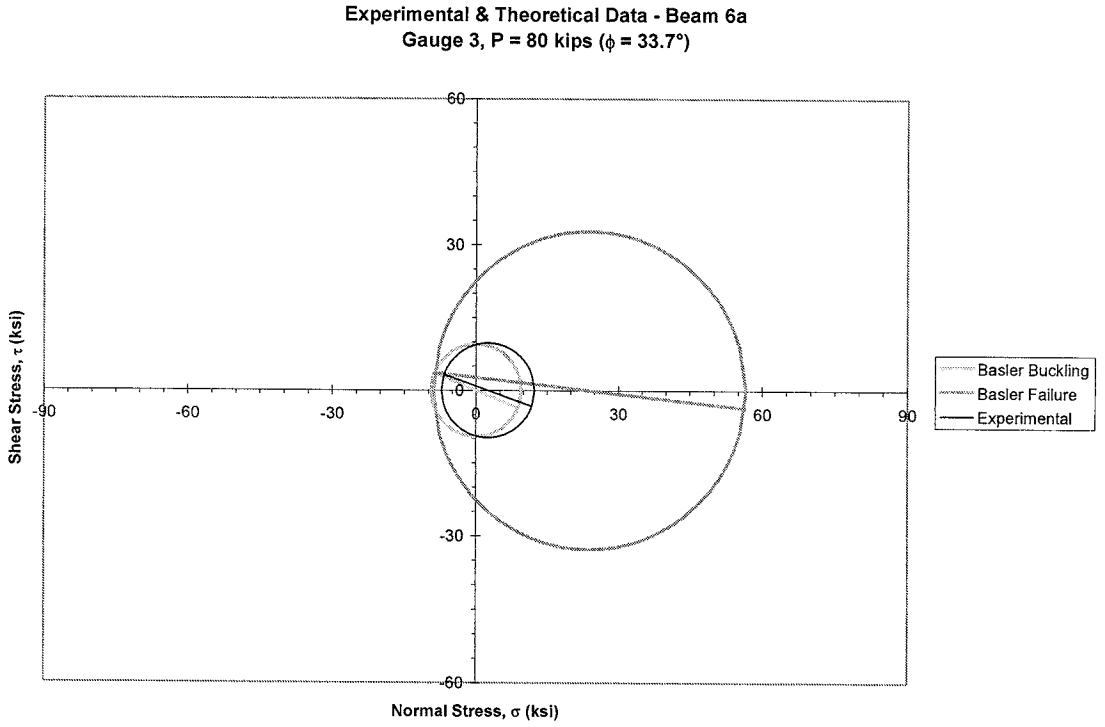

Figure 4-47. Mohr's Circle at 80 kip Applied Load

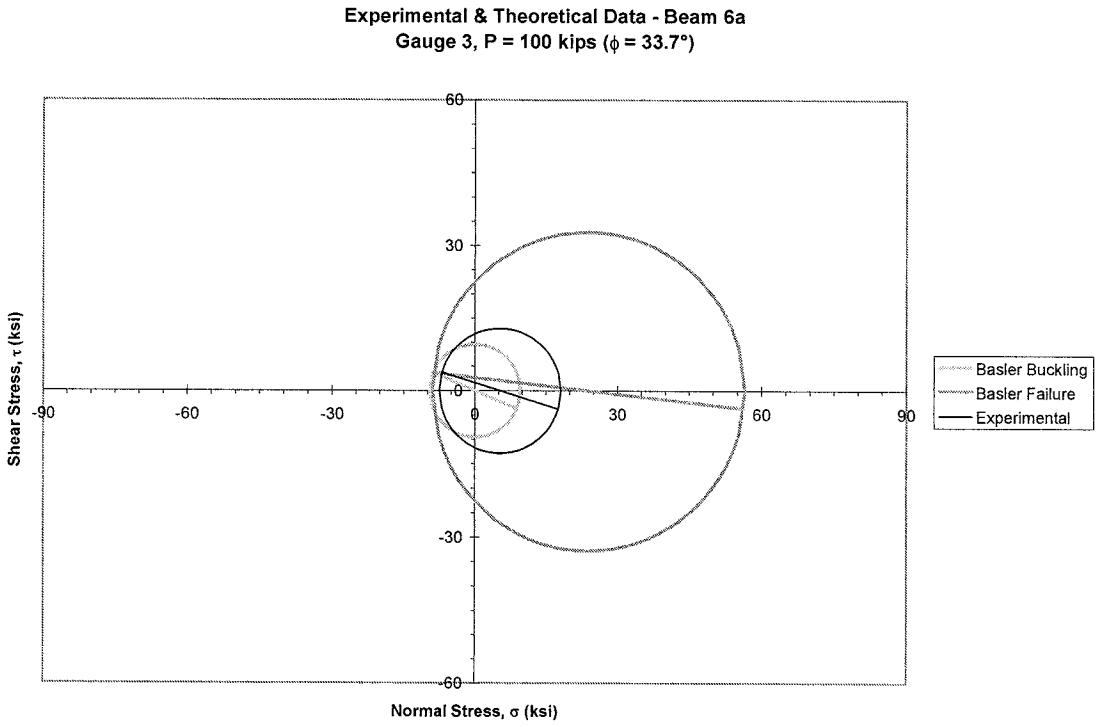

Figure 4-48. Mohr's Circle at 100 kip Applied Load

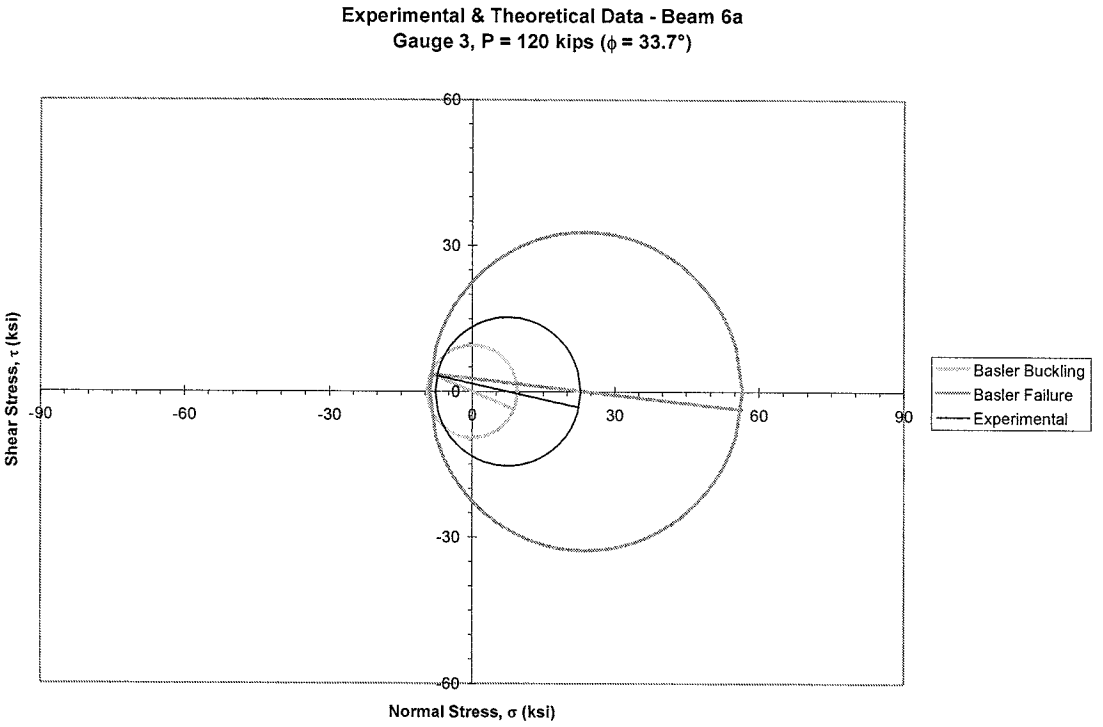

Figure 4-49. Mohr's Circle at 120 kip Applied Load

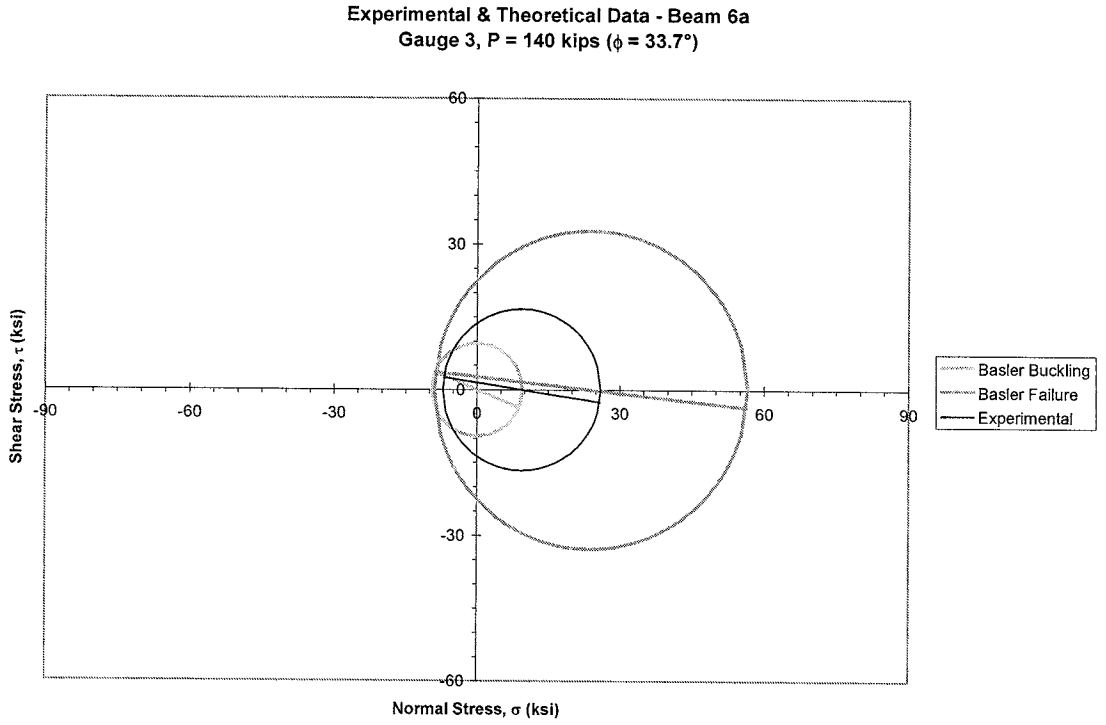

Figure 4-50. Mohr's Circle at 140 kip Applied Load

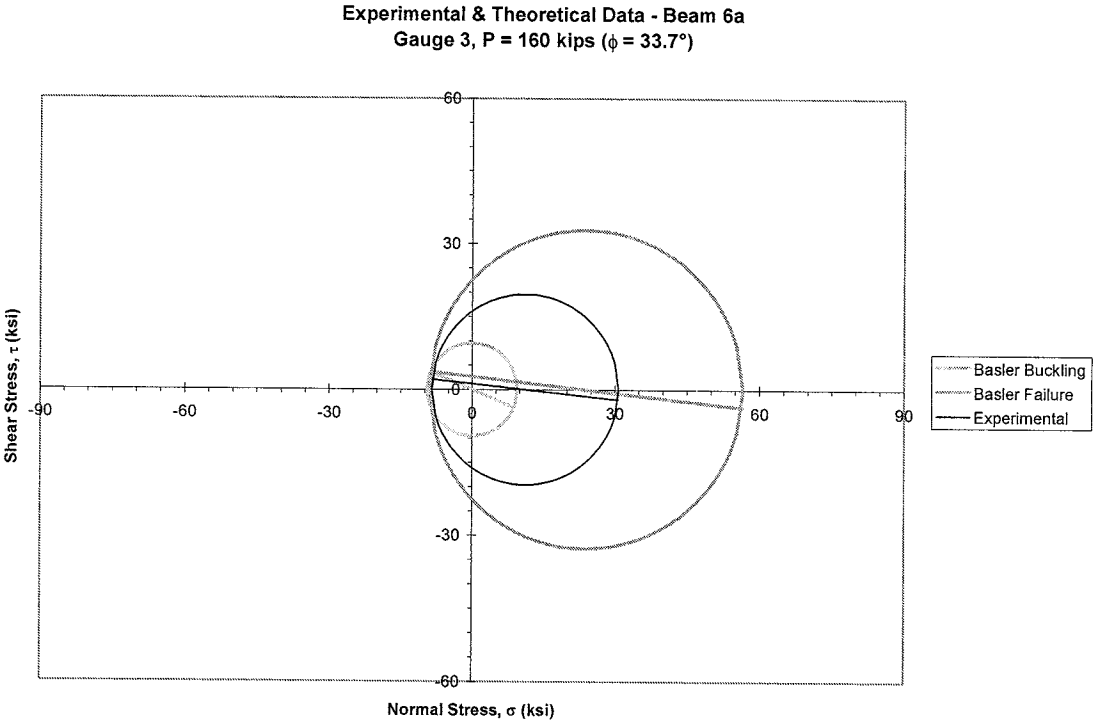

Figure 4-51. Mohr's Circle at 160 kip Applied Load

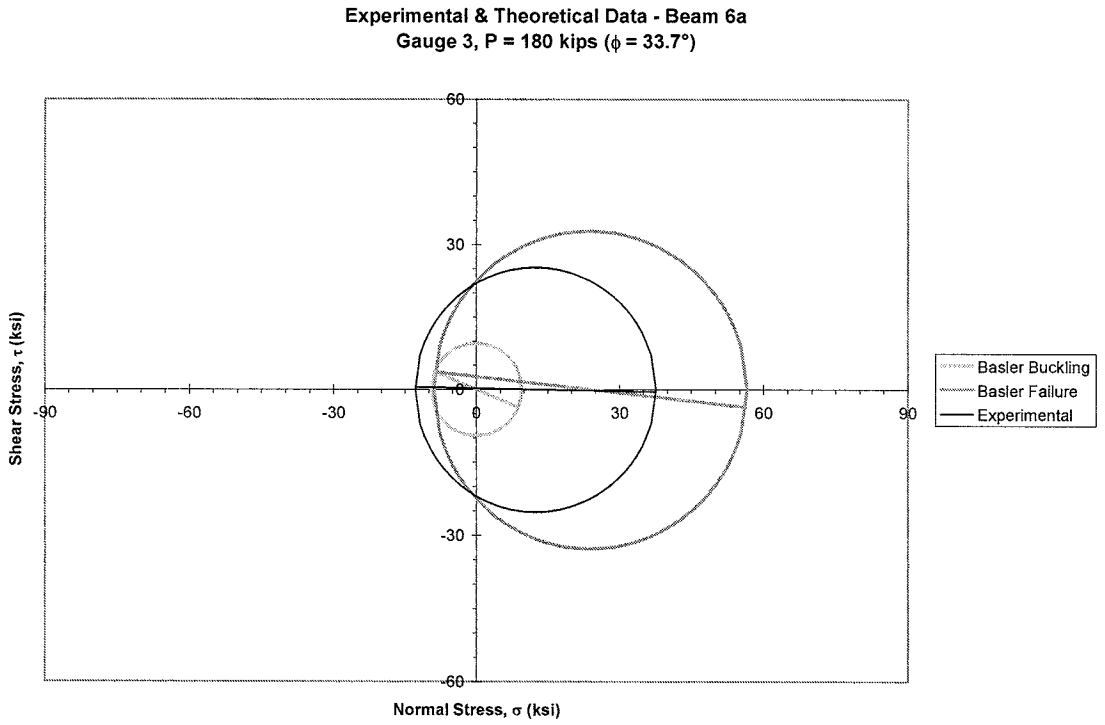

Figure 4-53. Mohr's Circle at 180 kip Applied Load

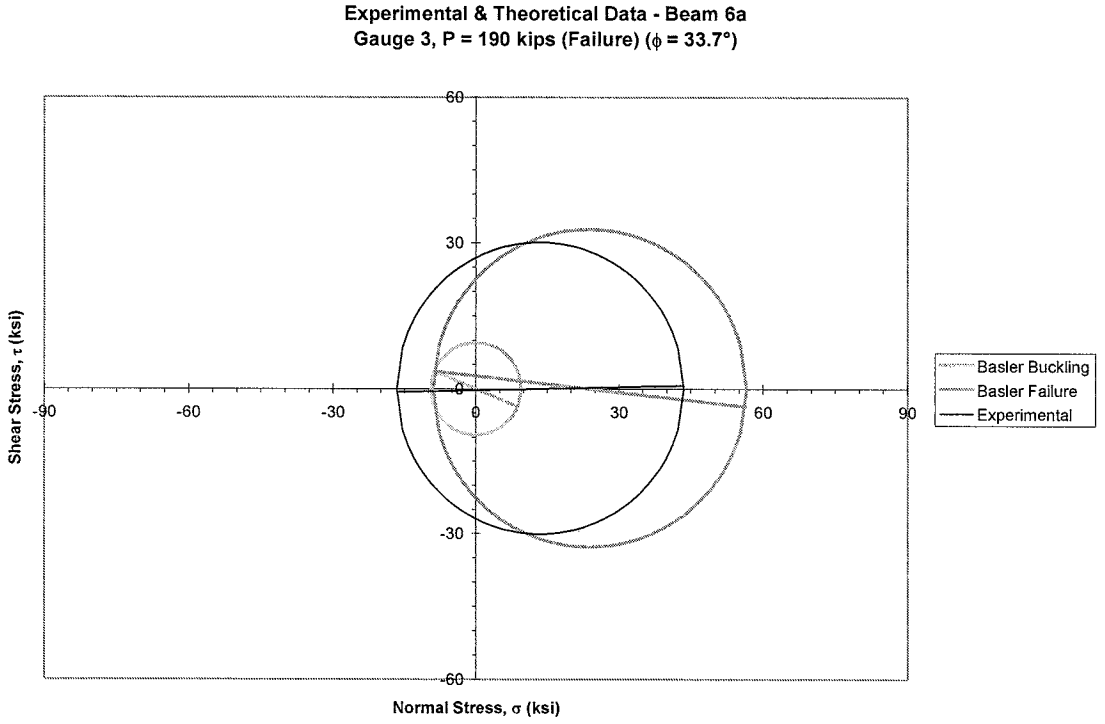

Figure 4-52. Mohr's Circle at 190 kip Applied Load (Failure)

The experimental Mohr's circle data agrees reasonably well with Basler's tension field action theory using $\phi = 33.7°$. Note that the experimental v-axis state of stress increases with applied load until it is nearly concurrent with the Basler buckling state of stress, and then remains stationary, consistent with Basler's theory. Also notice that the u-v plane approaches the principal plane as the girder nears failure. Data from other test girders displays similar results (see Results Volume Chapter L (Zentz 2002)).

As with elastic stresses, the flexural stress distribution can also be a useful display tool for postbuckling stresses. Even though it is qualitative, the flexural stress distribution is useful for demonstrating the effect of tension field action stresses on the cross section. With more gauge locations, it would also be possible to measure the experimental tension field bandwidth as the tension field develops. However, with only a few gauge locations as in the Series II tests, the bandwidth cannot be measured, but the effects of the tension field on the flexural stress distribution can be visualized. Figure 4-54 through Figure 4-59 show development of flexural stresses from an applied load of 100 kips through failure. Refer to Section 4.3 for flexural stress data at lower levels of applied load. Complete flexural stress data for all tests is given in Results Volume Chapter I (Zentz 2002).

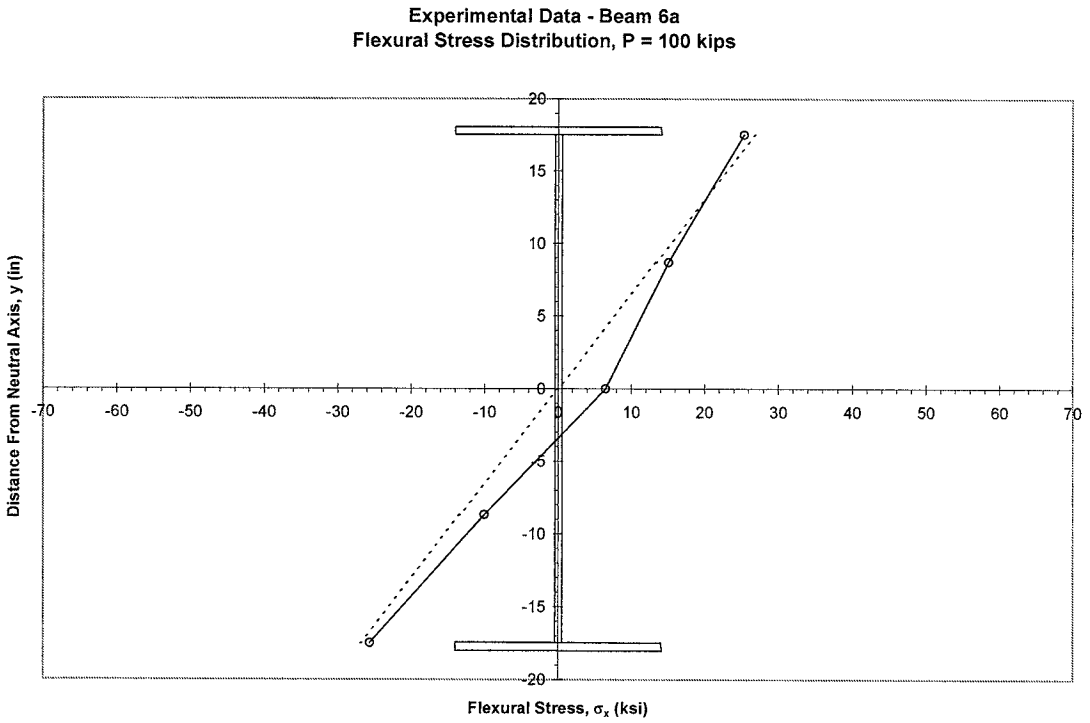

Figure 4-54. Flexural Stress Distribution for 100 kip Applied Load

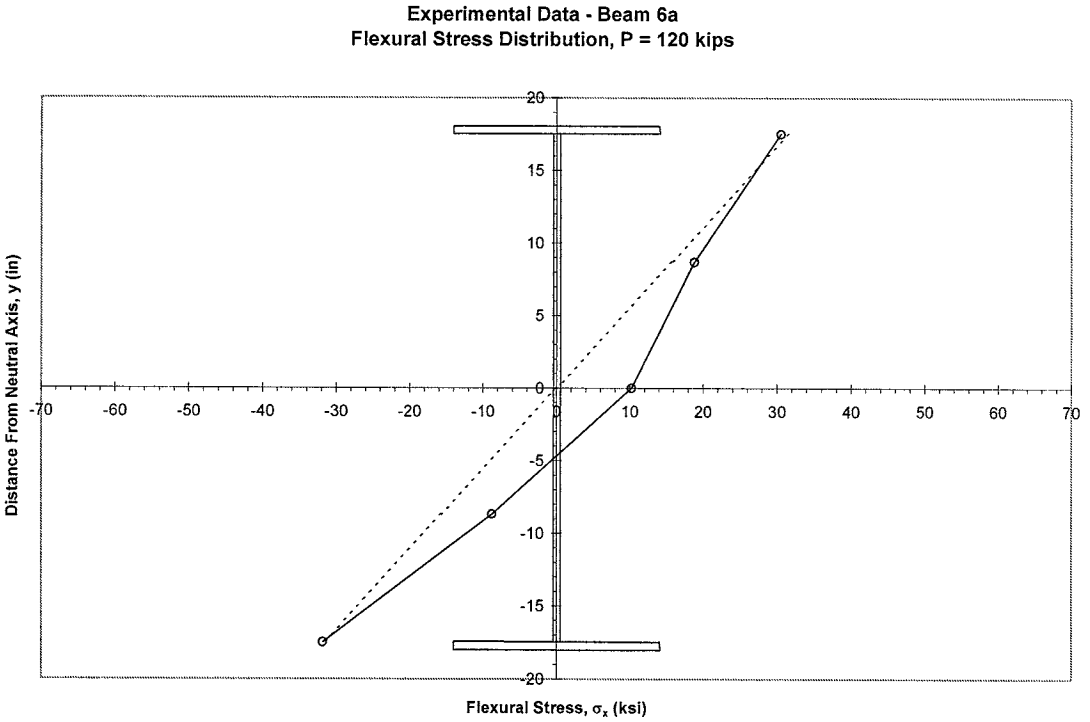

Figure 4-55. Flexural Stress Distribution for 120 kip Applied Load

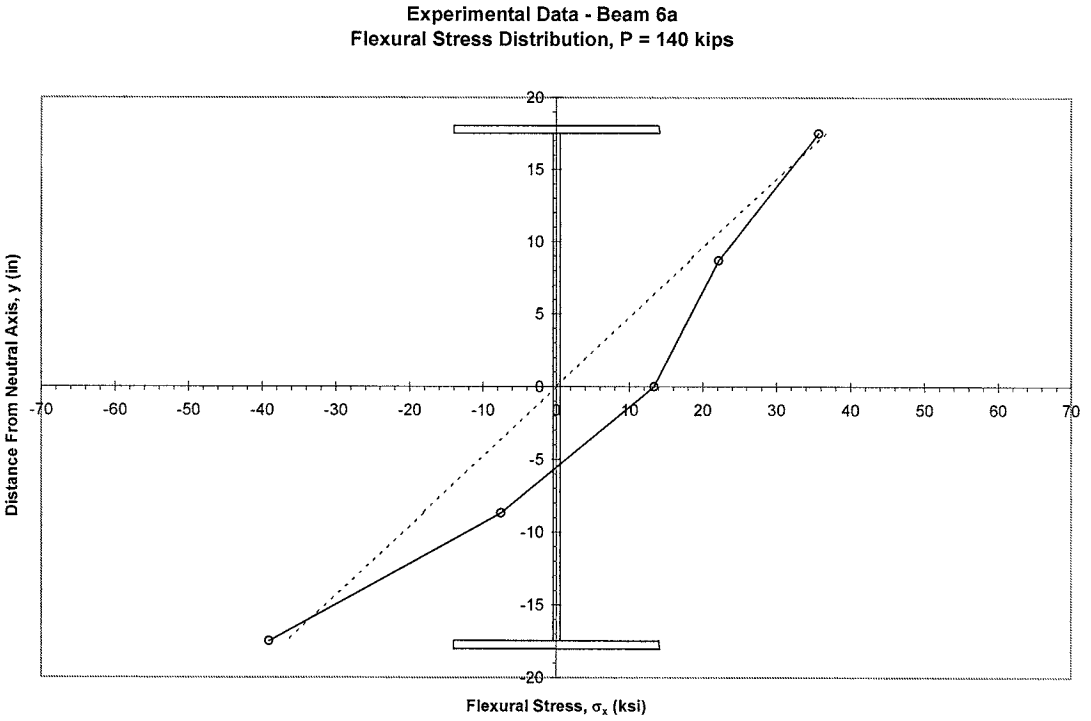

Figure 4-56. Flexural Stress Distribution for 140 kip Applied Load

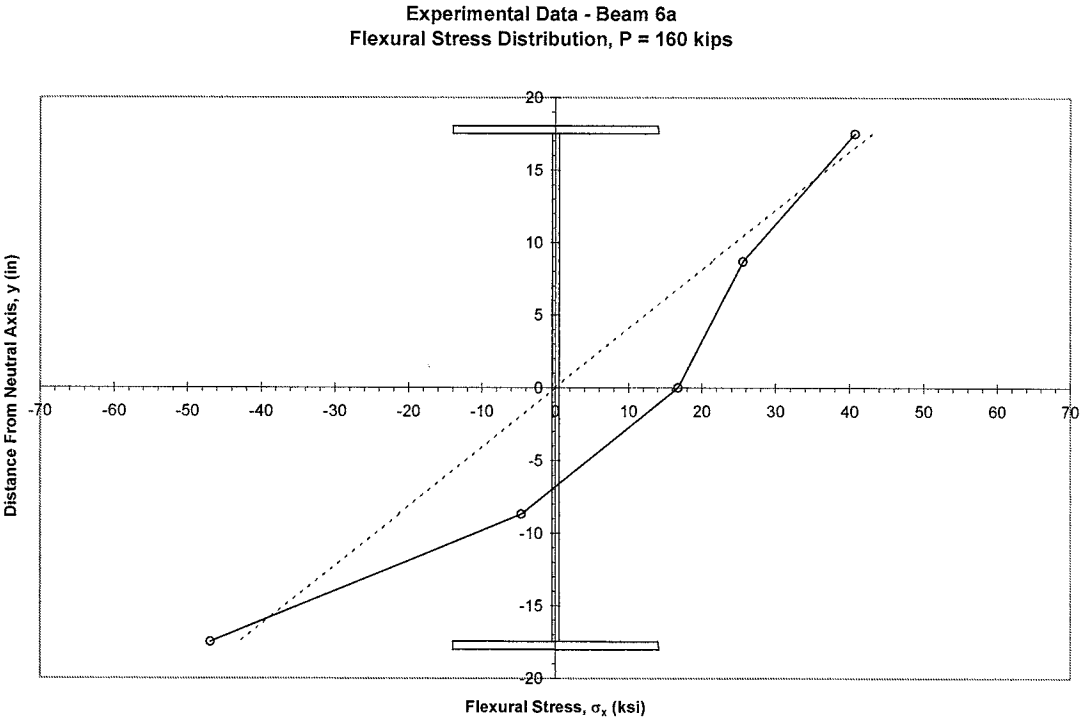

Figure 4-57. Flexural Stress Distribution for 160 kip Applied Load

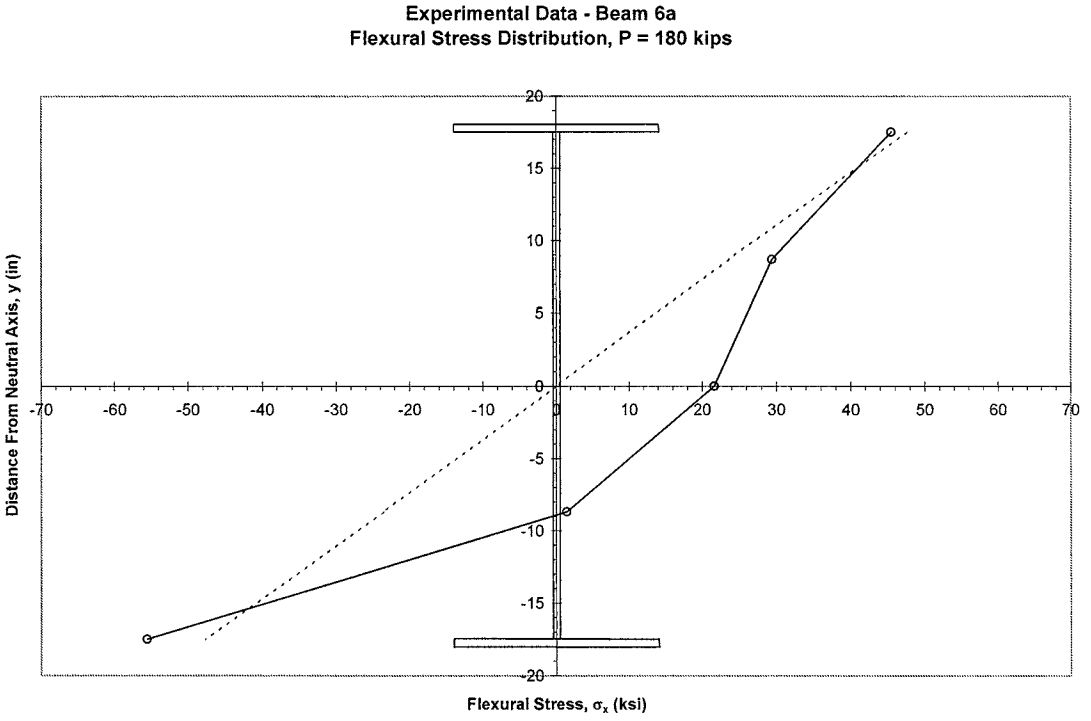

Figure 4-58. Flexural Stress Distribution for 180 kip Applied Load

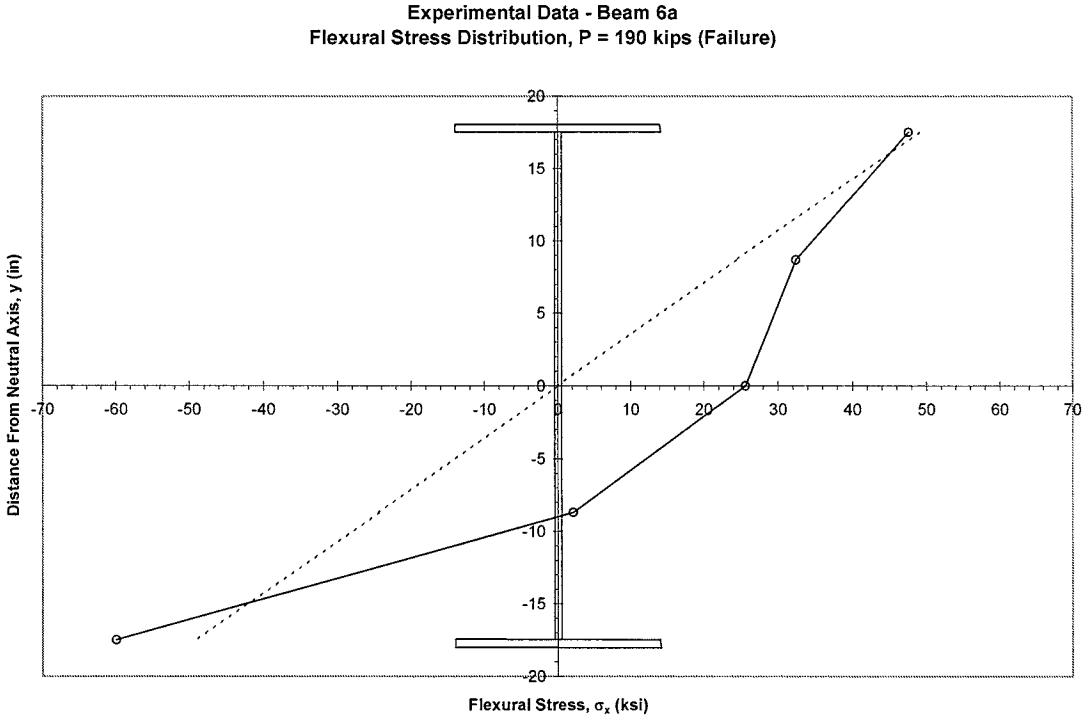

Figure 4-59. Flexural Stress Distribution for 190 kip Applied Load (Failure)

For a qualitative comparison, it is assumed that the flexural stress effects from beam and tension field action can be superimposed. As shown in Figure 4-60, the linear flexural stress distribution is added to the x-axis component of Basler's assumed tension field, resulting in the flexural stress distribution shown. Given the few data points available for the Series II tests, the theoretical distribution resembles the experimental distribution as the girder nears failure.

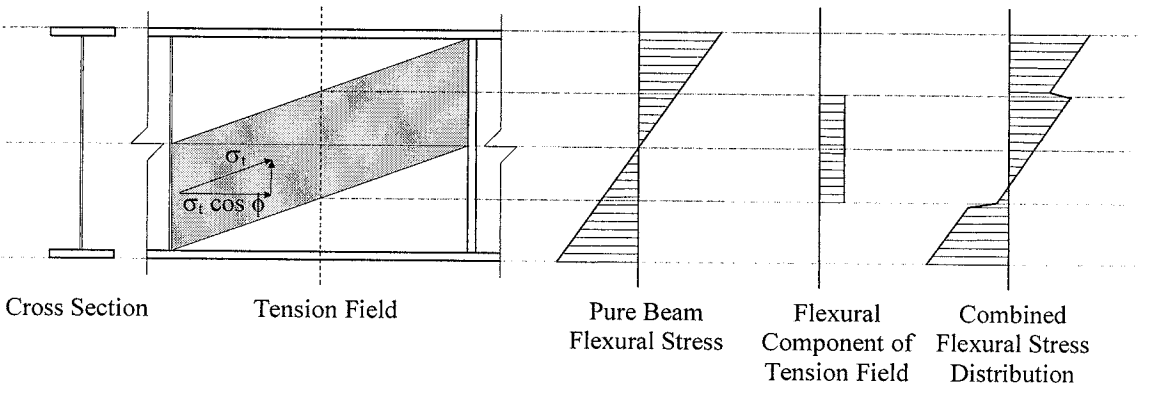

Figure 4-60. Theoretical Flexural Stress Distribution from Superposition

Experimental data including u-v plane stresses, principal stresses, Mohr's circles, and flexural stress distributions have been used to verify the postbuckling stresses in the Series II test girders. The stresses generally correspond reasonably well with Basler's tension field action theory, with the exception that the angle of inclination of the u-v plane was found to be equal to the diagonal angle of the shear panel.

4.5 Impact of TFA in Hybrid Girders

Goessling (2002) examined the impact of allowing tension field action and eliminating the moment-shear interaction reduction on a suite of typical steel girder bridges. She designed 16 bridges and determined the number of intermediate shear stiffeners required for various bridge configurations (Table 4-4). The spans varied between two and three with two different span length combinations each. She considered girder spacing in terms of number of girders, and web slenderness ratios.

Table 4-4. Stifffener Design Using TFA in Hybrid Girder Bridges

Bridge	# of Girders	50 ksi Steel	HPS70W Steel	D/tw	No TFA	TFA	# of Stiffeners saved	% Saved	$ Saved
2 Span		tons	tons		# Stiffeners	# Stiffeners	using TFA	using TFA	$200 per stiffener
120'-120'	7	186.2		120.9	42	28	14	33.3%	$2,800
		175.2		140	126	70	56	44.4%	$11,200
	8	183.1		120	80	48	32	40.0%	$6,400
		194		140.4	112	80	32	28.6%	$6,400
160'-160'	7	290.7		120	42	28	14	33.3%	$2,800
		284		140.4	126	84	42	33.3%	$8,400
	8	327.8		120	32	32	0	0.0%	$0
		319.3		140.4	112	64	48	42.9%	$9,600
3 Span									
120'-150'-120'	7	608.2		120.9	84	56	28	33.3%	$5,600
		578		140	238	112	126	52.9%	$25,200
	8	607.5		120	144	112	32	22.2%	$6,400
		648.1		140	192	128	64	33.3%	$12,800
160'-200'-160'	7	1100.6		120.7	56	28	28	50.0%	$5,600
		1075.9		140.8	154	42	112	72.7%	$22,400
	8	1105.1		120	64	64	0	0.0%	$0
		1069.7		140.4	224	64	160	71.4%	$32,000

Goessling compares the total number of stiffeners required, including bearing stiffeners, for restricting the hybrid designs to the shear buckling capacity (no TFA) with the reduced number required if TFA is allowed without a reduction for moment-shear interaction. She assumes a stiffener cost of $200 per stiffener to arrive at a total savings. In addition to fewer details and a more consistent design, the savings can be significant.

4.6 Summary

The objective of this chapter was to determine the experimental tension field action shear capacity of the Series II hybrid plate girders, verify that the capacity is indeed due to tension field action stresses, and compare the results to theoretical values from Basler's tension field action theory. Through physical observation of the Series II tests, the ultimate shear capacity and interaction characteristics of the test girders were investigated, and the tension field action contribution to shear resistance was quantified. The data taken from the tests was used to verify both the elastic and postbuckling stresses present in the test girders in order to verify the presence of tension field action.

The experimental tension field action shear capacities of the Series II test girders have been determined and the tension field stresses have been verified. The ultimate shear capacities of the hybrid test girders were found to be accurately predicted by AASHTO's current design equations for homogenous sections, neglecting moment-shear interaction reductions. There was no evidence of significant moment-shear interaction that would require reducing the shear capacity as is currently prescribed in AASHTO. The stress patterns present in the test girders correspond well with Basler's tension field action theory, with the exceptions that the angle of inclination of the u-v plane was found to be equal to the diagonal angle of the shear panel, and the transition from beam action to tension field action begins at low load levels and is more gradual than suggested by theory. The following chapter will draw conclusions based on the observations made from the experimental data.

Chapter 5 - Summary and Conclusions

5.1 Summary

High Performance Steel, in particular HPS70W, has been used in hundreds of bridges across the United States. A large percentage of these bridges have used the HPS in the form of hybrid girder designs. Bridge studies (Barker and Schrage 2000) have shown that the most beneficial use of HPS70W (70 ksi) is in the flanges of hybrid girders with 50 ksi webs. One limit with hybrid girder design, which decreases the beneficial aspects, is that tension field action (TFA) is not allowed when determining the shear capacity. This is a severe shear capacity penalty for using hybrid girders. Limiting hybrid shear capacities to the shear buckling capacity results in more transverse stiffeners required (closer spacing) for a hybrid girder than that for a homogeneous girder. This not only increases material costs, but significantly increases fabrication costs.

The objective of this research is to validate the tension field action behavior in hybrid plate girders. The goal is to allow TFA in hybrid girders resulting in more economical design of steel bridges.

The work conducted for this research covers several topics in tension field action and moment-shear interaction of plate girders. The first effort concentrated on the original shear capacity theoretical derivations (Basler 1961a) and the impact of using hybrid girders. Proposed theoretical lower bound shear capacity procedures were developed for moment-shear interaction that represent the equivalent AASHTO equations for hybrid girders (Barker et al 2002, Hurst 2000).

Two series of tests were designed (Hurst 2000) and tested to determine the hybrid girder shear capacity and study the tension field behavior of homogeneous and hybrid girders. Series I test specimens were homogeneous and hybrid girders tested under high shear and low moment conditions. Results from Series I testing are published in two separate theses (Schreiner 2001, Rush 2001). Series II test specimens were designed and tested to study the effect of moment-shear interaction. Results from Series II testing are published in two separate theses (Zentz 2002, Davis 2002). Finally, Goessling (2002) studied an array of practical bridge designs to study the impact of allowing TFA in hybrid girders.

This report includes a thorough presentation of tension field action and moment-shear interaction in plate girders, and in particular hybrid plate girders. It presents a comprehensive presentation on the Series II test girders with a detailed analysis and examination of the test behaviors. The report only uses the overall results of the Series I test girders.

In this Summary, there are a few important results that need to be presented clearly. Hybrid steel girders exhibit tension field action according to current AASHTO shear capacity provisions. Using the original moment-shear interaction derivations, this research has produced a theoretical lower-bound moment-shear interaction equation for hybrid girders that is equivalent to the current AASHTO moment-shear interaction requirement for homogeneous girders. However, the results of the experimental tests have also shown that there is no moment-shear interaction for these plate girders. Aydemir (2000) agrees after many finite element analyses of a parametric suite of plate girders. Table 5-1 summarizes the Series I and Series II test girder results. All of the

tests show that hybrid girders exhibit tension field action according to the current AASHTO specifications. Figure 5-1 shows the test results plotted against the AASHTO and proposed hybrid girder moment-shear interaction requirements. The girders all demonstrated that the capacities exceeded expectations and that a moment-shear interaction reduction is not necessary.

Table 5-1. Tension Field Action Experimental Results

BEAM		Test Girder	V/Vn	M/Mn	Theoretical Total Shear Capacity (kips)	Experimental Shear Capacity (kips)	Remarks (failure mode)
Series I	1	50-50	**1.07**	Low	193	205	Shear
	2	70-70	**>1.05**		208	>218	Shear
	3a	50-70	**1.10**		193	211	Shear
	3b	50-70	**1.08**		193	207	Shear
Series II	4	50-70	**1.04**	0.79	193	201	Shear
	5	50-70	0.78	**1.05**	193	151	Moment
	6a	50-70	**0.98**	0.93	193	190	Shear
	6b	50-70	**0.99**	0.93	193	191	Shear
	7	50-70	0.45	1.04	193	86	Moment
	8	50-50	**0.95**	**1.16**	193	183	Mom/Shear

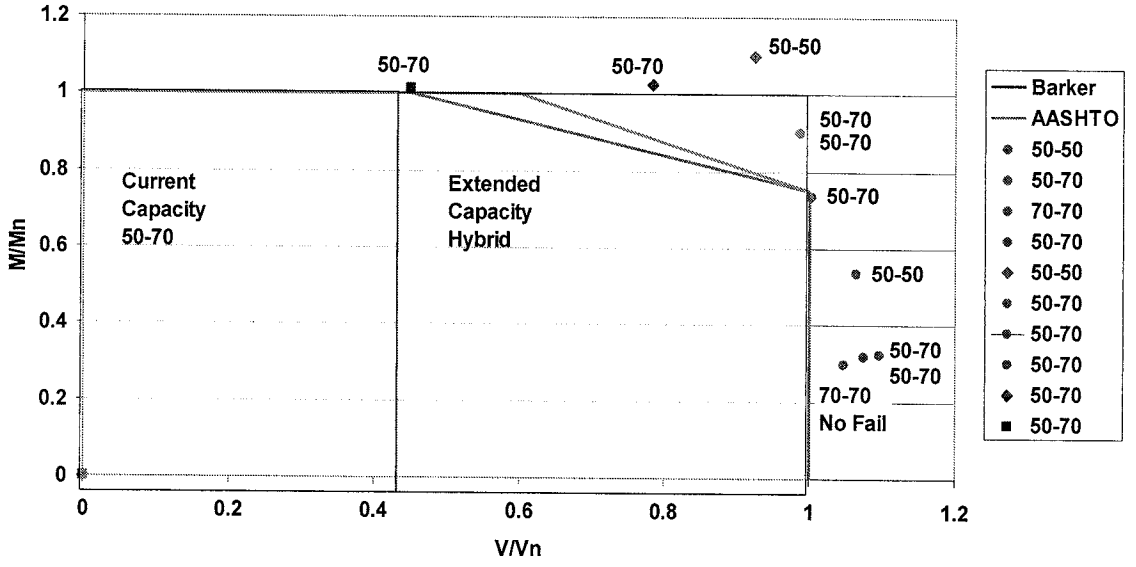

Figure 5-1. Test Results Compared to AASHTO & Proposed Moment-Shear Interactions

5.2 Project Conclusions and Recommendations

This research, in conjunction with research at Georgia Tech (Aydemir 2000), found that tension field action shear capacity is fully applicable to hybrid girders. The AASHTO shear capacity equations are accurate for hybrid girders and that there is not a moment-shear interaction for any plate girder, whether homogeneous or hybrid. Allowing tension field action in hybrid plate girders and removing the moment-shear interaction for all plate girder designs would be a major advancement for steel bridge design.

References

AASHTO, (1998), *LRFD Bridge Design Specifications*, 2nd Edition, American Association of State Highway and Transportation Officials, Washington, D.C.

Aydemir, Murat, (2000), "Moment Shear Interaction in HPS Hybrid Plate Girders," Master's Thesis, Georgia Institute of Technology.

Barker, M.G., and Schrage, S.D., (2000), "High Performance Steel Bridge Design and Cost Comparison," Transportation Research Record No. 1740, Transportation Research Board, Washington, D.C., pp 33-39.

Barker, M.G., Hurst, A.M., and White, D.W., (2002), "Tension Field Action in Hybrid Steel Girders," AISC Engineering Journal, American Institute of Steel Construction, Vol. 39, No. 1, 1st Quarter, pp 52-62.

Barth, K.E., White, D.W. and Bobb, B. (2000), "Negative Bending Resistance of HPS 70W Girders," Journal of Constructional Steel Research, 53(1), pp. 1-31.

Basler, Konrad, (1961a), "Strength of Plate Girders in Shear," *ASCE J. Struct. Div.*, Vol. 87, No. ST7, pp. 151-180.

Basler, Konrad, (1961b), "Strength of Plate Girders Under Combined Bending and Shear," *ASCE J. Struct. Div.*, Vol. 87, No. ST7, pp. 181-197.

Davis, Benjamin, (2002), "Experimental Moment-Shear Interaction Testing of HPS Hybrid Girders," Master's Thesis, University of Missouri – Columbia.

Goessling, Victoria, (2002), "Investigation of TFA in the Shear Design of Hybrid Girders," Master's Thesis, University of Missouri – Columbia.

Hurst, Austin, (2000), "Tension Field Action in HPS Hybrid Plate Girders," Master's Thesis, University of Missouri – Columbia.

Rush, Courtney, (2001), "Experimental Tension Field Action Behavior in HPS Plate Girders," Master's Thesis, University of Missouri – Columbia.

Schreiner, John, (2001), "Experimental Testing of HPS Hybrid Plate Girders in Shear," Master's Thesis, University of Missouri – Columbia.

Zentz, Adam, (2002), "Experimental Moment-Shear Interaction and TFA Behavior in Hybrid Plate Girders," Master's Thesis, University of Missouri-Columbia.

Zentz, Adam, (2002), "Data Results of TFA Girder Tests," Results Volume, University of Missouri – Columbia.